NTNU
Norwegian University of
Science and Technology

Hydrodynamic effects relevant for free-falling lifeboats in wave conditions

Vegard Netland

Marine Technology
Submission date: June 2017
Supervisor: Marilena Greco, IMT
Co-supervisor: Andrea Califano, DNV-GL
Sebastien Fouques, SINTEF

Norwegian University of Science and Technology
Department of Marine Technology

MASTER THESIS IN MARINE TECHNOLOGY

Spring 2017

FOR

Vegard Netland

Hydrodynamic effects relevant for free-falling lifeboats in wave conditions

(Hydrodynamiske effekter relevant for fritt fall livbåter i bølgeforhold)

Free-fall lifeboats represent a good alternative to conventional, davit launched, lifeboats (lowered to sea by means of cables) because they require shorter time for launching and can have more momentum for escaping the host ship/platform. The different phases of their evolution have been investigated during the project thesis with focus on the water-entry and later stages. A simplified body geometry was modelled numerically and studied with a selected CFD commercial solver assuming calm-water conditions and incompressible air.

The project activity was carried out together with two other master students. The master thesis will be individually carried out, but with some shared investigations.

Objective

Present master thesis aims to continue the numerical investigations started during the project thesis focusing on the influence of incident waves on the lifeboat behaviour during water-entry and later stages.

The work should be carried out in steps as follows:

1. Summarize major findings/outcomes from the project thesis and investigate possible reasons for questions left open. The latter part will be carried out in collaboration with the other two students working on the same simplified lifeboat concept.
2. Complement the literature study of the project with state-of-the-art works on numerical/experimental/theoretical studies in waves relevant for the topic of interest.
3. Use the simplified lifeboat geometry studied during the project thesis and perform a systematic numerical study on the relevant parameters connected with initial conditions, assuming calm water and incompressible air, and using the CFD solver selected in the project work.
4. Using findings from the literature study performed in step 2, perform a numerical investigation on the influence of incident regular waves on the lifeboat behaviour using the CFD solver selected in the project work. Study the sensitivity of the results to the wave phase at the impact of the lifeboat with the water surface, for at least three wave headings and steepnesses.

The work may show to be more extensive than anticipated. Some topics may therefore be left out after discussion with the supervisor without any negative influence on the grading.

The candidate should in his report give a personal contribution to the solution of the problem formulated in this text. All assumptions and conclusions must be supported by mathematical models and/or references to physical effects in a logical manner.

The candidate should apply all available sources to find relevant literature and information on the actual problem.

The thesis should be organised in a rational manner to give a clear presentation of the work in terms of exposition of results, assessments, and conclusions. It is important that the text is well written and that tables and figures are used to support the verbal presentation. The thesis should be complete, but still as short as possible. In particular, the text should be brief and to the point, with a clear language. Telegraphic language should be avoided.

The thesis must contain the following elements: the text defining the scope (i.e. this text), preface (outlining project-work steps and acknowledgements), abstract (providing the summary), table of contents, main body of thesis, conclusions with recommendations for further work, list of symbols and acronyms, references and (optional) appendices. All figures, tables and equations shall be numerated.

The supervisor may require that the candidate, in an early stage of the work, present a written plan for the completion of the work. The plan should include budget for the use of computer and laboratory resources that will be charged to the department. Overruns shall be reported to the supervisor.

From the thesis it should be possible to identify the work carried out by the candidate and what has been found in the available literature. It is important to give references to the original source for theories and experimental results.

Supervisor : Marilena Greco

Co-supervisor : Andrea Califano

Co-supervisor : Sebastien Fouques

Submitted :15 January 2017

Deadline :11 June 2017

Abstract

A free- falling lifeboat is a last resort evacuation system, installed on many rigid and floating offshore structures. The diving process of a free-falling lifeboat is a complex matter, as the external forces varies through the process. The diving process is essentially divided into six different phases. These are the launching phase, free-falling phase, water entry phase, submerged phase, water exit phase and the sail away phase. The launching and free-falling phase determines the initial conditions at the point of impact, typically this will be impact velocity, water entry angle and angular rotations. As the body enters the water, it will be subjected to slamming forces. The pitch motion initially turns from clockwise to counter clockwise rotation, leading to larger slamming forces on the aft part. Eventually the aft part crosses the water surface and there will be an air cavity formation. The gravity will press the two newly formed free surfaces together and the unavoidable collapse leads to a large pressure on the body, in its direction of motion. This is due to the pressure from the water on the newly formed air bubble, entrapped on the very aft part. The body reaches its maximum submergence and then it starts the ascent phase, driven by the buoyancy. In the case of a positive surge motion and a counter clockwise rotation, the body will get this additional contribution in the ascent. The body eventually exits the water, where it gets a certain pop-up height, this height depends on the exit velocity and angle. As the body re-enters the water surface it can be subjected to a second slamming, and its magnitude is dependent on the pop-up height and the rotation after the water exit. It is favourable that the body sail as far as possible away from the evacuation scene. And this distance is dependent on the other phases.

A simplified free-falling lifeboat geometry were chosen for the simulations. The body is a semi-ellipsoid with length 10 m, and largest diameter 3 m. The simulations are run in the commercial software Star-CCM+. The simulations are computational expensive, and most of the simulations has been simulated on the high-performance computer, Vilje. A convergence check was preformed to investigate the quality of the solution and a suitable mesh size has been chosen with respect to satisfactory global behaviour and computational time.

A simulation has been preformed in calm water conditions. The result and behaviour of the body is reasonable compared to theory. The body is subjected to large deaccelerations and counter clockwise pitch accelerations in the water entry phase. The formation of an air cavity and its collapse is clearly

visual in VOF-scenes and as a large peak in the body-fixed acceleration plot. The body exits bow first, gets some air time, and is subjected to a small second slamming as it re-enters the water surface.

A parameter investigation has been preformed where the impact velocity, water entry angle and centre of gravity in z-direction has been changed with $\pm 5\ m/s$, $\pm 5°$ and $\pm 0.2\ m$, repectivly. The results showed that changing the velocity gave largest effect in the behaviour of the body, but the highest water entry angle gave the largest submergence which is an important parameter as it gives the highest hydrostatical pressure. Changing the centre of gravity showed to have relative small effects.

The lifeboat will most likely be used in a storm-conditions. Eighteen different cases has been simulated, with four different wave phases in three different headings. Three of these has been tested for two additional steepnesses. The waves are modelled as regular linear waves. The results shows that the behaviour of the body is greatly affected when waves are included in the simulation. The wave forces contribute in form of Froude-Krylov forces, diffraction forces and additional drag forces. Some of the largest accelerations in the water entry phase are found when the body dives in the wave phase where the fluid velocity is acting upwards. Large accelerations in the water entry phase are also observed when the fluid velocity is acting in the same global x- direction as the body. This creates a large counter clockwise pitch velocity which increases the slamming load on the aft part. The second slamming is dependent on the water exit, where the exit velocity, water exit angle, wave phase and heading are decisive.

The effect of decreasing the steepness was in general smaller accelerations in the water entry phase. The particle velocities are reduced as they are proportional to the wave amplitude. However, the second slamming is dependent on the water exit and the body rotation, and the CAR values shows that there can be large stresses on the passengers also in the case of small steepnesses.

Uncertainties connected with the simulations are the segregated flow and its weakness in term of predicting impulse forces like slamming, and how this manifests further in the solution. There has also been detected some unreal large velocities at the aft corner, leading to uncertainties on how these will affect the solution. Some errors in the interpolation between the cells in the overset mesh will be present as the overset mesh does not have a uniform cell size.

Sammendrag

En fritt-fallende livbåt er et siste utveis evakueringssystem, installert på mange faste og flytende offshore-strukturer. Stupeprosessen til en fritt-fallende livbåt er en kompleks sak, da de ytre kreftene varierer gjennom prosessen. Stupeprosessen er i hovedsak delt inn i seks forskjellige faser. Dette er slippfasen, fritt-fall fasen, vannsammenstøtfasen, neddykket fase, vannutgangsfase og seile fasen. Slipp- og fritt-fall-fasen bestemmer forholdene ved vannsammenstøtet, typisk vil dette være vannsammenstøthastighet, vanninngangsvinkel og vinkelrotasjoner. Når kroppen entrer vannet, blir den utsatt for slamming krefter, og stampebevegelsen svinger raskt fra retning med klokken til retning mot klokken, noe som fører til større slammingkrefter på akterdelen. Til slutt krysser akterdelen vannoverflaten, hvor en luftkavitet dannes. Tyngdekraften vil presse de to nyopprettede frie overflatene sammen, og det uunngåelige kollapset fører til en stor kraft på kroppen, i bevegelsesretningen livbåten. Dette skyldes trykket fra vannet på luftboblen som er fanget langs hekken. Kroppen når sin maksimale neddykket posisjon, og så starter oppstigningsfasen, drevet av oppdriftskreftene. Livbåten vil få et ekstra bidrag i stigningsfasen ved tilfeller av jagebevegelse kombinert med stamping mot klokken. Kroppen forlater til slutt vannet, der den får en viss pop-opp høyde, denne er avhengig av utgangshastigheten og utgangsvinkelen. Etter hvert som livbåten re-entrer vannoverflaten, kan den bli utsatt for en andregangsslamming. Dens størrelse er avhengig av pop-up-høyden og rotasjonen etter vannutgangen. Det er gunstig at kroppen seiler så langt som mulig bort fra evakueringsscenen. Og denne avstanden vil være avhengig av de andre fasene.

En forenklet fritt-fallende livbåtgeometri ble valgt for simuleringene. Kroppen er en halv ellipsoid med lengde 10 m og største diameter 3 m. Simuleringene kjøres i den kommersielle programvaren Star-CCM+. Simuleringene er beregningstunge, og de fleste simulasjonene er simulert på den høytytende datamaskinen, Vilje. En konvergenskontroll ble forhåndsformet for å undersøke løsningens kvalitet og en passende mesh-størrelse er valgt med hensyn til tilfredsstillende global oppførsel og beregningstid.

En simulering har blitt utført i stille vann. Resultatene og oppførselen til kroppen er rimelig i forhold til teorien. Kroppen er utsatt for store retardasjoner og negative stampeakselerasjoner i vanninngangsfasen, og dannelsen av en luftkavitet og dens kollaps er tydelig visuelle i VOF-scener og som en stor akselerasjonstopp. Livbåten går ut av vannet med baugen først, får en viss svevetid, og blir utsatt for en liten andregansslamming når den re-entrer vannoverflaten.

En parameterundersøkelse er utført der inngangshastigheten, inngangssvinkelen og tyngdepunktet i z-retning er endret med henholdsvis ± 5 m / s, ± 5 ° og ± 0,2 m. Resultatene viste at endring av hastigheten gav størst effekt i livbåtens oppførsel, men den høyeste vanninngangsvinkelen gav den største neddykkingen som er en viktig parameter, da den gir det høyeste hydrostatiske trykket. Endring av tyngdepunktet viste relativ liten effekt.

Livbåten vil mest sannsynlig bli brukt i stormforhold. Atten forskjellige tilfeller har blitt simulert, med fire forskjellige bølgefaser i tre forskjellige bølgeretninger. Tre av disse har blitt testet for to ytterligere steilheter. Bølgene er modellert som regulære lineære bølger. Resultatene viser at livbåtens oppførsel blir sterkt påvirket når bølger er inkludert. Bølgekrefter bidrar i form av Froude-Krylov-krefter, diffraksjonskrefter og ekstra drag-krefter. Noen av de største akselerasjonene i vannsammenstøtfasen finner man når livbåten stuper i bølgefaser hvor fluidhastigheten virker oppover. Store akselerasjoner i vanninngangsfasen blir også observert når fluidhastigheten virker i samme globale retning som kroppen. Dette skaper en stor stampefart mot klokken, som vil øke slammingkraften på akterdelen. Andregangs slamming er avhengig av vannutgangshastigheten, vannutgangsvinkelen, bølgefasen og bølgeretning.

Effekten av å redusere steilheten var generelt sett mindre akselerasjoner i vannsammenstøtfasen. Partikkelhastighetene reduseres ettersom de er proporsjonale med bølgeamplituden. Andregangs-slamming er imidlertid avhengig av vannutgangen og kroppsrotasjonen, og CAR-verdiene (Combined Acceleration Ratio) viser at det kan være store belastninger på passasjerene, også ved små steilheter.

De største usikkerhetene i simuleringene er knyttet til den segregerte strømmingsløseren og dens svakhet i form av å forutsi impulskrefter som slamming, og hvordan dette gir videre utslag i løsningen. Det har også blitt oppdaget noen urealistiske store hastigheter på akterdelen ved hjørnene rett etter starten på neddykkingsfasen, og det knyttes usikkerhet i forhold til hvilken effekt disse vil ha videre i løsningen.

Preface

This thesis is written to fulfil the degree Master of Science, at the Norwegian University of science and Technology. It consists of a study of free-falling lifeboats, and their behaviour in wave conditions.

One parts of this thesis is written with fellow co-students Simen Groth and Andreas Svendsen, and the other part that includes waves, is an individual part. We wrote the specialisation project "Hydrodynamical effects off free falling lifeboats, a preliminary study" together in the fall 2016. None of us had any experience with CFD-analysis before the fall of 2016, and simulations of a free-falling lifeboat was challenging. There was a steep learning curve, and some crucial mistakes were made. One part of the objective of the master thesis is therefore to re-do the specialization project, which results in a common part from section "Introduction to free-falling lifeboats, phases and physics" to the "Parameter investigation" section. This is of agreement with our main supervisor, Professor Marilena Greco.

The topic has been challenging and educational with a steep learning curve.

I will like to thank my main supervisor, Professor Marilena Greco for helpful discussion and tips. Also for providing us with relevant theory and speeding up the process at all stages. She has also provided us with two co-supervisors.

I would like to thank our two co-supervisors Andrea Califano and Seabstien Fouques for helpful discussions and tips regarding the CFD analysis in Star CCM+ and theory regarding the subject.

I would like to thank Simen Groth and Andreas Svendsen for the collaboration on the common part, and also for helpful discussion and tips on the individual part.

Trondheim, June 11, 2017

Vegard Netland

Contents

List of figures

List of tables

Nomenclature

β	Dead rise angle
Γ	Diffusion vector
γ	Surface tension
$\gamma(2)$	Forcing coefficient
δ'_{ij}	Kronecker delta
η	Surface elevation
$\ddot{\eta}_i\ , i = 1, \dots ,6$	Body fixed acceleration in the different DOF's
θ_0	Static contact angle
κ	Von Karman's constant
λ	Wave length
η_b	Water spray point
μ	Dynamic viscosity
μ_τ	Frictional velocity
ν	Kinematic viscosity
ρ	Fluid density
ρ_s	Solid density
τ_W	Shear stress
ϕ	Velocity potential
$\phi(2)$	Transport of a scalar property
$\phi(3)$	Current solution to the transport equation
ϕ^*	Value of the forces solution
ω	Wave frequency
Ω	Submergence
$\boldsymbol{a}$	Surface vector
a	Wave amplitude
a_x	Acceleration in x-direction
a_y	Acceleration in y-direction
a_z	Acceleration in z-direction
c	Wetted length

d	Water depth
f	Frequency
$f(2)$	Roughness form function
f_1	Wave damping constant
f_2	Wave damping constant
f_i	Body force
f_{strech}	Stretch factor
g	Gravitational acceleration constant
h	Wave height
h_p	Pop-up height
k	Wave vector
n_d	Damping exponent
p	Pressure
q_ϕ	Source term
t	Time
t_0	Air cavity formation starting time
u	Horizonal velocity in x-axis
u^+	Non-dimensional velocity
v	Horizontal velocity in y-axis
$v_{x'}$	Velocity in the body-fixed x-direction
w	Vertical velocity in z-axis
x_{min}	Minimum cell size
x_{ed}	Wave damping end point
x_{sd}	Wave damping start point
z_0	Creation position of air cavity
z_{0r}	Roughness length
z_b	Vertical position of the bow
$\boldsymbol{A}$	Surface area of control volume
A_{33}	Added mass in heave
Bo	Bond number
C_a	Capillary number

C_D	Drag coefficient
D	Diameter
F_3	Force in heave
F_D	Drag force
Fr	Froude number
H	Total cavity closure height
H_c	Cavity closure height
$H(f)$	Frequency domain transfer function
I_q	Integrated quantity
L	Length
R	Radius
Re	Reynolds number
S_ϕ	Source term
S_z^d	Residence term
T	Wave period
T_c	Air cavity closure time
U	Velocity
U_w	Wind velocity
U_0	Velocity
V	Velocity
V	Control volume
We	Webber number
X_h	Prism layer height
Y^+	Non-dimensional wall distance
∇	Nabla operator

$2D$	Two-dimensional
$3D$	Three-dimensional
CAR	Combined acceleration ratio
CFD	Compactional fluid dynamics

CFL	Courant Friedrichs Lewy
COG	Centre of gravity
DOF	Degree of freedom
OA	Order of accuracy
$RANS$	Reynolds-Averaged Navier-Stokes
VCG	Vertical position of centre of gravity
VOF	Volume of fluid

1 Introduction

A free- falling lifeboat is a last resort evacuation system, installed on many rigid and floating offshore structures. The body is often mounted on a skid on the mother vessel, which it will slide down from after the release. After leaving the skid it will be free- falling for a while, before it enters the water. Eventually the body gets fully submerged for a period, before it exits through the water surface. Then it should be able to sail as far as possible away from the evacuation scene.

This is the essence of free-falling lifeboat diving. There are numerous physical parameters influencing this complex problem. The hull geometry, material properties, mass distribution, fluid properties, impact parameters and weather conditions are some of the parameters that should be included to get a realistic solution of the problem.

The different phases come with different external loadings. The launching from the skid is dependent on the motion of the of the mother vessel, the free-falling phase is dependent on weather conditions, such as the magnitude of the wind and its direction. Waves are affecting the initial conditions in the water entry phase, as well as all the later phases. Current can also effect the behaviour of the body. This makes the topic highly complex.

CFD analysis will be performed by using Star CCM+. A simplified lifeboat geometry is applied, and its behaviour will be investigated in calm sea and in wave conditions.

2 Introduction to free-falling lifeboat phases and physics

In the case of free-falling lifeboat diving, the process is divided into different phases. The body operates in different fluids, enters the water in high velocity, gets fully submerged, ascents to the surface and should then it be able to operate as a sailing vessel. This complex matter is thus divided into launching phase, free-falling phase, water entry phase, submerged phase, water exit phase and the sail away phase.

The theory in the submerged phase, water exit phase and partly the water entry phase, will be based on studies of water entering and exiting projectiles, combined with theory from previous papers regarding free-falling lifeboats.

2.1 Launching phase

The lifeboat will normally rest at a skid mounted on the mother vessel. Several releasing mechanisms for launching are available, most common are the releasing hook. The lifeboat is released from the hook by a manually driven hydraulic pump that is possible to operate from the inside. After releasing, the lifeboat slides along the skid driven by the gravitational and frictional forces. As the boat passes the end of the skid, an increasingly part of the lifeboat will be free falling, while the behind part will have contact with the end of the skid. This will lead to a rotation which depend on the position of the skid in the global coordinate system.

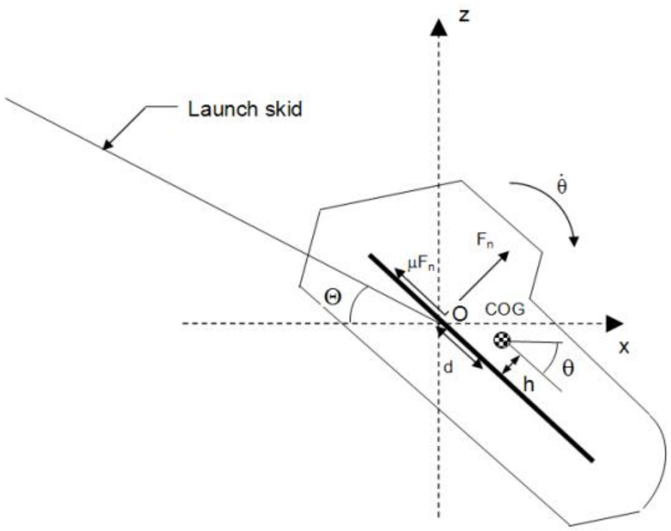

Figure 2.1: Shows the lifeboat on a launch skid, as the center of gravity passes the end of the launch skid.

Assuming a global coordinate system shown in Figure 2.1 where z represents the vertical axis, and x and y the two normal horizontal axes. The gravitational force will act downwards in z-direction. Ideally the skid plane lies in the x-z plane, the lifeboat will then move straight forward down the skid, without any translation in the y- direction. Then if the centre of gravity of the lifeboat lies along the y-axis, there will only be rotation about one axis, the y-axis. This rotation is pitch.

Since the lifeboat is used in emergency cases, the operational conditions will likely be harsh, and an ideal launch situation will be unlikely. When the skid plane moves out of the x-z plane, the skid plane will be skewed seen in the y-z plane. The gravity force pulls on the centre of gravity, leading to rotation in roll and yaw as well as pitch. The skid plane can also be tilted forward and backwards as a consequence of rotational motion of the mother vessel parallel to the x-axis of the skid plane. The result of this can respectively be an increase and decrease in the initial free-falling velocity. The rotation is dependent on the velocity at the end of the skid. If the lifeboat slides slowly over the skid end, the gravity has a large amount of time to pull down the part that has passed the skid end, causing a large rotation. In the case of high sliding velocity, the rotation will be small.

The launching plane is dependent on the motion of the mother vessel, hence the initial conditions in the launching phase is crucial for the further phases.

2.2 Free-falling phase

The free-falling phase starts when the lifeboat no longer has contact with the skid, that is when the normal reaction force from the skid is zero, $F_n = 0$, seen in Figure 2.1. The free-falling phase is affected by the rotation (angular velocity), initial velocity out from the skid, skid plane angle (launching angle), air resistance and wind loads. The free-falling time is dependent on the diving height, that is the freeboard position of launching.

Figure 2.2: Shows a free-falling lifeboat in the free-falling phase. This is a Norsafe AS production, one of the leading lifeboat producers. (Consultance, 2017)

In wave conditions where the launching point on the vessel has a relatively steady global position, the diving height will depend on the phase of the impact wave. It will increase if the lifeboat is launched such that it enters in a through and decrease when entering at a crest. Longer free-falling time leads to a larger effect of the air resistance, wind loads and larger impact velocities. However, the wind loads are not constant trough the free-falling distance. The wind velocity profile is dependent on the atmospheric stability conditions. It is also dependent on the hour of the day and changes between day and night, dawn and dusk. An example of a wind velocity profile from DNV for stable (low temperature lapse rate), neutral (medium temperature lapse rate) and unstable (high temperature lapse rate) atmospheric conditions are shown in Figure 2.3. (DNV-GL, 2010) It should be noted that most lifeboats are installed between 10-30 meter above sea level, hence, the difference regarding the wind velocity for the presented atmospheric condition is small.

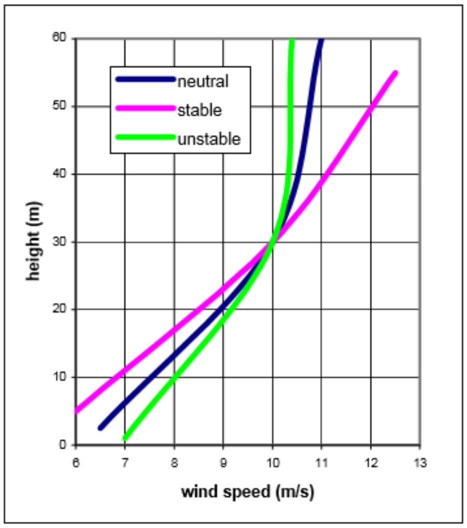

Figure 2.3: Wind conditions (DNV-GL, 2010)

A logarithmic wind velocity profile for neutral atmospheric conditions from DNV-GL is expressed as

$$U_w(z) = U_w(H_w)\left(1 + \frac{ln\left(\frac{z}{H_w}\right)}{ln\left(\frac{H_w}{z_0}\right)}\right) \qquad [1]$$

Where H_w is the height of the mean wind velocity measuring, z is the height at any given point and z_0 is the terrain roughness parameter also known as the roughness length. In open sea with waves, this value is in the range of 0,0001 – 0,01 m.

The effect of the rotation, air resistance and the wind loads are dependent on the diving time. Rotation is measured in rotation angle over time, hence the water entry angle is dependent on launching angle and the rotation given at the end of the skid and free-falling time.

2.3 Water entry phase

The water entry phase starts from initial impact between body and the free surface, and ends when the aft part of the body is below the undisturbed free surface. The launching and free-falling phases sets the initial parameters for the water entry. These parameters are the velocity, water entry angle and angular velocity in roll pitch and yaw. The typical diving height for a free-falling lifeboat launched at a skid, is between 20 m and 30 m. This will provide an impact velocity of approximately 20 m/s. The skid usually has a value of 35°, and a desirable water entry angle has a value of 50°-60°, hence the angular velocity is providing the water entry angle. As the body enters the water it is subjected to resistance forces in terms of drag, viscosity effects and slamming. The influence of slamming forces is most critical for the water entry phase, due to the transfer of momentum from the lifeboat to the impact fluid.

2.3.1 Slamming

In the water entry phase, the free-falling lifeboat will experience impulse loads with high pressure peaks, propagating from the bow to the stern. This phenomenon is known as slamming. It is a strongly non-linear problem. It is very sensitive of the relative impact velocity, that is the liquid-body velocity, and the dead rise angle, β, which is the angle between the water and the body. The sudden transition from air to water leads to large forces on the body, and can lead to global elastic transient resonance oscillation. The slamming load are the most critical load in the matter of free-falling lifeboats, and govern the design of the local hull structure. In this phase, the pitch rotation will reverse from the free-falling rotation. The rotation is now counter clockwise, when using Figure 2.4 as reference, and causes increased slamming pressure on the aft part of the hull. For oval geometry cases, such as the lifeboat form, it is important that the water entry angle does not become too low. If it does, the slamming forces will increase rapidly due to the large change in added mass.

Some of the physical phenomena connected with slamming is compressibility of water, air cushions/bubbles (for small angle between the body and the water), hydroelasticity, cavitation and ventilation.

2.3.1.1 Simplified calculation approach

There has been performed extensive researching on the field of slamming. Von Karman (1929) and Wagner (1932) had a large impact on the field.

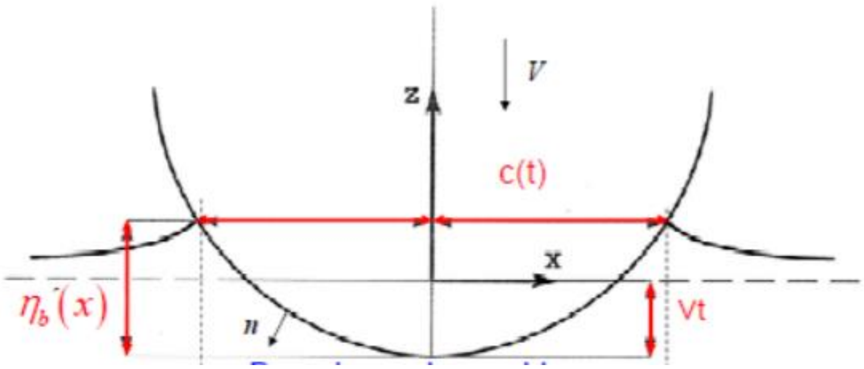

Figure 2.4: Shows how the different parameters are defined in the analysis of impact forces and pressure on a body.

The wetted area is taken to be between $-c(t) \leq x \leq c(t)$, shown in Figure 2.4. Von Karman (1929) developed a method with a simplified approach. The wetted length is taken at the free surface, excluding the up-rise water effect. Wagner (1932) includes this effect and the wetted area is taken at a height $\eta_b(x)$ which is defined as the distance from where the body has its maximum submerged point up to the point of water spray.

The density of water is almost independent of the temperature and pressure (Engineering ToolBox, u.d.), which make the incompressible assumption appropriate. For a frictionless fluid, there will be no shear forces and torque. A frictionless flow without initial fluid rotation, will never start to rotate, and the velocity can be derived by the velocity potential spatial derivatives. Equation [3] - [8], shown below, are only valid for frictionless, stationary and incompressible fluid, meaning that potential theory is applicable.

$$U = \nabla\phi \qquad [2]$$

Then for a simple two-dimensional projectile penetrating the free surface, the force in heave can be written as

$$F_3 = \frac{d}{dt}(VA_{33}) + \rho g \Omega(t) \qquad [3]$$

F_3 is the force in heave, A_{33} is the added mass in heave. The term $\rho g \Omega(t)$ is the time dependent buoyancy force, and is initially zero. The velocity and added mass in heave are time dependent variables, hence equation [3], by utilizing the product rule, can be written as

$$F_3 = A_{33}\frac{dV}{dt} + V\frac{dA_{33}}{dt} + \rho g \Omega(t) \qquad [4]$$

In this case, the pressure can be defined from the Bernoulli equation

$$p = -\rho g z - \rho\frac{\partial\phi(x,z)}{\partial t} - \frac{1}{2}\rho(\nabla\phi)^2 \qquad [5]$$

For the slamming case, by assuming that $z = 0$ at the mean water surface, and neglecting the spatial derivatives of the velocity potential, as they are much smaller than the time derivatives of the velocities potential, equation [5] can be simplified to

$$p = \rho\frac{\partial\phi(x,z)}{\partial t} \qquad [6]$$

The velocity potential on the body can be written as

$$\phi = -V\sqrt{c^2 - x^2}\,, \quad |x| < c(t) \qquad [7]$$

Then by time differentiate the velocity potential, the pressure becomes

$$p = \rho\frac{dV}{dt}\sqrt{c^2 - x^2} + \rho V\frac{c}{\sqrt{c^2 - x^2}}\frac{dc}{dt} \qquad [8]$$

The first term from equation [8], $\rho\frac{dV}{dt}\sqrt{c^2 - x^2}$, represents the added mass pressure and the second term, $\rho V\frac{c}{\sqrt{c^2-x^2}}\frac{dc}{dt}$, represents the slamming pressure. (Faltinsen, 1990)

For a “real flow”, viscous forces will always be present, resulting in shear stresses and boundary layers, but for large $Re = \frac{uL}{\nu}$, irrotational fluid flow outside the boundary layer is a valid assumption. For the slamming case, it is assumed that the spatial derivatives are negligible compared to the time derivatives. Since the viscous term is multiplied with the spatial derivatives in the Navier–Stokes equation, the inviscid fluid assumption is reasonable for the case of slamming.

2.3.1.2 Slamming calculations for free-falling lifeboats

Calculation of the slamming pressure for free-falling lifeboats is a complex matter. There will be an oblique impact, the body is three-dimensional and waves should be considered. Sauder proposed a method for calculating the slamming phenomena for free-falling lifeboats. The method is developed to predict the trajectory in the six degrees of freedom in waves. In able to do so, three dextral orthogonal coordinate systems are used, and some approximation and assumptions had to be set.

Approximations:

- Three-dimensional formulation of fluid momentum conservation
- Long wave
- A boundary element method for evaluating the added mass matrix

Assumptions:

- The viscosity and the compressibility of the water are neglected
- Potential theory is applied
- The fluid acceleration is assumed to be much larger than the gravity acceleration, hence the high-frequency free surface boundary condition $\phi = 0$ can be used.
- Von Karman approach, local water up-rise is neglected. The pressure in the spray area will be very close to atmospheric pressure. It is the hydrodynamic pressure and forces that are of interest.
- Ventilation, cavitation and hydroelasticity are neglected

(Sauder & Fouques, 2009)

2.3.1.3 Hydroelasticity

In slamming hydroelasticity is relevant for dead rise angles $\beta < 5^\circ$ and when the loading time associated with water entry is small or comparable to the natural wet period of the structure. Hydroelasticity means that the hydrodynamic loads affect the structural elastic vibrations and in return the elastic vibrations affect the fluid flow and related pressure field. When hydroelasticity matters in the slamming problem, the hydrodynamic and structural problems must be solved simultaneously. In extreme cases of flat impacts with hydroelasticity the maximum pressures cannot be used to estimate the structural response. Hydroelasticity is a phenomenon connected with slamming where the dead rise angle $\beta < 5^\circ$. (Greco, 2012)

2.3.2 Parameters defining the water entry

There are several parameters which influence the physics during a water entry problem, resulting in air entraining, super cavitation or maybe no cavity formation at all. Water entry with air cavity formation and air entraining are emphasis on in this thesis.

Air cavity is a result of viscous forces outweighing the surface tension, and the contact line is then pinned to the body surface at the air-water project line. This resulting in air to be entrained behind the body as the air cavity develops. For water impacts, where the fluid velocity is high, a small horizontal jet gets ejected at great radial velocity outwards from the intersection point. For Spheres, Thorodsen et. al (2004) found that this was the case for Re > 9000. (Truscott, et al., 2013)

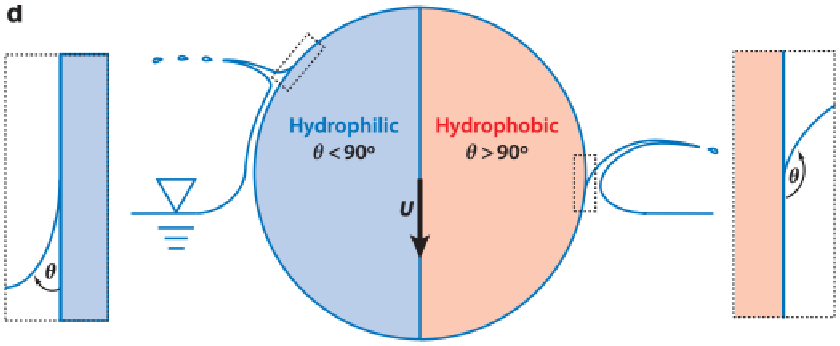

Figure 2.5: Shows the difference in splash crown formation for a hydrophilic and a hydrophobic case (Truscott, et al., 2013)

Important parameters for the entering body are geometry, wettability, density and location of center of mass, and due to variation in geometry, impact conditions and material properties, the water entry phenomenon is very complex and difficult to predict. Wettability is defined with the static contact angle θ_0 shown in Figure 2.5. If this contact angle, θ_0, is below 90 degrees, the water entry is called hydrophilic, while a θ_0 > 90 is called hydrophobic. For an interaction between a body and a given fluid with constant surface tension, less impact velocity is needed for the body at a higher θ_0 to ensure cavity creation.

Impact parameters influencing cavity creation are the impact angle, impact velocity, transverse and longitudinal spin. Truscott, et al. (2013) did experience with billiards ball, where the contact angle varies from one side to another, due to an initial spin counter clockwise. The left-hand side of the sphere experienced a larger dynamic wetting angle, due to an advancing contact angle resulting in a larger outward splash. For the right-hand side, the spin resulted in positive vertical velocity, contributing to a wedge of fluid is drawn across the cavity and inhibits splash growth. (Truscott, et al., 2013)

Important parameters for the opposite fluid is viscosity, density and surface tension. Surface tension is due to the cohesive force between the liquid molecules, with dimension force per unit length. For sea water it has a natural value of $72.8 * 10^{-3}\ N/m$. Truscott did experiments with spheres, only changing the body density ρ_S, showing the dependency of density relation, $\frac{\rho_S}{\rho}$, and cavity closure height divided on total cavity height, $\frac{H_c}{H}$. The experiment showed that $\frac{H_c}{H}$ increased with increasing $\frac{\rho_s}{\rho}$. More about cavity shapes and creation will be included in the submerged phase, section 2.4.

The value of the surface tension may be of importance for how the air cavity forms. Further influencing all the aspects of the behavior of a body, such as acceleration, velocity and trajectory when the body moves from the water entry phase to the submerged phase. For relatively large bodies and velocities, surface tension can be neglected, though it might be of importance near cavity closure. The formation of an air cavity can be predicted by non-dimensional numbers. They are all inverse proportional with the surface tension force γ. A high Capillary number may indicate that an air cavity will form, defined as

$$C_a = \frac{\mu U_0}{\gamma} \qquad [9]$$

Where μU_0 is the viscous force. The Bond number is the ratio between gravitational forces, $\rho g D^2$, and surface tension forces. The air cavity shape is dependent on the ratio between surface tension and inertia forces for a low Bond number, defined as

$$Bo = \frac{\rho g D^2}{\gamma} \tag{10}$$

For low Bond numbers the cavity shape will be dependent on the ratio between inertia forces and surface tension, this is known as the Webber number. The cavity breakup and characterization of the splash crown stability can be predicted by this number, given as

$$We = \frac{\rho U_0^2 D}{\gamma} \tag{11}$$

Where $\rho U_0^2 D$ represents the inertia force. The Froude number characterizes the macroscopic behaviour of the air cavity

$$Fr = \frac{U_0}{\sqrt{gD}} \tag{12}$$

The lifeboat structure is relative large and the water entry velocity is relative high. Additionally, a low surface tension for water, results in very high non-dimensional numbers. Therefore, the surface tension will have little influence in the submerged phase.

2.4 Submerged phase

The submerged phase starts when the aft part passes the free surface, and for this phase, the focus will mainly target the understanding of the cavity evolution of the air cavity behind the free-falling body. The body will experience large hydrostatical pressure on the hull as well as hydrodynamic forces. The translational and rotational velocity and the water entry angle at initial water entry, affects the trajectory through the water. As mentioned earlier in the water entry phase, there are several parameters influencing the water entry, increasing the complexity of the submerged phase. External forces will also have great effect on the trajectory. These external forces are primarily waves, but also strong current can have an effect. The waves have local phase dependent fluid particle velocity and acceleration properties, as well as wave surface elevation and slope.

2.4.1 Air cavity formation

As the very aft passes the free surface, the corner at the newly created free surface has an initially infinite curvature. The gravitational force tries to flatten out this new surface, dragging the two corners diagonally inwards towards the body-center. The contact point of where the two surfaces collapses will be the point of air cavity closure. At this point a singularity will emerge. This results in a formation of water jets. The water jets move in oppositely directions from the collapse location, one towards the body inside the entrapped air bubble, and the other in the reversed water entry direction. As the two water surfaces collapses, the body will experience an abrupt change in acceleration. The reason for this is that the newly entrapped bubble behind the lifeboat is compressed by the water surrounding it, resulting in that the body will get a positive acceleration contribution in the direction of motion. After the first compression, the entrapped bubble will oscillate due the difference in pressure inside the bubble and the surroundings, while it decreases in size until it gets dissolved.

The formation of an air cavity behind the lifeboat contributes to a stronger retardation. Hence when designing a lifeboat hull, there will be a high focus on minimizing the air cavity by mainly altering the lifeboat-stern geometry. The formation of the air cavity is most pronounced at the aft part of the body. However, there will be appendages and a wheelhouse on a lifeboat, where air cavity also will be present, but in a smaller scale. (DNV-GL, 2016)

2.4.2 Cavity classifications

The creation of air cavity begins in the first few moments after impact, as the fluid is displaced downward and upward, forming a splash curtain.

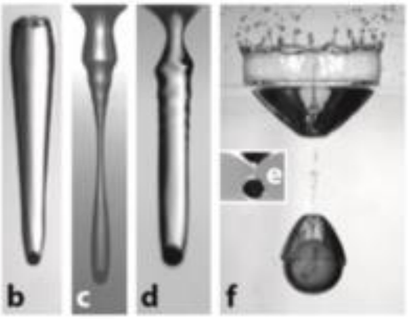

Figure 2.6: Visualization of different water entry events (Truscott, et al., 2013)

Air cavity can be divided into four types of cavity formations after water impact. Surface seal, deep seal, shallow seal and quasi-static seal, Figure 2.6 b, c, d and f, respectively. Surface seal is defined when cavity closure occurs at the free surface, with a long cavity attached beyond the body. Surface seal is often more relevant for higher Froude's Number, while a deep seal, where the pinch off occur closer to the body often is connected with relatively low Froude Number. For shallow seal, the pinch of occurs just below the water surface, like a deep seal, but with a shape more like a surface seal.

The main difference between a shallow and a deep seal is that the pinch of close to the surface in a shallow seal is due to capillary instabilities rather than hydrostatic pressure. The opposite is the case for a deep seal. Quasi-static seal is often in connection with pinch of at the body or close to it. This is common for cases where the body is almost restrained to enter the water due to the large surface tension. Aristoff and Bush (2009) presented low Bond number cases where $10^{-2} < \mathrm{Bo} < 10^{3}$ versus Froude numbers of $\sqrt{10^{-0,5}} > Fr < \sqrt{10^{2,5}}$ and stated that only surface and deep seal occurs for Bo > 10^{3}. Lee et al. (1997) suggest that deep seal occurs roughly halfway between the surface and a projectile for $\sqrt{20} < Fr < \sqrt{70}$, where transition to surface seal occurred for $Fr > \sqrt{150}$.

In the case of free-falling lifeboats, the surface tension is considerably low. This leads to high Capillary, Bond and Webber number (Equations [9] - [11]), which predicts air cavity formation in form of deep seal corresponding with Froude number range for lifeboats.

2.4.3 Physical insight

The study regarding the dynamics of water impact and air cavities was intensified during the world war because of the needed design of military projectile entering water in high speed. Therefore, most of these early experiments were conducted with a high Froude Number, resulting in relative unimportant gravity effects. In recent years, scientific interest and practical importance have led to an increase of studies with relatively low Froude number, where gravity effects are comparable to inertia forces.

To better understand the physics in the submerged phase, it is important with a basic knowledge of the cavity development and evolution, regarding both assumptions and simplifications made for the varies derivations. Experiments is often conducted with high Reynolds number to ensure more accurate cavity parameter calculations when potential theory is applied. This is due to the small influence of the viscous forces. Not only experiments have been conducted regarding water entry dynamics, but also theoretical and numerical studies have been performed.

Birkhoff and Zaranthello (1957) and Lee, Longoria and Wilson (1997) used a two-dimensional analytic model to study the air cavity dynamics. In a two-dimensional potential flow, air cavity cannot be created, and to account for the three-dimensional flow effects, they had to introduce an arbitrary constant to make the kinetic energy finite. This arbitrary constant was further determined by fitting the theoretical prediction with experimental data and/or nonlinear numerical simulations. A thorough explanation of a specific derivation regarding the air cavity dynamics will be included in the compressible part for this thesis. (Yan, et al., 2009)

A simple derivation of how the cavity closure is dependent of the Froude number, can be obtained by dividing the water entry of a body and the following air cavity into two main phases. Assuming a relative low Fr>10 and a constant vertical velocity, the vertical position of the bow, z_b, after impact can be defined as $z_b = \mathrm{Vt}$, if $t = 0$ at initial impact. At some height, z_0, the creation of the cavity begins, with an initial radius $r(z_0, t_0) \approx R$, where R is the body radius assuming an axisymmetric body. As the body continuous to descend below z_0 ($t > t_0(z_0)$), the cavity expands, $\frac{\partial \mathrm{r}}{\partial \mathrm{t}} > 0$, for some time. When the cavity has reached the maximum radius, the expansion time $\delta t_1(z_0)$ is over, and the radius will decrease, eventually resulting in collapsing of the air cavity. Generally speaking, there is a height H_c, where the cavity first closes at $t = T$, and $r(H_c, T) = 0$. Initial air cavity closure can occur above the free surface, referred to as surface closure, or below the free surface, often referred to as deep closure or pinch of. Cavity closure is dependent on Froude number, where deep closure usually occurs for relatively low Froude numbers, while surface closure is more common for larger Froude numbers, discussed in section 0. Regarding the contraction phase, a basic estimate of closure time at any height z_o can be obtained by assuming steady state, with a constant radial velocity derived from Bernoulli equation,

$$-\frac{\partial r}{\partial t} = u(z_o) = (2gz_0)\text{^}0{,}5 \text{ for } t > t_o + \delta t_1 \qquad [\,13\,]$$

The time of collapse is $t_c(z_0) = t_0 + \delta t_1 + \delta t_2$, where δt_2 is equal to the collapsing phase time, and can be estimated as $\delta t_2(z_o) \cong R/u(z_o)$, by assuming that the maximum cavity radius is equal to the body radius. For many body shapes, like long vertical cylinders, the expansion phase is short compared to the collapsing phase, and can be neglected. Resulting in closure time defined as: $T = min_{z0}\,[t_0(z_0) + \delta t_2(z_0)]$ and substituting δt_2 in terms of z_o, a relation between Froude number and closure time can be found

$$\frac{TV}{D} \approx \left(\frac{3}{2^{5/3}}\right) Fr^{2/3} \qquad [\,14\,]$$

At pinch of position $z = H_c$, assuming that the total cavity height $H = TV$ at pinch of, is equal to $3H_c$. According to Duclas, et al. (2007), this relation, even though with many simplifications, will show good agreement with reality in the case of relatively long vertical cylinders. More detailed derivation of the equation above can be found in Mann (2005) and Mann, et al. (2007). (Yan, et al., 2009)

2.4.4 Capillary waves evolution in the air cavity water surface

As the two surfaces collapses together at the air cavity closure, it will result in a shock, leading to air, water jet and capillary waves moving towards the body along the free surface of the air cavity. The shock creates a wave packet containing wave of different frequencies, the waves spread with the velocity $c = \omega/k$, given by the dispersion relation $\omega^2 = \left(\frac{\gamma}{\rho}\right) k^3$, where plane capillary waves are assumed. γ is the surface tension and k is the wave vector. (Gekle, et al., 2008)

2.5 Water exit phase

An important parameter for the water exit for a body breaching the water surface, is the pop up height, h_p. It is defined as the height from the body center, to the undisturbed free surface. Pop-up height is of interest for all applications where objects breach the surface. For example, an emperor penguin breaches the surface to escape from predators. They release bubbles from their feather during ascent to reduce drag forces, resulting in an increased water exit velocity. In the case of a free-falling lifeboat, water exit speed is beneficial for a longer sail away distance.

The pop-up height depends on the free surface exit speed, which is dependent on the under-water trajectory and dynamics during surface breach. Vortex shedding is dependent on the release depth, and will in addition influence the trajectory and speed of the body. During ascent, vortices will shed differently, depending on the Reynolds number. This leads to three underwater trajectory regimes, often referred to as vertical, oblique, and oscillatory. This is demonstrated in Figure 2.7.

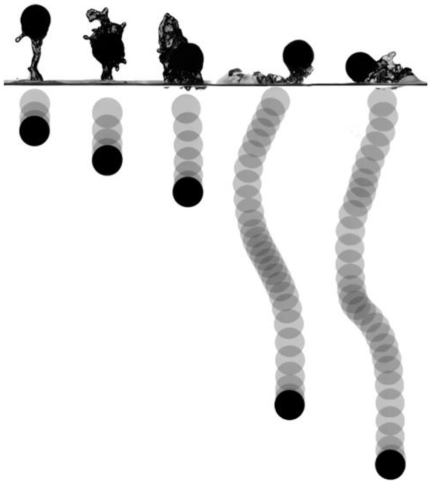

Figure 2.7: Trajectory dependent on released depth for ping-pong balls (Truscott, et al., 2016)

Depending on the Webber number (equation [11]) and the Froude number (equation [12]), during water exit in addition to the structure of the vortex shed near the water surface, the resulting splash plume and cavity will take on various forms. This indicates varying amounts of energy transferred to the fluid during water exit. A rough estimate of h_p can be derived from the mechanical energy considering the body at breach, assuming constant mass. The added mass will actually vary as the body breaches the surface, making the problem more complex

$$\frac{V_1^2}{2} + gh_1 = \frac{V_2^2}{2} + gh_2 \qquad [\ 15\ ]$$

Where $h_1 = h_p$, V_1 is the vertical velocity equal to zero at maximum h_p. V_2 is the vertical velocity at surface breach and h_2 is the height of the body center at water surface, equal to zero. When assuming zero net hydrodynamic forces acting on the body during breach, neglecting the work done by buoyancy and dynamic pressure forces and ignoring the energy lost when the body breaches the surface, resulting in splash and wave production, equation [15] can be simplified to

$$gh_p = \frac{V_2^2}{2} \qquad [\ 16\ ]$$

this yields

$$\frac{h_p}{D} = \frac{V_2^2}{2Dg} = \frac{1}{2} * Fn_b^2 \qquad [\ 17\ ]$$

Seen from formula [17], the pop-up height depends on the vertical free surface exit speed as mentioned above. An increased depth of release does not have to result in higher pop-up due to the fact that the water exit velocity do not correlate with an increasing function of the release depth. For a more reliable derivation of the exit speed, where the force balance is modeled for a sphere by setting the net vertical acceleration equal to zero, see Truscott, et.al. (2016), equation 4.

Depending on the pop-up height, slamming can also occur after the water exit phase, referred to as second slamming. In the cases of second slamming, the lifeboat can have a water entry angle close to zero degrees. This angle provides the maximum slamming forces at for a given velocity. Since the slamming force is proportional with square of the velocity, and the velocity at second water entry is significantly lower, slamming forces for the first water entry is of main interest. (Truscott, et al., 2016)

2.6 Sail away phase

The main objective in the sail away phase is to get away from hazardous events. The ability to sail away from the evacuation scene is crucial and all the other phases will affect this phase. Here, the functionality of the lifeboat is described as a sailing vessel, that is resistance, maneuverability and stability. As the conditions are most likely to be challenging, the sail away performance must be of high standard, where the forward distance performance depends on the lifeboat initial motion right after resurfacing, which will be affected by waves. (Jin, et al., 2014)

2.7 Motion patterns

DNV-GL has identified four different main motion patterns for free falling lifeboat launches in calm water.

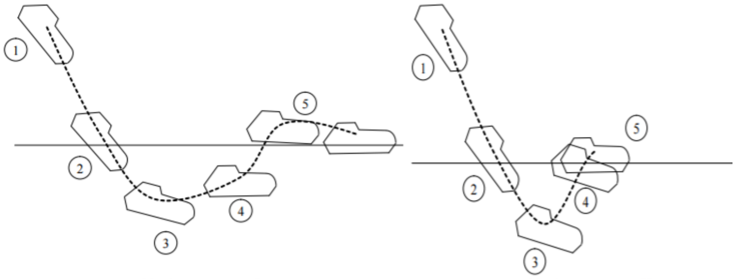

Motion pattern I Motion pattern II

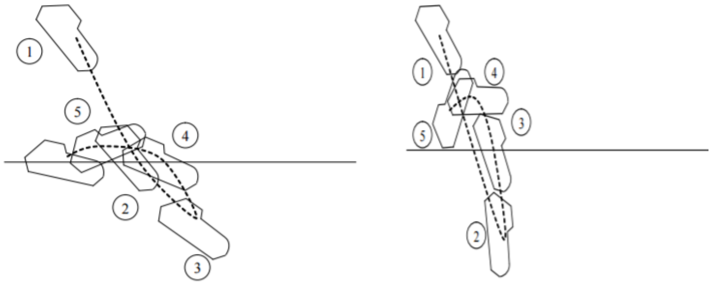

Motion pattern III Motion pattern IV

Figure 2.8: Motion patterns for a free-falling lifeboat

Where motion pattern 1, in Figure 2.8, is when the lifeboat pitches significantly at maximum submergence and ascent so that it surfaces with a positive forward velocity. Motion pattern 2, in Figure 2.8, is the same, but the forward velocity is reduced to zero and it surfaces with a negative (backward) velocity. Motion pattern 3 and 4, in Figure 2.8, is when the lifeboat moves backwards after reaching maximum depth in water, these two motions are often referred to as *log dive*, and should be avoided. (DNV-GL, 2016)

2.7.1 Log dive

Log dive is an unwanted water exit path where the body exits with aft part first. This can occur if the water entry angle is too large. Launching problems, wind loads and entry in a through can lead to an increased water entry angle. Also, the air cavity formation should stay intact in order to have the strong drag force, pulling on the lifeboat back into the entry trajectory, reversing the path. One criteria for log dive to occur is if the maximum negative longitudinal velocity in the ascent phase accommodate the following criteria

$$v_{x'} < -\sqrt{2g * VCG} \qquad [18]$$

$v_{x'}$ is the velocity in the body fixed x-direction, VCG is the vertical position of the center of gravity.

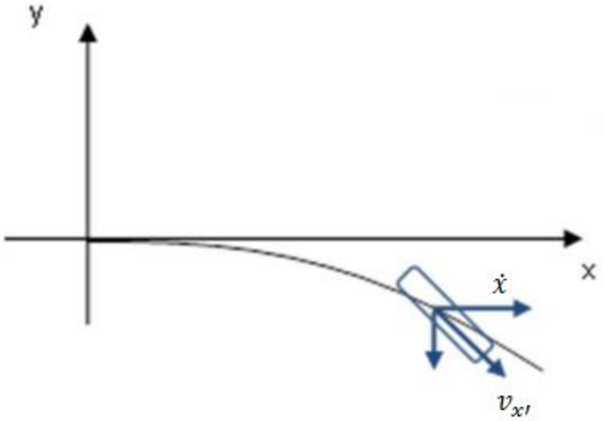

Figure 2.9: $\dot{x}$ is the horizontal velocity of the lifeboat and $v_{x'}$ is the sum of the horizontal and the vertical velocity components in the direction of motion. (DNV-GL, 2016)

2.8 Occupant safety

Accelerations induced on the lifeboat is important regarding the safety and comfort for the occupants. To ensure that the passengers does not get harmed by the induced acceleration, the lifeboat designer has to focus on complex combination of various relations like for example body sizes and seating.

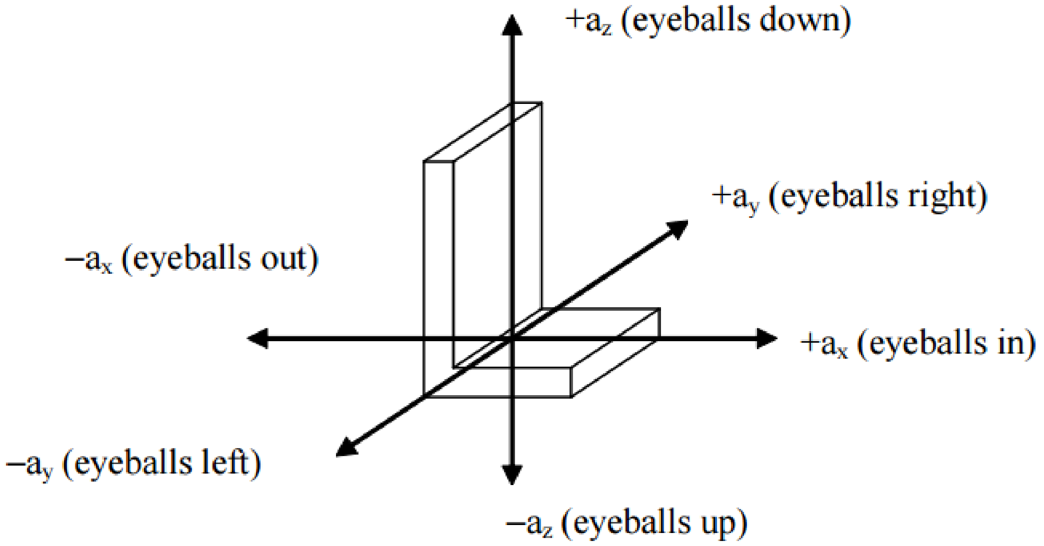

Figure 2.10: The local seat coordinate system (DNV-GL, 2016)

The basis for quantifying the acceleration induced loads on the human body in a free-fall lifeboat dive consist of acceleration components in the relevant directions. See Figure 2.10 for description of acceleration components a_x, a_y and a_z. An accepted criterion for occupant acceleration, is the Combined Acceleration Ratio (CAR), which is defined as

$$CAR = \max \sqrt{\left(\frac{a_x}{18g}\right)^2 + \left(\frac{a_y}{7g}\right)^2 + \left(\frac{a_z}{7g}\right)^2} \qquad [\,19\,]$$

18g, 7g and 7g is the normalization constants for the accelerations a_x, a_y and a_z, respectively.

- CAR$_1$ for out of seat acceleration – positive a_x values in the times series only.

- CAR$_2$ for into seat accelerations – negative a_x values in the times series only.

For into the seat acceleration it is recommended that the normalization constant a_x is reduced with 50% from 18g to 9g. A CAR value of less than one is defined as safe.

When interpreting the CAR index the acceleration data from the time series is to be filtered with a minimum 20Hz low-pass filter. A Butterworth fourth-order filter is to be used for filtering of the acceleration data, where the frequency domain transfer function, |H(f)|, is described as

$$|H(f)|^2 = \frac{1}{1 + \left(\frac{f}{20}\right)^4} \qquad [\,20\,]$$

where f is an arbitrary frequency (1/s). (DNV-GL, 2016)

3 Computational fluid dynamics

Computational fluid dynamics (CFD) is a branch of fluid mechanics that uses numerical analysis and algorithms to solve and analyze problems that involve fluid flows. CFD uses computers to perform the calculations required to simulate the interaction between the body and the fluid defined by the boundary conditions.

In a CFD process there are 5 to 6 main interconnected steps; 1) Geometry definition, 2) Surface grid generation, 3) Volume grid generation, 4) Flow calculation, 5) Data reduction, and 6) Experimental validation, if it can be provided. Then the software creates a second mesh, but now representing the volume occupied by the fluid, this is done to determine the behavior of the particles. After the meshes are finish, the software will set up a clear image on how the fluid will come in contact with the initial surface or object, while also emphasizing the exact problems encountered by it in the process. The software works to solve the Navier-Stokes problem, and afterwards the post-processing begins. It is assumed that the governing equations are valid. By applying the mass conservation equation and the momentum equation, four equation emerges and the pressure and the velocities in the three dimensions can be calculated. The results from CFD simulations are generally validated with previous experiments. (J. Andreson, 2009)

3.1 Governing equations in CFD

CFD calculations is based on solving the Navier-Stokes problem for four equations and four unknowns. The first of two equation that govern the fluid mechanics, is the conservation of mass. It described the balance of mass through a control volume. The equation for this is called the continuity equation and can be expressed as:

$$\frac{\partial \rho}{\partial t} + \frac{\partial}{\partial x_j}\left(\rho u_j\right) = 0 \qquad [\,21\,]$$

Where u_j is the velocity vector in all three directions, and the operator $\frac{\partial}{\partial x_j}$ is the respectively derivatives. It implies that the mass cannot be created or destroyed in a flow field. Hence, if there is a change in density there must be a change in the volume. It must be compressed or stretched in at least one direction, in order to conserve the mass in the control volume.

The other three equations can be expressed from

$$\frac{\rho D u_i}{Dt} = \frac{\partial \sigma_{ij}}{\partial x_{ij}} + \rho f_i \qquad [\,22\,]$$

This is the basic conservation law for momentum in fluid mechanics and is valid for every relation between deformation rates and viscous stress. The stress tensor vector can be written as

$$\sigma_{ij} = -p\delta_{ij} + \sigma' \qquad [\,23\,]$$

where the viscous stress tensor for Newtonian fluid, defined as “The resistance which arises from the lack of lubricity in the parts of fluid, other things being equal, is proportional to the velocity by which the part of the fluid are being separated from each other” (White, 2006) have the relation:

$$\sigma' = (\frac{\partial u_i}{\partial x_j} + \frac{\partial u_j}{\partial x_i} - \frac{2}{3} * \delta'_{ij} * \frac{\partial u_k}{\partial x_k}) \qquad [\,24\,]$$

δ'_{ij} is the two variables function, called the Kronecker delta. Its value is an integer, and equal to one if the velocity component changes in its defined direction, and zero if not, shown in equation [25].

$$\delta_{ij} = \begin{Bmatrix} 0 & if\ i \neq j \\ 1 & if\ i = j \end{Bmatrix} \qquad [\,25\,]$$

By inserting equation [24] into equation [23] and then into equation [22], the famous Navier-Stokes equation appears:

$$\rho \frac{Du_i}{Dt} = -\frac{\partial p}{\partial x_i} + \frac{\partial}{\partial x_j}\left[\mu\left(\frac{\partial u_i}{\partial x_j} + \frac{\partial u_j}{\partial x_i} - \frac{2}{3}\delta_{ij}\frac{\partial u_k}{\partial x_k}\right)\right] + \rho f_i \qquad [\,26\,]$$

In the case of constant fluid density, which is assumed in most CFD calculation for free fall lifeboats equation [26] can be reduced to:

$$\rho \frac{Du_i}{Dt} = -\frac{\partial p}{\partial x_i} + \mu \nabla^2 u_i + \rho f_i \qquad [\,27\,]$$

(Ytrehus, u.d.) (White, 2006) (J. Andreson, 2009)

3.2 Previous work with the use of CFD for free-falling lifeboats analysis

Since free falling lifeboats mainly operates at sea, experimental results for typical north-sea waves is hard to come by. Here CFD is a valuable resource for calculating forces, accelerations, path and other parameters and features.

3.2.1 Validation of CFD with experiments

Tregde (2015) ran CFD simulations of a free-falling lifeboat which started 0.5m above water level, and with initial conditions received from previous CFD simulations. The trajectory of the lifeboat is assumed to be governed by the Reynolds averaged Navier-Stokes equations in which turbulence effects are included. In the simulations some simplifications were made, such as;

- Water is assumed to be incompressible
- The lifeboat geometry is somewhat simplified to ease the meshing
- The lifeboat is assumed to be a rigid body, hydroelastic effects are not taken in account
- Air is assumed to be either incompressible or compressible with ideal gas relation
- Implicit 1st order time scheme has been used.

The simulations were compared with experimental results, where the compressible CFD simulations compared with the full scale experimental data showed good correlation for pressure on the top of canopy, figure 7 and 8 in the paper.

Tregde concludes that incompressible flow simulations would give reliable results for motions, accelerations and most pressures, except in the aft sections of the vessel, where the compressed air bubble makes a big difference. (Tregde, 2015)

3.2.2 Free-falling lifeboats in waves

Berchiche, et al. (2015) ran 12 cases for a free falling-lifeboat in waves with CFD simulations, were the waves had different headings and hit point locations, seen in table 2 in the paper. It should be noted that the simulations were done with laminar flow, with Reynolds-Averaged Navier-Stokes (RANS) and an implicit unsteady model with second order time scheme. Also there it was concluded that the CFD simulations were able to predict the motions, accelerations and pressures of the lifeboat during water entry into waves of various directions. Similar as Tregde (2015), Berchiche, et al. (2015), also states that for the local pressures at places where air-cavities are formed and then collapse, such as the aft wall of the lifeboat, it is necessary to model the air as compressible. (Berchiche, et al., 2015)

3.2.3 Sail away phase

The work is done by Jin, et al., (2014). The forward distance performance of a free-falling lifeboat after water exit is addressed. A numerical study with irregular sea state under constant wind and current velocities has been used. Three weather directions, two autopilot settings and different initial motion conditions of the lifeboat are considered in the simulations. The waves are modeled using the JONSWAP spectrum, where the waves have no directional spreading and the wave forces included are of first-order. The current and the wind has a constant velocity. The current forces are implemented by superposing the current velocities onto the local forward and transverse velocities onto the local forward and transverse velocities through the sea. The sea state is represented in table 2 in the paper. Within this weather data the directions considered was: head sea, bow quartering sea and beam sea.

The two autopilot system headings were set to against the weather and the other is along the launch direction. They are represented in table 3 in the paper.

The results obtained from the simulations, shows that the forward distance performance depends on the lifeboat initial motion right after resurfacing of the forward distance simulation. Positive initial surge velocity and small initial yaw angle gives better forward distance performance compared to those with negative surge velocity and large yaw angle. When the desired heading is set to along launch direction, the forward distance is observed best in beam sea condition, and the transverse motion is observed smallest in head sea condition. For the bow quartering and beam sea the transverse motion is quite similar. With positive surge velocity and negative initial yaw angle, the lifeboat is able to turn straight against weather without drifting sidewise. Some important aspects have been identified in the paper, such as that the lifeboat can be pushed backwards before gaining forward distance in some cases, and that the drift motion can be difficult to avoid in bow quartering and beam seas. (Jin, et al., 2014)

3.3 Star-CCM+

Berichiche, et al. (2015) and Tregde (2015) used the software Star-CCM+ when simulating with CFD and free-falling lifeboats, therefore Star-CCM+ is a reasonably choice of software. The software is developed by CD-Adapco and features step-by-step tutorials to minimize the steep learning curve of the software.

3.3.1 Physics

To get the most realistic results from the CFD simulations, the physics are carefully selected. This involves volume discretization, turbulence models, interface capturing, wall Y^+equations, Courant number validation and boundary conditions. Star-CCM+ is a leading software in the matter of CFD analysis, it is a commercial code, and later theories are related to this software.

3.3.1.1 Transport equation

Star-CCM+ uses the governing equation in fluid mechanics and transforms it in to a set of algebraic equations. For this transformation, the equations have to be discretized in space and time. Then the resulting linear equations are solved by an algebraic multigrid solver. A closed set of equations are obtained after introducing an appropriate constitutive relation into the conservation equation. The integral form of the transport equation, equation [28], is obtained by integrating the generic transportation problem over the control volume and applying Gauss divergence theorem:

$$\frac{d}{dt}\int_V \rho\phi dV + \int_A \rho\boldsymbol{v}\phi \cdot d\boldsymbol{a} = \int_A \Gamma\nabla\phi d\boldsymbol{a} + \int_V S_\phi dV \qquad [\ 28]$$

Where the first term is the transient term, the second term is the convective flux, the third term is the diffusive flux and the fourth term is the source term. V is the control volume ϕ is the transport of a scalar property, $\boldsymbol{A}$ is the surface area of the control volume and $d\boldsymbol{a}$ represents the surface vector, Γ is the diffusion vector and S_ϕ is the source term.

3.3.1.1.1 Segregated flow solver

To solve the integral conservation equation of mass and momentum in a sequential manner, the segregated flow solver can be used. Then by iteration process the non-linear governing equation are solved for the solution variables, that is the velocities and the pressure. A pressure correction equation is solved to fulfil the mass conservation constraints on the velocity field used in the employed pressure-velocity coupling algorithm. The momentum equation and the continuity equation is used for the construction of the pressure correction equation. Then the predicted velocity field fulfils the continuity equation, this is achieved when correcting the pressure. The pressure correction equation also obtains the pressure as a variable.

3.3.1.2 Turbulence model

In Star-CCM+, there are currently four major classes of Reynolds-Average Navier-Stokes (RANS) turbulence models, which are time averaged equation of motion for fluid flow.
To obtain RANS equation, the Navier-Stokes equations for the instantaneous velocity and pressure field are decomposed into a mean value and a fluctuating component. “The averaging process may be though of as time averaging for steady state situations and ensemble averaging for repeatable transient situations.” (Steve CD adapco, 2016)

3.3.1.2.1 Spalart –Allmares

It is applicable for cases where the boundary layers are largely attached and separation is mild if it occurs. It is often used in connection with aerospace external flow applications, like flow over a wing. This turbulence model is not suited for flows dominated by free share stress layer in connection with complex recirculation. Therefore, this turbulence model is not of interest, due to separation on the aft part of the lifeboat. (Steve CD adapco, 2016)

3.3.1.2.2 K-Epsilon model

The K-Epsilon turbulence model is a two-equation model that determines the turbulent viscosity. This is done by solving the transport equations for the turbulence kinetic energy $\boldsymbol{k}$ and its dissipation rate ϵ. According to Star-CCM+, this turbulence model provides a good comparison between robustness, computational cost and accuracy. Unlike the Spalart–Allmares model, K-Epsilon are suited for complex recirculation, with and without heat transfer. (Steve CD adapco, 2016)

3.3.1.2.3 K-Omega model

The K-Omega model and K-epsilon both solve two transport equations. The main difference is the choice of the second transported turbulence variable. The K-Omega model has improved performance for boundary layer under adverse pressure gradients, compared to the K-Epsilon model. This is perhaps the most significant advantage for the K-Omega model. In the K-Omega model original form, the largest disadvantage is that the boundary layer computations are very sensitive of the specific dissipation rate (ω) in the free stream. This leads to extreme sensitivity in the inlet boundary conditions for internal flows. This problem is not present for the K-Epsilon model. (Steve CD adapco, 2016)

3.3.1.2.4 Reynolds stress transported model

According to Star-CCM+, it is the most complex and computationally expensive models offered. It is best suited for situations where the turbulence is strongly anisotropic. This is highly relevant for the swirling flow in a cyclone separator (Cyclonic separation is a method of removing particulates from an air, gas or liquid stream). (Steve CD adapco, 2016)

3.3.2 Free boundaries approximations

For fluid dynamics, both Langrangian and Eularian coordinates are commonly considered. The Langrangian coordinate system is following the fluid particle at each point, and then the fluid properties are determined as the fluid particle is moving. The Eulerian coordinate system is just observing the fluid properties as a function of time and space. Lagrangian coordinates are most common to use as basis for numerical solution algorithms in connection with structural dynamics. Eularian coordinates are often used since the free boundaries undergo such large deformations that Lagrangian methods cannot be applied. Free boundaries are often referred to as surfaces where discontinuities exist in one or more variable. Shock waves and interfaces between fluid and deformable structures are example of free boundaries. The problems related to numerical treatment of free boundaries can be divided into three; their discrete representation, evolution in time and the way boundary conditions are imposed on the free boundaries. (Hirt & Nichols, 1979)

3.3.2.1 Volume of fluid method

There are varies ways to approximate free boundary in finite numerical simulations, but the most common method is based on the concept of a fractional Volume Of Fluid (VOF). This method defines a function F. Its value is of unity if the point of interest is fully occupied with fluid, and otherwise zero. For a distinctive cell, represented by several points, the average value of F will then represent the volume fraction of the cell occupied by the fluid. A cell that only contains fluid will have the value of unity, while a zero value represent no fluid. Hence, if F has a value greater than zero and smaller than one, it implies that the cell must contain a free surface. The VOF method solves the transport equation for the volume fraction F of the occupied liquid in each cell in the grid (see equation [29]). Only one value for the fractional volume is required for each cell, where the fractional volume at the current time step in each cell is located using the velocity field and fractional volume at the previous timestep. This method is time efficient and beneficial due to the fact that it only requires one storage word for each cell. In addition to identify the cells with boundaries, it is important to know where the fluid is located at the boundary. This is predicted only by the scalar fractional volume value and the filling state of the cells sharing a common side, which is considered as the methods main draw back.

$$\frac{\partial F}{\partial t} + u * \frac{\partial F}{\partial x} + v * \frac{\partial F}{\partial y} = 0 \qquad [\ 29\ ]$$

Equation [29] is an example of the derivations of the transport equation for two-dimensional cases, where F moves with the fluid. This can readily be extended to three dimensional calculations.

When both the value of F and the direction of the boundaries are known, a line separating the cell can be constructed to represent the interface, which further can be used when setting the boundary conditions. For cases related to surfaces where the fluids do not remain fixed, but have relative motion in addition, the equation above must be modified. Handling of boundaries between single face and two face fluid regions and shockwaves are examples for when the equation must be modified. (Hirt & Nichols, 1979) (Faltinsen & Timokha, 2009)

3.3.3 Wall Y^{+}

The non-dimensional wall distance, Y^{+}, for a wall bounded flow is given as

$$Y^{+} = \frac{y u_{\tau}}{\nu} \qquad [\ 30\ ]$$

u_{τ} is the frictional velocity at the body, y is half the cell height closest to the body and ν is the local kinematic viscosity (m^2/s) of the fluid. It is commonly used for boundary layer theory and the non-dimensional velocity u^{+} is given as

$$u^{+} = \frac{u}{u_{\tau}} \qquad [\ 31\ ]$$

Where $u_{\tau} = \sqrt{\frac{\tau_W}{\rho}}$ and τ_W is the shear stress.

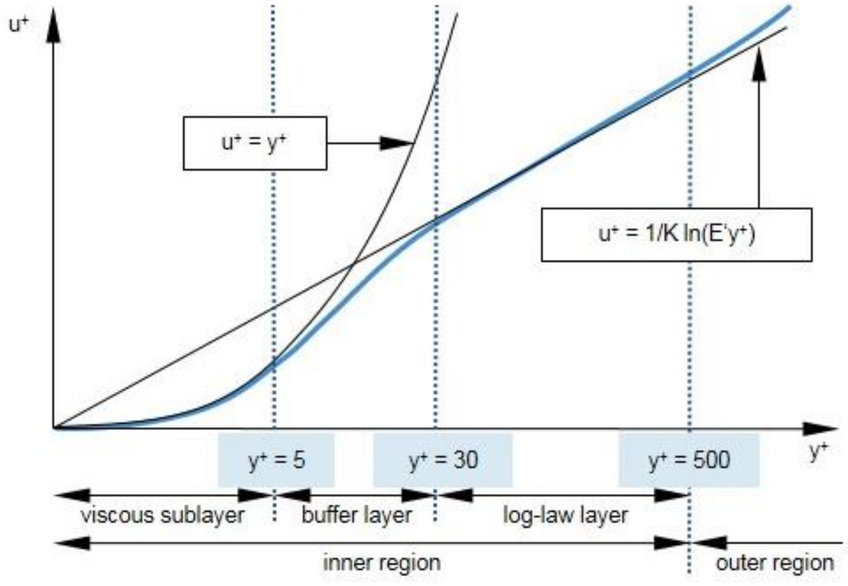

Figure 3.1: Correlation between Y^+ and u^+ (Steve CD adapco, 2016)

The logarithmic layer from Figure 3.1 can be described as:

$$u^+ = \frac{1}{\kappa}\ln(E'y^+) \qquad [\,32\,]$$

Where κ is the von Karman's constant, approximately equal to 0,42. $E' = \frac{E}{f}$ where E is a coefficient equal to 5,1 and f is the roughness form function. Figure 3.1 shows that u^+ follows the relation of Equation [32] after as Y^+ passes the value of approximately 30. (J. Andreson, 2009) (Steve CD adapco, 2016)

Regarding the wall treatment, three different settings can be chosen in Star-CCM+, this depends on the value of Y^+. If the value is in the viscous sublayer, that is $Y^+ < 5$, the" low Y^+" setting should be used. Often utilized when:

- The accurate prediction of the boundary layer velocity and/or temperature profile is important.
- Simulation time and therefore cell count is not a critical issue.

If the value is in the “log-law layer”, that is $Y^{+} > 30$, the “high Y^{+} should be used. Beneficial to utilize when:

- The wall roughness effect must be included.
- Simulation time and cell count is of critical issue.

A third setting is the “all Y^{+}”. It is a hybrid treatment that uses both the low and high Y^{+} treatment. For the buffer layer $1 < Y^{+} < 30$ it uses a blending function and gives reasonable solutions for low values in the buffer layer. It is beneficial to choose this setting when Y^{+} is varying due to varying geometry and velocity scale associated with the model. (Steve CD adapco, 2016)

3.3.4 Courant Friedrichs Lewy Number

The formula for the dimensionless CFL (Courant Friedrichs Lewy) number is given as:

$$CFL = \frac{u\Delta \mathrm{t}}{\Delta x} \qquad [\,33\,]$$

It gives an indication of the ratio between the simulated fluid distance for a given time step, Δt, and the length of one cell, Δx. For every time step, Δt, the Navier-Stokes equations are solved by the iteration process. If the CFL number has a value smaller than one, it implies that there will be at least one solution for each cell. For a moving mesh, such as overset meshes, u is defined as the velocity relative to the mesh in Star-CCM+. Small CFL are advantageous for the quality of the solution, but as a compromise for the computational calculation time, some increase must be tolerated. (Steve CD adapco, 2016)

The CFL number is of interest where the body intersect with the surrounding fluid. Due to the change in density across the cell in a free surface, a low time step is important to ensure robustness for the interface capturing of the free surface. This can be showed by a simplified momentum equation for incompressible, isothermal and immiscible fluids, where the flow does not have pressure and velocity gradients. The momentum equation then reduces to

$$\frac{\partial u_i \rho}{\partial t} = -\nabla \rho u_i u_i \qquad [\ 34\ ]$$

Seen from equation [34], a change in density across the cell will lead to change in the acceleration. Large difference in the density within a cell combined with a time step too "coarse" can therefore lead to unrealistic large accelerations. The fluid will in addition accelerate when it passes sharp corners. Hence, numerical instabilities are most pronounced when sudden changes in geometry (like sharp corners) intersect with the free surface. (Kim & Park, 2016)

3.4 High Performance Computers

With the use of CFD calculations the need of processing power increases with the amount of cells in the simulation. Here high performance computers (HPC) will be valuable. With the use of these computers, more accurate simulations is possible, and the time before the results is available for the user decreases.

Vilje is NTNU's HPC and has 1404 nodes with two hyperthreaded eight-core processors per node of the type Intel Xeon E5-2670 ('Sandy Bridge'), which results in a total of 22 464 cores. There are 32GB RAM attached to each node. (NTNU HPC Group, 2016) As the simulation goes downwards in mesh size and time step, more CPU power is required. Vilje is que based where the job is submitted with a wall time and a number of processors that shall be used, an advice from Andrea Califano was that the simulations should at least have one processor per 30 000 cells. Which was extended to roughly 40 000 cells per processor to reduce que time at Vilje.

By using Vilje, one encountered limitation was the mesh operation, since this operation had to be done beforehand. For this operation, an Asus Zenbook U500V with Intel® Core™ i7-3612QM processor and 10 GB RAM was used. Star-CCM+ recommended approximately 1 GB RAM per 500 000 cells for this study's mesh configurations, which results in a maximum of 20 000 000 cells in the simulations. (Steve CD adapco, 2016)

4 Pre-Processing

In order to establish the accurate solutions for the simulations, a geometry, mesh configurations, boundary conditions and physics has to be interpreted into Star CCM+.

4.1 Geometry

For the simulations of a free-falling lifeboat, a simplified geometry was chosen. The reason for the simplification is to not complicate the process with appendages such as a wheelhouse. Still, the essence of the behavior of the body will be similar to an actual lifeboat. This gives valuable training in simulating free fall lifeboat diving. The geometry chosen is therefore an ellipsoid, Figure 4.1, with specifications in Table 4.1.

Figure 4.1: Simplified geometry

PARAMETERS	VALUES	DIMENSIONS
LENGTH	10	m
DIAMETER	3	m
MASS	23561.9	kg
VOLUME	47.1	m^3
I_X	21205.8	$kg*m^2$
I_Y	481841.8	$kg*m^2$
I_Z	481841.8	$kg*m^2$
I_{XX}	21205.8	$kg*m^2$

I_{YY}	150501.9	kg*m^2
I_{ZZ}	150501.9	kg*m^2
R_{XX}	0.949	m
R_{YY}	2.527	m
R_{ZZ}	2.527	m
COG_X	3.75	m
COG_Z	-0.5	m

Table 4.1: Simplified geometry properties taken from the body fixed coordinate system

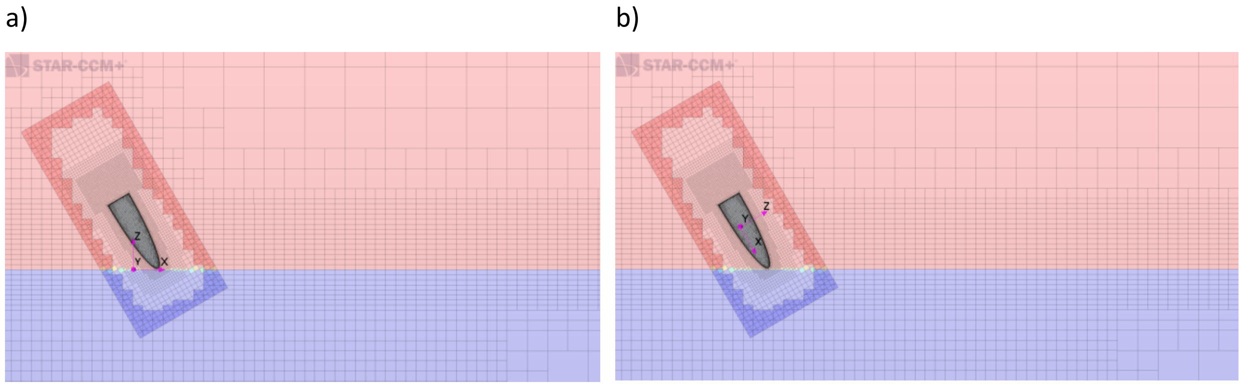

Figure 4.2: Visualization of the coordinate systems, a) is the global coordinate system and b) is the body fixed

Figure 4.2 a) shows the global coordinate system where the origin is located at [0, 0, 0] at all times in the simulations. The body-fixed coordinate system shown Figure 4.2 b), will be located in the body centre of gravity, and will follow the motion of the body. The different coordinate systems will be referred to as n_{global} for the global coordinate system and n_{body} for the body fixed, where n = x, y or z.

4.2 Boundary conditions

In order to get results that matches a realistic solution, the boundary conditions applied to the different regions in the CFD simulation must be defined. These conditions define the inputs of the simulation model. Whether the fluid flows around or through the body in question, or if the fluid enters or leaves the domain. Hence the boundary conditions connect the simulation model with its surroundings.

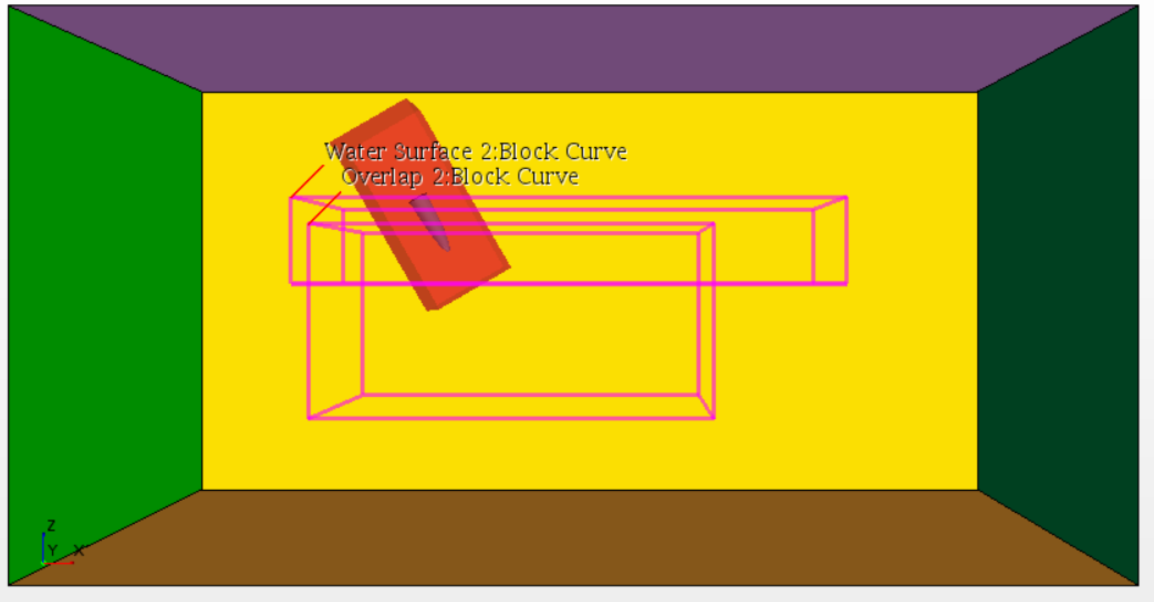

Figure 4.3: Boundary conditions illustration

Figure 4.3 shows the domain chosen for this study. Bright green is labelled as "inlet", green as "outlet", purple as "top", brown as "bottom", yellow as "port", red as "overset", and the transparent as "starboard". In Figure 4.3, two additional areas are highlighted. The upper one is the "water surface" and the lower one the "overlap". Their different dimensions are found in

NAME OF THE PART	CORNER 1 DIMENSION (x, y, z) $[m, m, m]$	CORNER 2 DIMENSION (x, y, z) $[m, m, m]$	CELL SIZE IN 0,08m MESH $[m]$
BOUNDARIES	-50, -40, -45	100, 40, 32	5.12
OVERLAP	-15, -20, -25	45, 20, 4	0.64
WATER SURFACE	-18, -18, 8	65, 18, -5	0.64, 0.64, 0.32
OVERLAP OVERSET	-18, -11, -11	10, 8, 8	0.64
OVERSET	-17.5, -7, -7	13.25, 7, 7	0.32
BOX BEHIND	-8.5, -3.5, -3.5	-3.75, 3.5, 3.5	0.08

Table 4.2: Dimensions for each part in the simulation, where Overlap Overset, Overset and Box Behind is measured in the body fixed coordinate system, while the rest of the parts in the global coordinate system

Port, starboard, top, bottom, inlet, outlet, water surface and overlap will be referred to as the domain, while overset and the lifeboat will be referred to as it is. This is due to the set up in Star-CCM+ where they are assigned as two separate regions.

In Star-CCM+, the domain was assigned as one region with different boundaries, were as the inlet, top and bottom is assigned as velocity inlet. The velocity inlet represents the inlet of a duct for a known flow velocity and is therefore set to zero in this case, as there is no initial current or velocity flows. The outlet of the domain is assigned as pressure outlet. The boundary face velocity is extrapolated from the interior using reconstruction gradients. The boundary condition for the lifeboat is set to wall. There will be no slip at this boundary, meaning that the fluid attached to the boundary will follow the body, resulting in a boundary layer with thickness δ and velocity gradients.

The lifeboat is impermeable, hence there will be no fluid passing through this boundary. Port and starboard side of the domain are assigned as symmetry plane. The symmetry plane can be seen as walls, due to the impermeability. However, slip condition is applied, which results in zero shear stress. The assigned parts should be placed such that the velocities at the boundaries is equal to the inlet velocity, resulting in zero velocity gradients close to the assigned parts. Large velocity gradients close to or in the boundaries will influence the simulations, therefore a large domain for this case was necessary. The overset is the interaction between the two regions, domain and lifeboat, and is where the volume to solve on is generated. For the interaction between the domain and overset to work properly, the mesh size in the overset cannot be smaller than half of the mesh size in the overlap region. (Steve CD adapco, 2016)

4.3 Mesh configurations

In order to get accurate results, a good mesh configuration is needed. In this thesis, a region based meshing was used combined with the Star-CCM+ overset mesh, where the overset mesh follows the body. The overset mesh describes how the regions in the simulation are related to each other, it creates an interface between the background (domain) and the body in question (the lifeboat). The mesh is generated with surface re-mesher, trimmer and prism layer options are enabled. Surface re-mesher uses the existing surface and optimizes it for the volume mesh models. The trimmer model is used to provide a robust and efficient method of producing a high-quality grid for both simple and complex mesh generation problems. Here hexahedra cells were used with smaller cells closer to the body such that all data were captured. The prism layer model is used with the two other models to generate orthogonal prismatic cells next to wall surfaces or boundaries. This layer of cells is necessary to improve the accuracy of the flow solution, due to better capturing of velocity gradient and viscous effects. It should be pointed out that the mesh operation is time-consuming, since the solving area should be large enough, such that near-wall disturbances do not occur. In this case it will be the lifeboat inside the overset region. The complete mesh is shown in Figure 4.4.

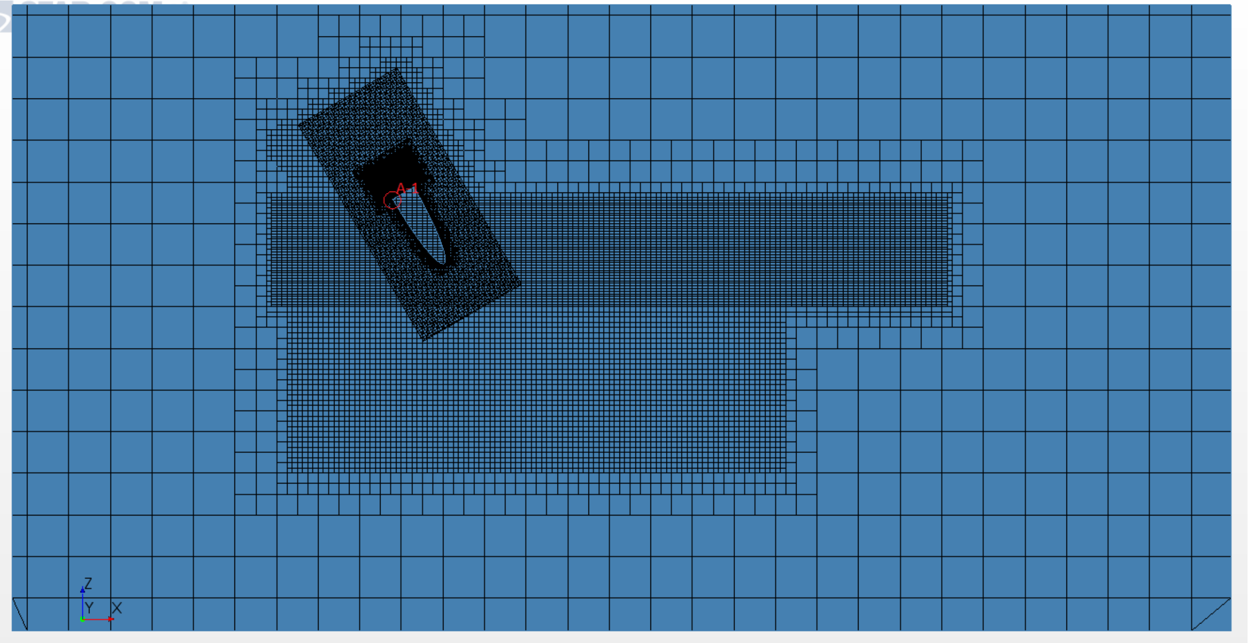

Figure 4.4: Mesh

As mention in section 3.3.3 Wall Y$^+$ **,** the closest cell to the body should be so small that the wall Y$^+$ value is within the region of the selected model. This was done using the prism layer model, as mentioned, where the total height, number of prismatic layers and height for the cell closest to the body were inserted into Star-CCM+. The total height of the prism layers is influenced by the number of prism layers, and this number was recommended by Star-CCM+ user guide to ensure a stretch factor over the cells to be between 1.3 and 1.5. Though the simulations were conducted with varying mesh size, the cell height closest to the body were kept constant in the prism layer, hence small changes for the Y$^+$ values.

$$X_h = x_{min} * \sum_{n=0}^{N} f_{stretch}^{n} \qquad [\ 35\ ]$$

Equation [35] shows how the prism layer height, X_h, is obtained from the minimum cell size, x_{min}, and stretch factor, f_{strech}. To ensure a smooth transition between the prism layer and the surrounding mesh the total height of the prism layer and the last cell in the prism layer is close to the size of the first cell outside the prism layer, as seen in Figure 4.5.

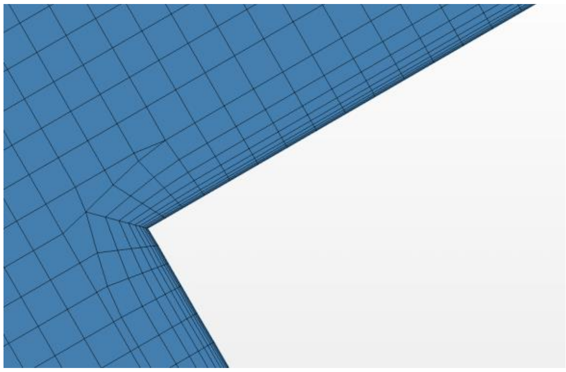

Figure 4.5: Prism layer illustration on the corner, cut-out A-1 from Figure 4.4

To capture the behaviour of the air cavity formed on the aft, a refined mesh was applied here, as seen in Figure 4.6**.**

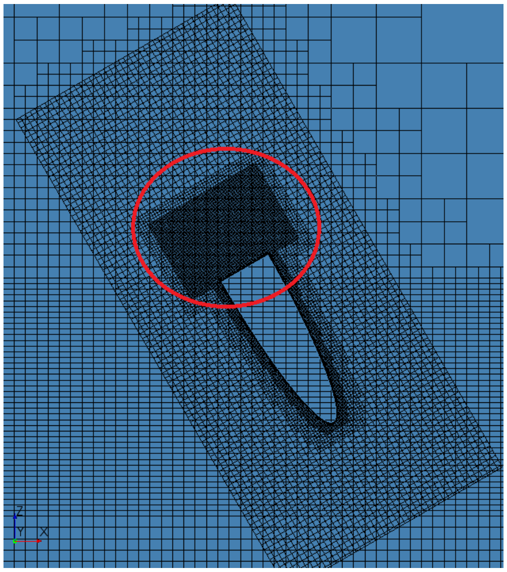

Figure 4.6: Refined mesh on aft part inside the overset

4.4 Applied physics

As described in section 3.3 Star-CCM+ offers a large variety of physics modules. In order to narrow the modules down for the case of a free-falling lifeboat, the work done by (Berchiche, et al., 2015), (Califano & Brinchmann, 2013) and (Tregde, 2015) has been used as guidelines. For this thesis the main physic modules are found in Figure 4.7.

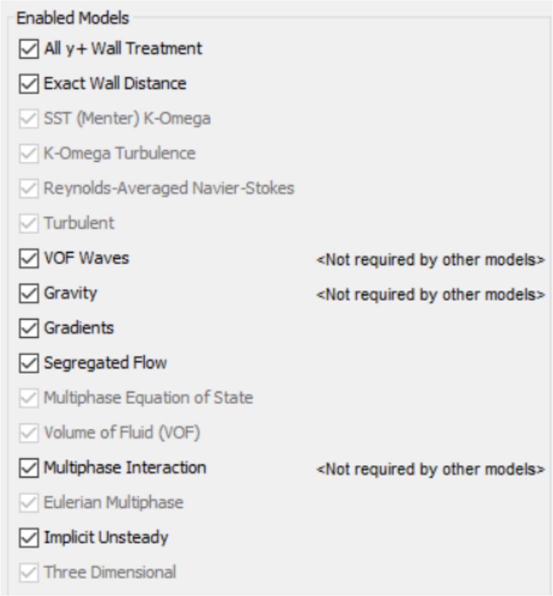

Enabled Models

☑ All y+ Wall Treatment
☑ Exact Wall Distance
☑ SST (Menter) K-Omega
☑ K-Omega Turbulence
☑ Reynolds-Averaged Navier-Stokes
☑ Turbulent
☑ VOF Waves <Not required by other models>
☑ Gravity <Not required by other models>
☑ Gradients
☑ Segregated Flow
☑ Multiphase Equation of State
☑ Volume of Fluid (VOF)
☑ Multiphase Interaction <Not required by other models>
☑ Eulerian Multiphase
☑ Implicit Unsteady
☑ Three Dimensional

Figure 4.7: Main applied physics in the simulations

For the simulations discussed in 3.2 Berchice et al. (2015) used a laminar flow, Califano & Brinchmann (2013) used a K-Omega module and Tregde (2015) a K-Epsillon module. Simulations with different turbulence models were conducted, where the difference in path and acceleration were unnoticeable. K-epsilon had longer solving time then K-omega for the same time step, but tolerated a higher time step before the simulation diverged. The reason for the all Y^+ treatment, was due to the density difference in water and air causing huge variation for the Y^+ at the same time instance, resulting in some values lower than 30. Y^+ values outside the log layer relation is less realizable for high Y^+, as mentioned in section 3.3.3 Wall Y^+. Therefore, a hybrid version of low and high wall Y^+ where chosen.

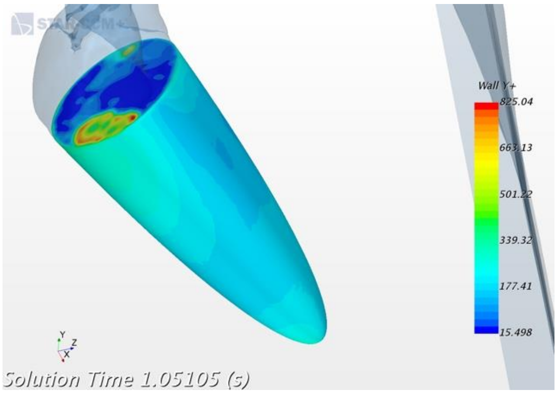

Figure 4.8: In the aft part of the body, air is still entrapped after 1.05 seconds, though the body is fully submerged, results in Y^+*values below 30.*

Both (Califano & Brinchmann, 2013) and (Berchiche, et al., 2015) used an implicit unsteady time scheme with second order temporal discretization. An unsteady time scheme with second order temporal discretization have been applied for all the simulations conducted with incompressible air. The interface technique has been VOF for all the simulations, where the basic concept regarding this method is mentioned in section 3.3.2.

The solver chosen is the segregated flow solver, mentioned in section 3.3.1.1. It should be noted that the segregated flow solver can handle mildly compressible flows and low Rayleigh number natural convection, but it is not suitable for shock capturing, high Mach number and Rayleigh number amplifications. (Steve CD adapco, 2016)

5 Sensitivity & Convergence

In order to get accurate results, it is necessary to determine a time step that correlates with the grid and mesh size. In addition, a sufficient amount of iterations for each time step has to be obtained, such that each time step converges.

A convergence study has been conducted to see how the cell size in the grid affects the solution. It is assumed that the solution is improved by decreasing the cell size. A convergence study is also useful for selecting the mesh size with respect to solution quality and computational time.

5.1 Sensitivity Analysis

The sensitivity analysis has been conducted for the mesh with the lowest number of cells. This is for the sake of the low CPU cost, and acceptable results for the purpose.

5.1.1 Residuals

The residuals indicate how well the governing equations for each solver quantity are being satisfied numerically. This will be different for each simulation due to the varying Δt, but as the Star-CCM+ user guide states: The amount that a residual decrease is dependent on the particulars of the simulations. Therefore a drop of 3-4 magnitude in the residuals might be sufficient for one simulations, but not for another. (Steve CD adapco, 2016) This does not indicate that the solution necessarily is the correct one, but the correct one for that mesh size with the corresponding Δt.

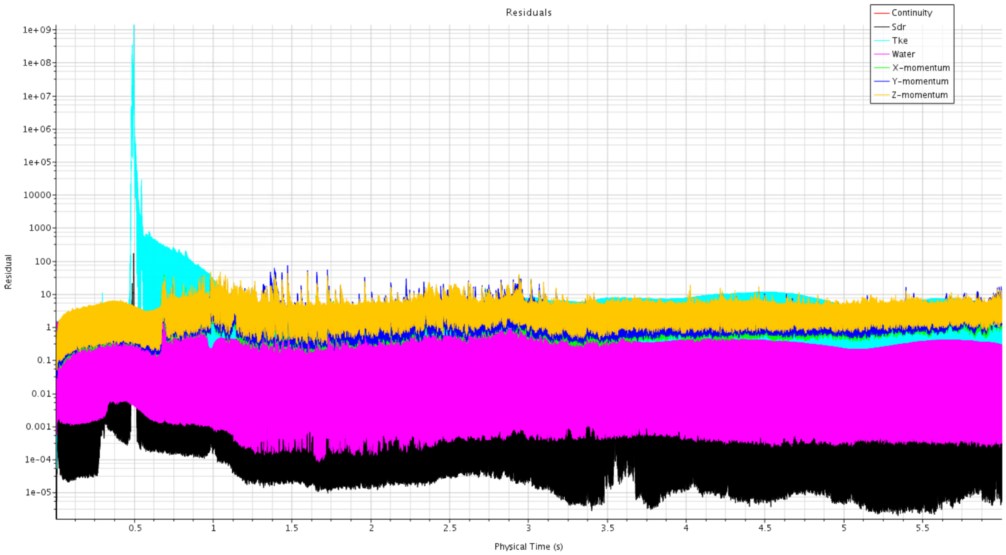

Figure 5.1: Residuals for the whole simulation with Δt =1.2ms and 10 inner iterations.

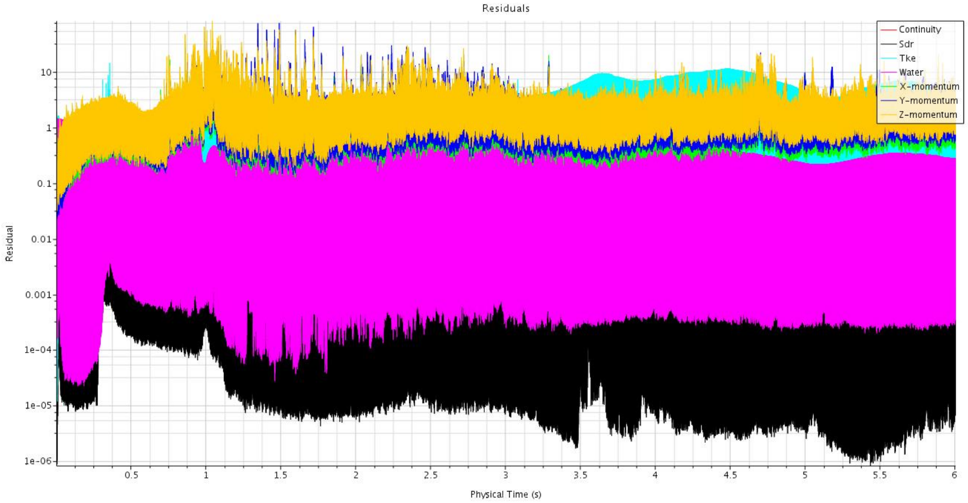

Figure 5.2: Residuals for the complete simulation with Δt=0.6ms and 10 inner iterations

By comparing the residuals values for each of the two time steps, Figure 5.1 and Figure 5.2, it is possible to see that the solver gets better residual values for lower time steps. The most critical area for the solver is around 0.3 s - 0.6 s, in the transition between water entry phase and submerged phase. As for the two time steps, 1.2 ms and 0.6 ms, the difference between the residuals in this critical region is in the order of approximately 10^9. Mentioned in 3.3.4, unphysical numerical solution might occur for sudden changes in geometry in connection with interaction with free surfaces, if the time step is not sufficiently low. Seen from Figure 5.1, the turbulence model (Tke) seems to diverge after approximately

0.45 s. This is when the sharp corners on the aft part of the body gets submerged, and unphysically high fluid accelerations may influence the robustness of the turbulence model. Therefore, the lowest time step of 0.6 ms was chosen to correspond with the coarsest grid.

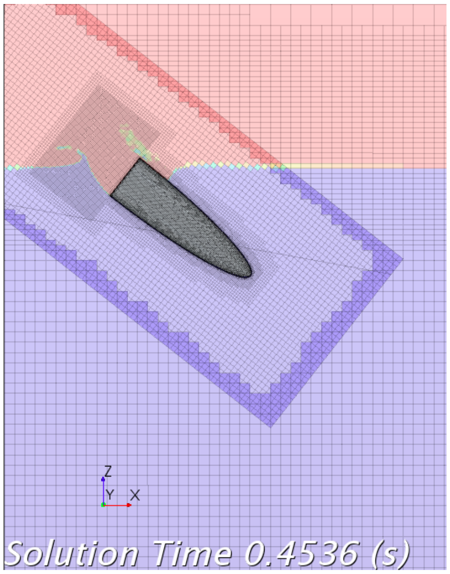

Figure 5.3: VOF picture approximately from where the turbulence model starts to diverge for larger time steps, even though the time steps are relatively small

5.1.2 Number of iterations

The maximum inner iteration is based on the number of inner iterations that the solver executes for transient analyses. As for the 6-DOF solver, it computes fluid forces, moment and gravitational forces on a 6-DOF body, in this case the lifeboat. Pressure and shear forces are integrated over the surface of the lifeboat. The forces and moments acting on the 6-DOF body are used to compute the translational motion of the center of mass of the body and the angular motion of the orientation of the lifeboat.

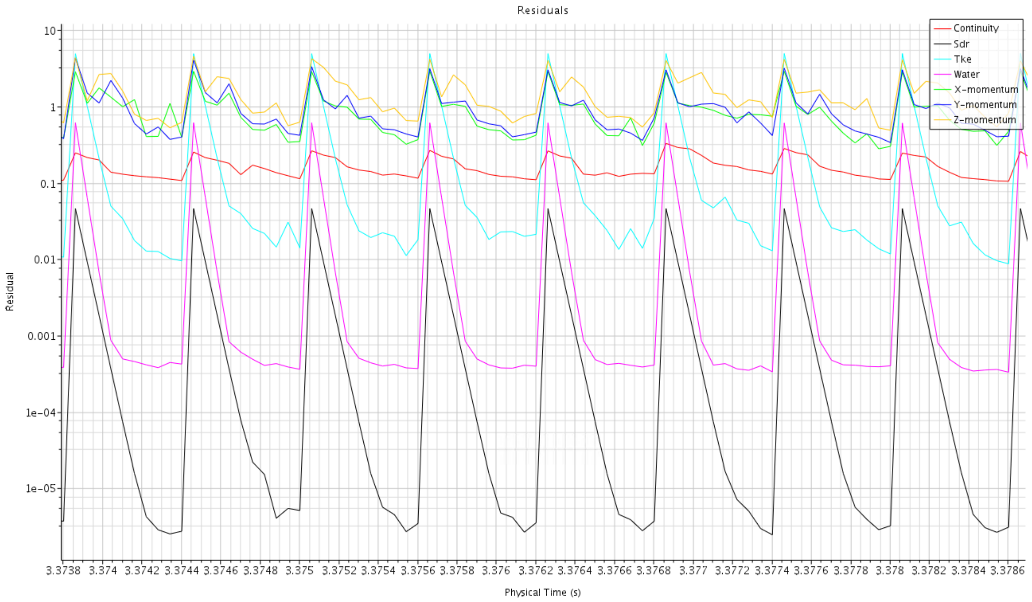

Figure 5.4: Residuals where the iterations for each time step is showed

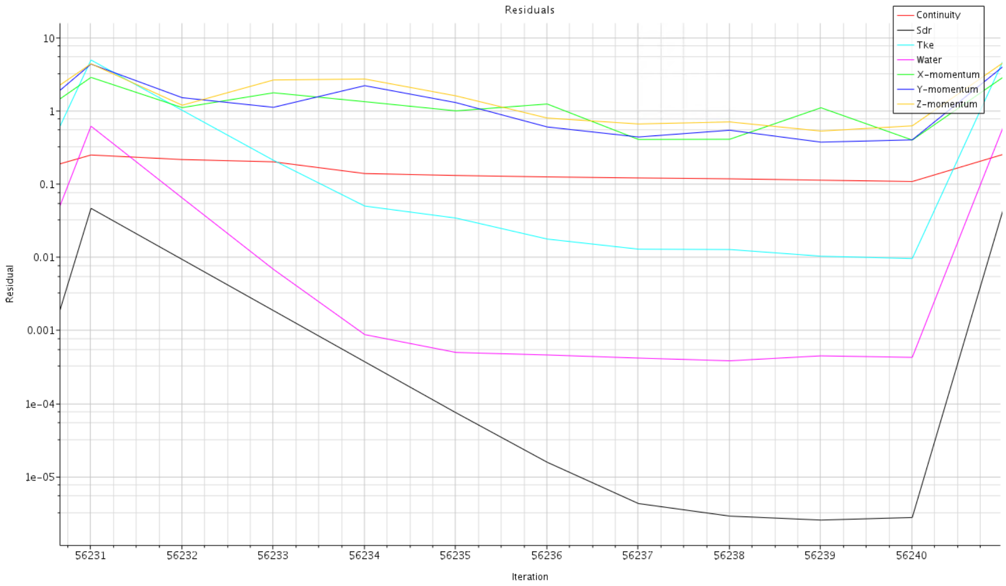

Figure 5.5: Residuals for one time step

An analysis to find the most efficient and precise number of inner iterations were conducted for respectively 6, 10 and 14 inner iterations. All the simulations were conducted with the same mesh and grid configuration for a time step of 0.6 ms, which was found from 0. With 10 inner iterations, the residual values seem to flatten out and converge at the end of each Δt after approximately 8-9 inner iterations, as seen in Figure 5.4 - Figure 5.5. Hence, 10 iterations are chosen as a basis for the varies simulations and 4 DOF-solver iterations.

5.1.3 CFL number analysis

Two different simulations with a time step of 1.2 ms and 0.6 ms were conducted to determine the sensitivity of the simulation with respect to the CFL value.

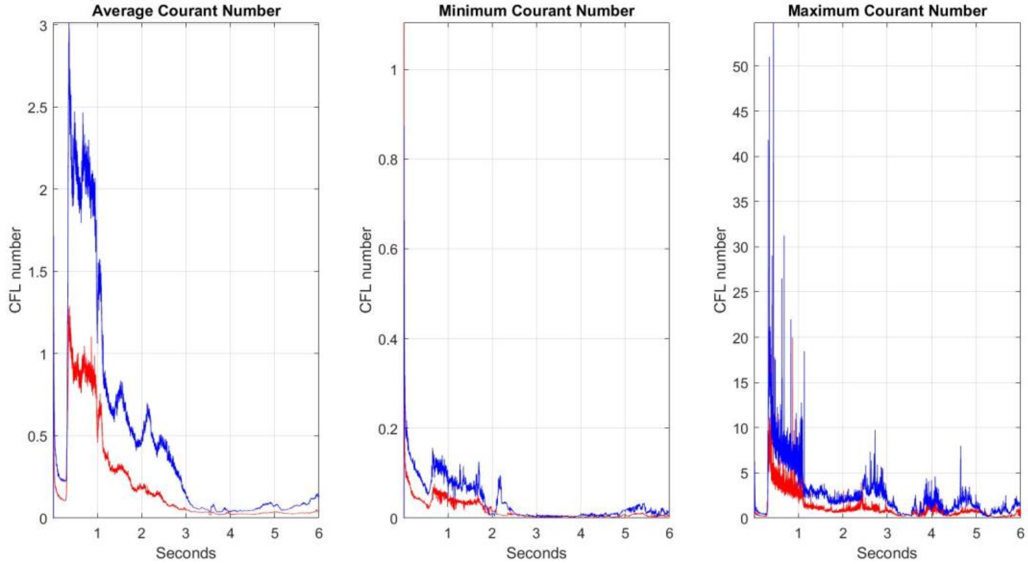

Figure 5.6: CFL values for free surface interaction, where blue is for Δt=1.2ms and red is for Δt=0.6ms

As described in section 3.3.4 the CFL number gives an indication of the ratio between the simulated fluid distance for a given time step, Δt, and the length of one cell, Δx. The values in the plots above are measured in the aft part of the body where the air cavity is located. The CFL plots for the two given time steps, seem to have the same trend, where the simulation with the lowest time step corresponds with lower CFL, which is reasonable.

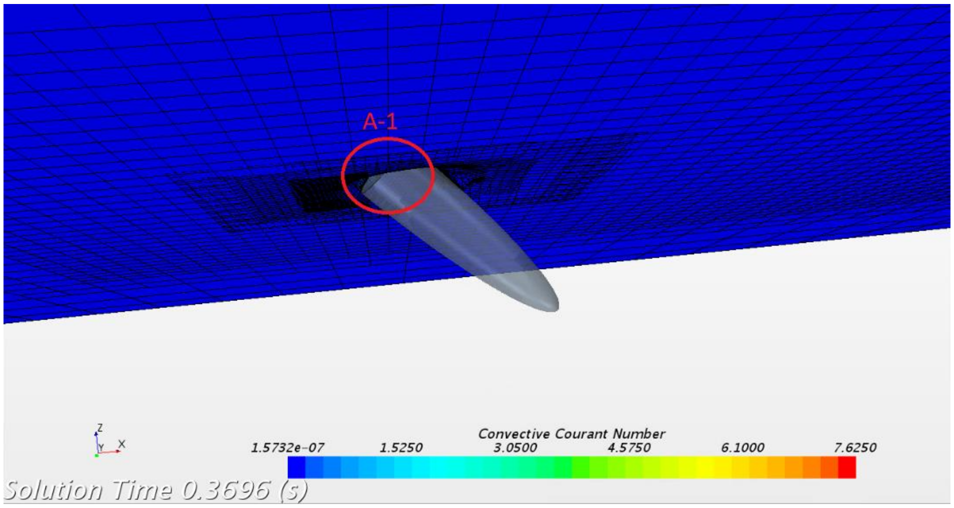

Figure 5.7: Courant scene for a global view at the end of water entry phase

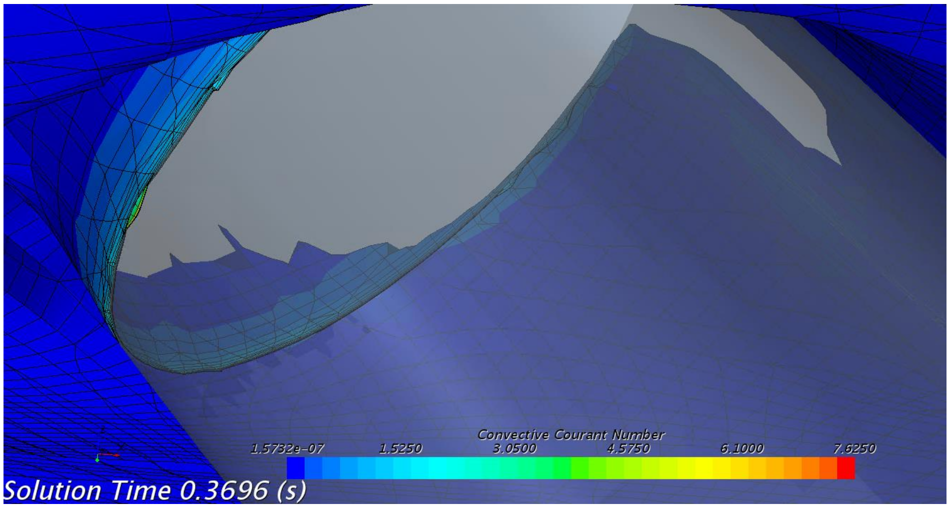

Figure 5.8: Local Courant scene from cut A-1 in Figure 5.7

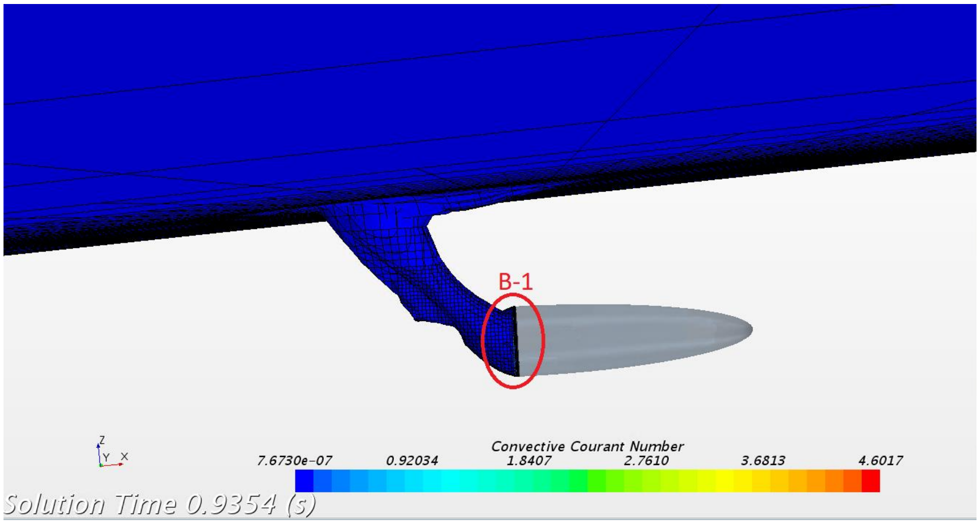

Figure 5.9: Global Courant scene right before cavity closure

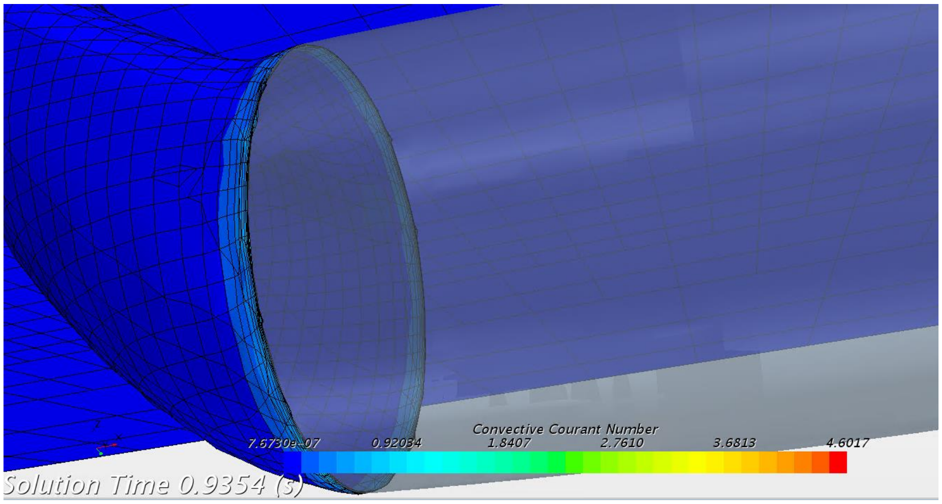

Figure 5.10: Local Courant scene right before cavity closure, cut B-1 from Figure 5.9

Both Figure 5.8 and Figure 5.10 shows the local CFL number, which indicates that the value has its maximum in the sharp corner on the aft part. This corresponds well with increased fluid acceleration around corners, and smallest cell size closest to the lifeboat surface (prism layer).

5.2 Convergence Study

In pursuance to investigate the convergence of the solution, the cell sizes in the grid has been changed. All the cells within the coarsest grid has been halved ones for the medium grid and twice for the finest grid. In order to have a more reliable convergence study, this is also done for the timestep. Then the CFL-number will be quite similar, though cell sizes is different. Meaning that the main parameter influencing the solution will be the cell size. An overview of the meshes is given in Table 5.1, and for the prism layers in Table 5.2. The parameters that will be investigated in this convergence study is acceleration, motion and pressure on the aft part of the lifeboat. The plots are integrated for global convergence and local points are selected for interesting points of time.

SMALLEST CELL SIZE $[m]$	**DISCRETIZATION**	**# CELLS LOCATED IN THE DOMAIN**	**# CELLS LOCATED IN THE OVERSET**	**TIMESTEP $[s]$**
0,16	Δx_3	88 186	203 043	0.0006
0,08	Δx_2	585 083	1 003 599	0.0003
0,04	Δx_1	4 409 925	6 839 080	0.00015

Table 5.1: Mesh description, where the cell sizes from the prism layer is excluded as smallest cell

	Δx_3	Δx_2	Δx_1
# OF PRISM LAYERS	12	10	16
TOTAL PRISM LAYERS HEIGHT [M]	0.31858	0.1527	0.16023
STRETCH FACTOR	1.4983	1.516	1.2419
CELL HEIGHT CLOSEST TO THE BODY [M]	0.00125	0.00125	0.00125

Table 5.2: Prism layer specification for each mesh discretization

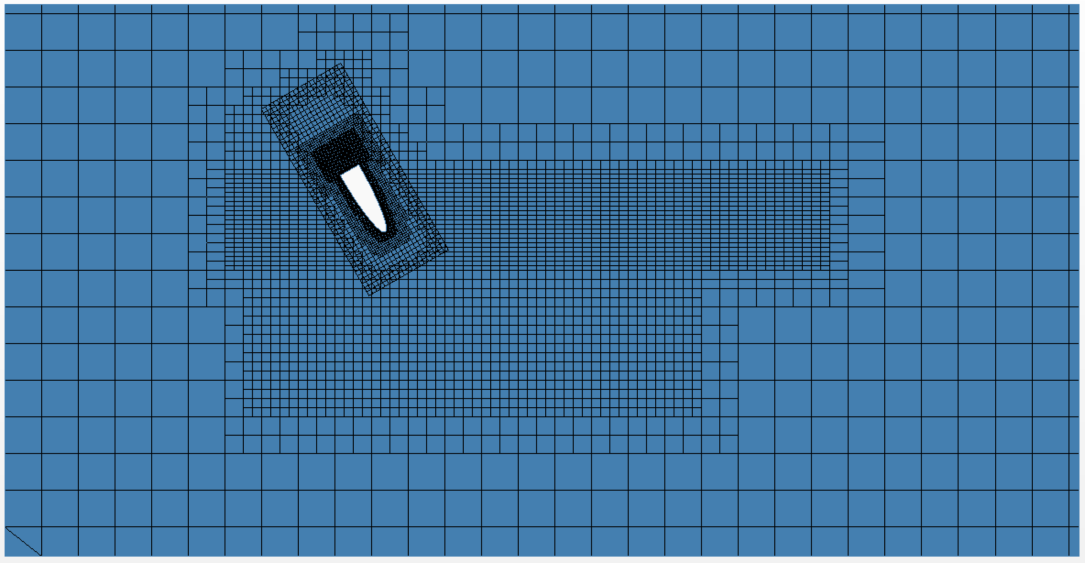

Figure 5.11: Mesh with 0,16 m as smallest cell, discretization Δx_3

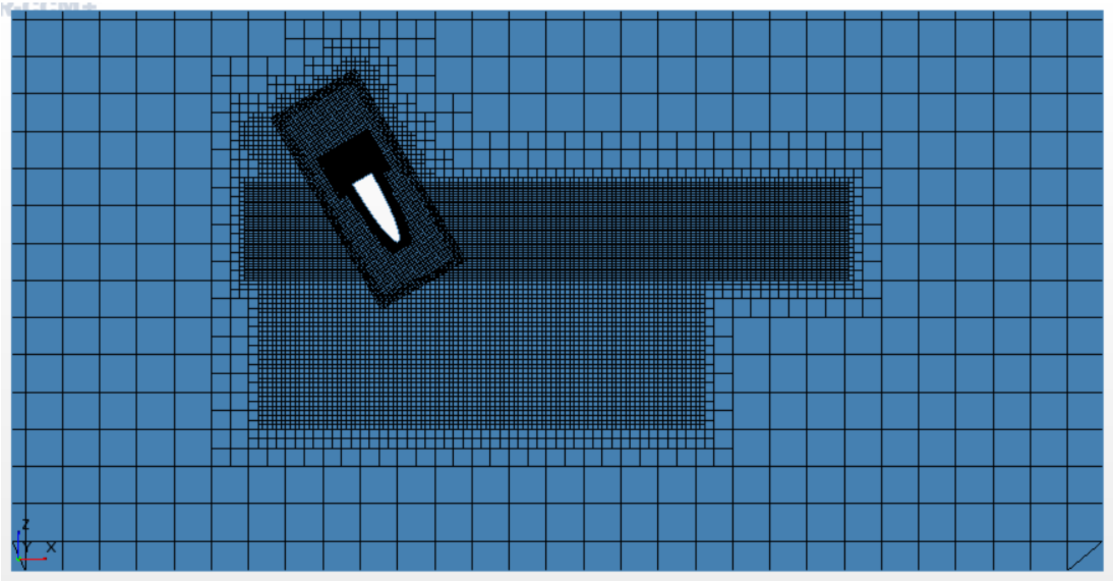

Figure 5.12: Mesh with 0,08 m as smallest cell, discretization Δx_2

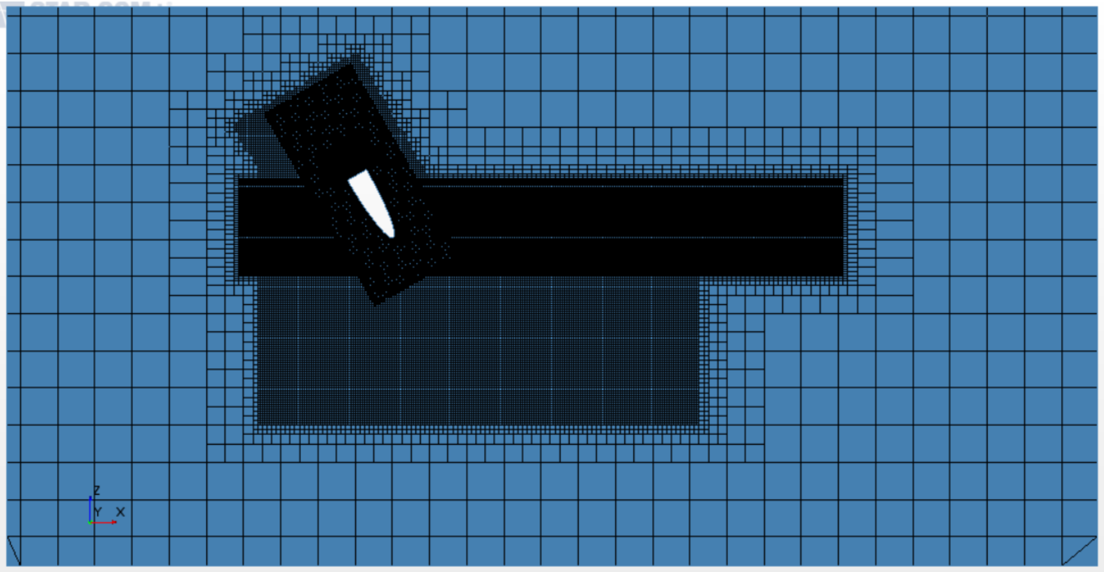

Figure 5.13: Mesh with 0,04 m as smallest cell, discretization Δx_1

As seen in Figure 5.11 - Figure 5.13 it is not only the cells located around the body that goes down in size, the water surface and overlap regions are also reduced in size in the same manner as the cells around the body. This is because of the overset mesh interaction with the domain, and it is recommended by the user guide that the overset cells are of similar size as the overlap cells. (Steve CD adapco, 2016)

A convergence study has been carried out, inspired by the paper written by Colicchio, et al. (2006). Assuming that the error approximated for a given quantity, q is proportional to Δx^{OA}. OA is the order of accuracy and has been defined as:

$$OA := \frac{\log\left(\frac{\left|I_g(\Delta x_2) - I_g(\Delta x = 0)\right|}{\left|I_g(\Delta x_1) - I_g(\Delta x = 0)\right|}\right)}{\log\left(\frac{\Delta x_2}{\Delta x_1}\right)} \tag*{[36]}$$

$I_q(\Delta x_1)$ and $I_q(\Delta x_2)$ are integrated values of given quantity, q, predicted numerically for discretization Δx_1 and Δx_2, representing different mesh resolutions. $I_q(\Delta x = 0)$ represent the exact time integral of the quantity q. Positive values are desired, where larger values mean that the results converge faster to a specific value. Since there has not been conducted experiments for similar lifeboat geometry and very small cell sizes causes too large CPU time, the exact integrated value for given quantities, $I_q(\Delta x = 0)$ is unknown. Hence, equation [36] has to be modified, where the exact solution can be derived by assuming a linear logarithmic relationship between I_q and Δx, by extrapolation from the integrals on three different meshes, $I_q(\Delta x_1), I_q(\Delta x_2)$ and $I_q(\Delta x_3)$. (Colicchio, et al., 2006)

$$-\frac{\log\left(\frac{|I_q(\Delta x_2)-I_q(\Delta x=0)|}{|I_q(\Delta x_1)-I_q(\Delta x=0)|}\right)}{\log\left(\frac{\Delta x_2}{\Delta x_1}\right)} = -\frac{\log\left(\frac{|I_q(\Delta x_3)-I_q(\Delta x=0)|}{|I_q(\Delta x_2)-I_q(\Delta x=0)|}\right)}{\log\left(\frac{\Delta x_3}{\Delta x_2}\right)} \quad [37]$$

The numerical solver uses a 2. order convection scheme. Hence, in order to have a satisfactory convergence, the order of accuracy should have a value close to 2.

Since the order of accuracy mostly is determined by integrated quantities, it is important to consider which time interval that is of interest and provide accurate predictions. Time intervals where the various plots intersect, will alter the accuracy since the integrated values may be of similar measure, even though the shape is not. Therefore, the first time interval (yellow area) is chosen from 0.22 s - 0.75 seconds, the second time interval is for the cavity closure peak (blue area) chosen from 0.985 s – 1.0125 s and the third time interval (purple area) chosen from 1.4 s – 2.4 s, shown in Figure 5.14

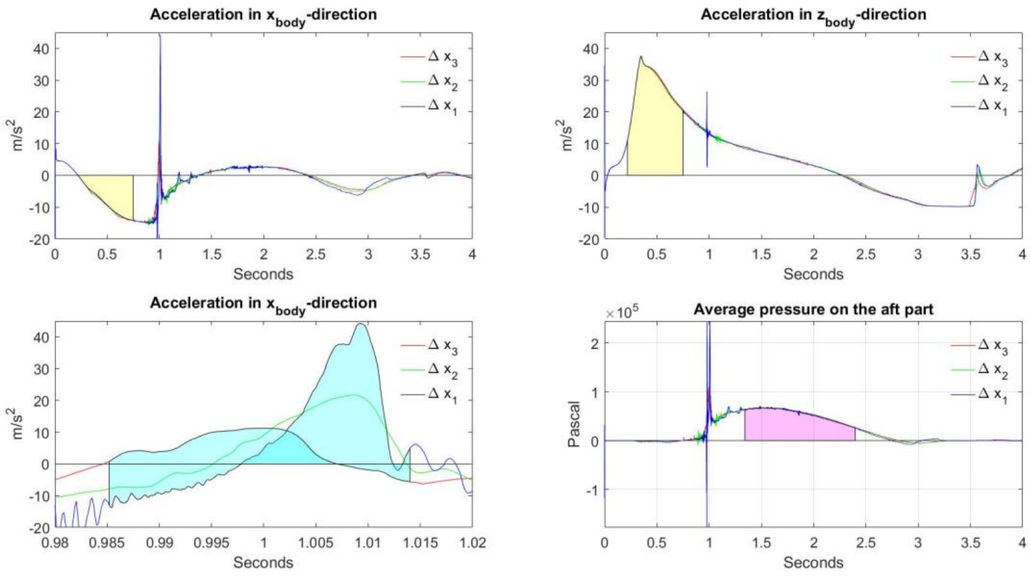

Figure 5.14: Convergence plots, where yellow is the time instance of 0.22 s – 0.75 s, blue 0.985 s – 1.0125 s and purple 1.4 s – 2.4 s

DESCRIPTION OF VALUES	**TIME INTERVAL/SINGLE POINT**	**ORDER OF ACCURACY (OA)**
INTEGRATED VALUE OF ACCELERATION IN x_{body}	0.22 s - 0.75 s (water entry phase)	0.545
INTEGRATED VALUE OF ACCELERATION IN z_{body}	0.22 s - 0.75 s (water entry phase)	0.958
INTEGRATED VALUE OF ACCELERATION IN x_{body}	0.985 s - 1.0125 s (air cavity closure peak)	1.190
INTEGRATED VALUE OF AVERAGE PRESSURE IN AFT PART	1.4 s – 2.4 s (Submerged phase, post air cavity closure)	0.546
CAVITY CLOSURE TIME	Single point	3.807
MAXIMUM SUBMERGENCE, z_{global}	Single point	1.384

Table 5.3: Order of accuracy for different integrals and points for selected time intervals and point of time.

All the measures of the order of accuracy are positive, indicating that the two finer grid discretization are more similar then the coarsest for the given quantities. Even though the plots shown in Figure 5.14 are very similar, they do not seem to converge with the order of accuracy that is expected for the solver. As mentioned above, intersection for the varies plot, will alter the reliability of the integrated quantities. This theory gets strengthen, since the OA is significantly higher for single point values, though the cavity closure time indicates a convergence rate, faster than the solvers accuracy. Another error source influencing the order of accuracy, might be the turbulence and corresponding Y^+ model applied. A hybrid model of the Y^+ model was chosen because of the density differences, as mentioned in section 3.3.3, Wall Y^+. The code used for modelling of various Y^+ ranges for the hybrid model are not shown in the manual, hence an inaccurate solver method is not unlikely. As for the turbulence, the solver struggled to model the turbulence when the aft part intersected with the free surface even though a relatively low time steps were applied. This will surely alter the order of accuracy, even though it is of secondary importance for short duration of impact problems with flow separation from sharp corners. (Faltinsen & Greco, 2013) The low values in OA can also be caused by the inaccuracy of the coarsest mesh. If the mesh is to coarse, it can lead to large unreal manifestations in the solution. A finer mesh may result in a more satisfactory OA. For the peak interval in Figure 5.14 for the body fixed x-accelerations, it is easy to see that there is no local convergence due to the large difference in shape of the plot, even though the

OA is quite high. However, the trend seems to converge, as the closure time is almost the same for the two finest grids and the maximum submergence point only have a difference of 4 cm between the finest grid and the coarsest grid, which implies global convergence.

DISCRETIZATION	SOLVING TIME $[hours]$	# OF PROCESSORS	CPU COST
$\boldsymbol{\Delta x_3}$	25	9	225
$\boldsymbol{\Delta x_2}$	51	39	1989
$\boldsymbol{\Delta x_1}$	150	272	40800

Table 5.4: Mesh discretization with its specific solving time, number of processors used and computational cost

The solution does not seem to have local convergence. However, the quite similar position plots show that the local accelerations do not have large manifestations in the global behaviour of the body. It is assumed that the finest mesh gives the most accurate results, but it is not computational economic. The second finest mesh has a global solution very close to the finest one. Hence, a compromise between computational time and accuracy is made, and Δx_2 is the chosen mesh discretisation for further studies in this thesis.

6 Results with initial conditions

As concluded with in 5.2, the results presented is obtained with the Δx_2 mesh discretization. This is due to the low CPU cost for each simulation, as well as section 5.2 concludes with that this discretization gives accurate results for most of the phases. This will also give a better representation of the comparison of a change in different parameters in section 7, where this discretization has been used. The results are obtained with an initial condition seen in Table 6.1.

CONDITION	VALUE	DIMENSIONS
WATER ENTRY ANGLE	60	degrees
VELOCITY$_{\text{BODY FIXED}}$	[20, 0, -5]	m/s
ANGULAR ROTATION	15	degrees/s

Table 6.1: Initial conditions

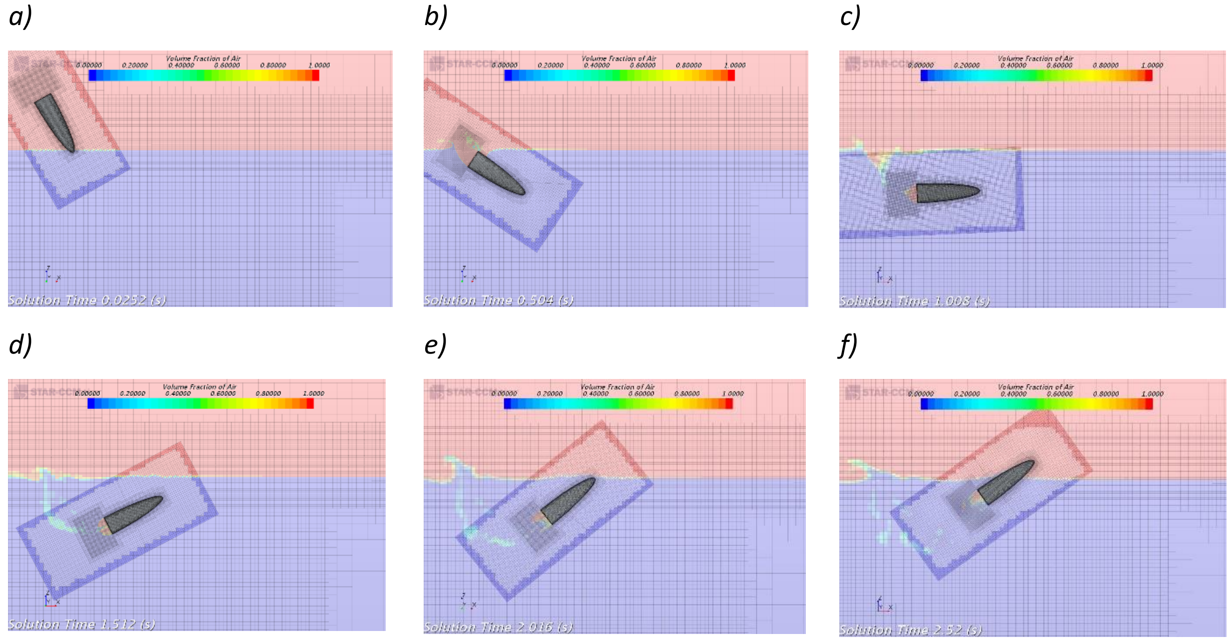

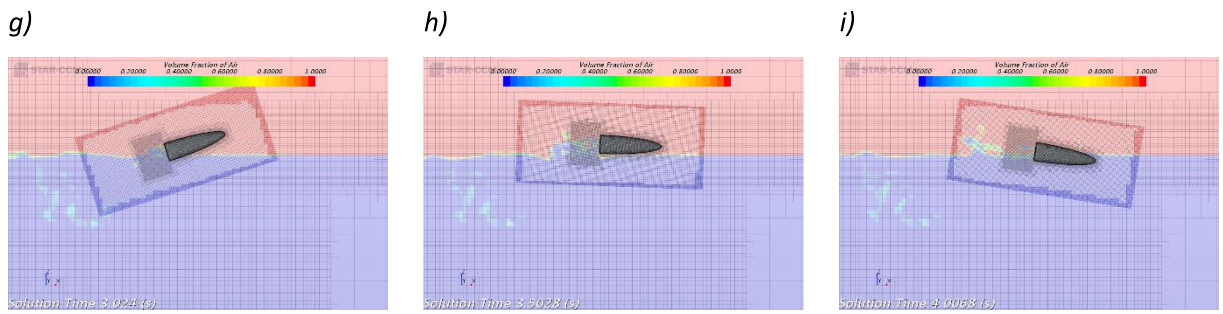

Figure 6.1: Volume fraction of air representation of the path from water entry to sail away

From Figure 6.1 it is possible to see the global behaviour of the path of the lifeboat with its initial conditions.

6.1 Acceleration and angular acceleration

The acceleration results are divided into the different phases the lifeboat goes through, from water entry to sail away phase. The air cavity formation and collapse are also included here.

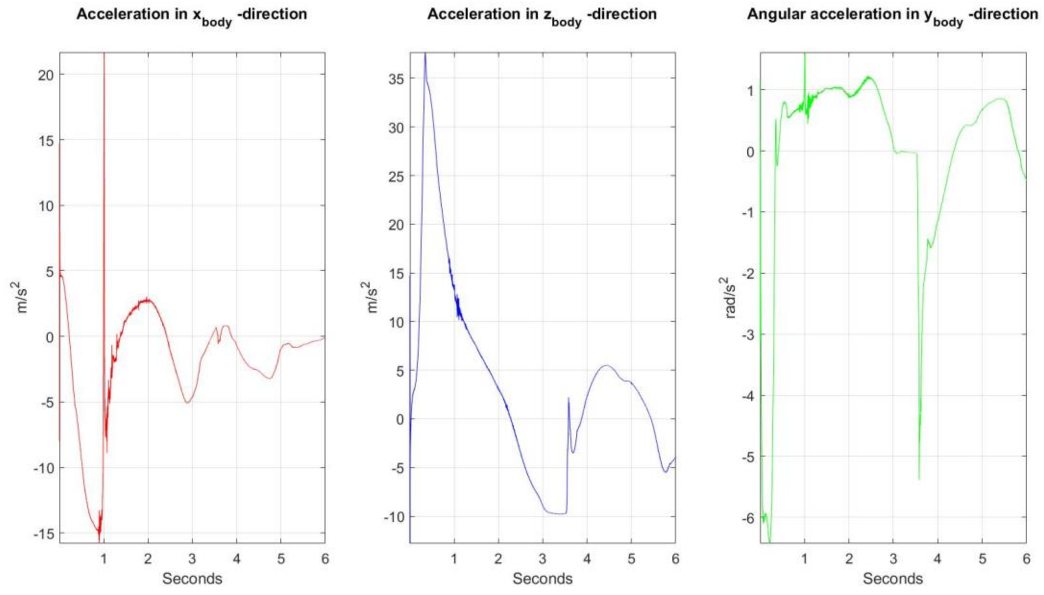

Figure 6.2: Acceleration and angular acceleration measured in the body fixed coordinate system

6.1.1 Water entry

The body has an initial free-falling acceleration, with a constant clockwise rotational velocity, until the water entry starts after 0.0085 s. As the lifeboat bow enters the water it is subjected to slamming forces. As mentioned in section 4.4, the segregated flow solver does not give a good representation of this phenomenon. From the acceleration plot (Figure 6.2), it is possible to see that the initial acceleration is counteracted in both x_{body} and z_{body}. The body will also get counter clockwise angular acceleration, the rotation is decreased and eventually reversed in the water entry. This occurs as the centre of gravity gets pulled down, while the bow is partially constrained in the fluid. When the added mass increases, there is a small clockwise angular acceleration which is slowly increasing for a while.

6.1.2 Air cavity formations

In the acceleration plot from Figure 6.2, the air cavity closure appears as a the large peak in x_{body} acceleration. It is caused by the pressure from the water on the newly formed air bubble located on the aft part of the body. The air in the bubble is modelled as incompressible. A consequence regarding this, is that the entrapped air bubble is rigid, hence the appearance of a single peak with a high value. The air in the entrapped bubble is in fact compressible, the acceleration plot is therefore not realistic at the point of air cavity closure. It is expected that the entrapped air bubble will oscillate in size, and that the first peak will be less pronounced than the peak in Figure 6.2.

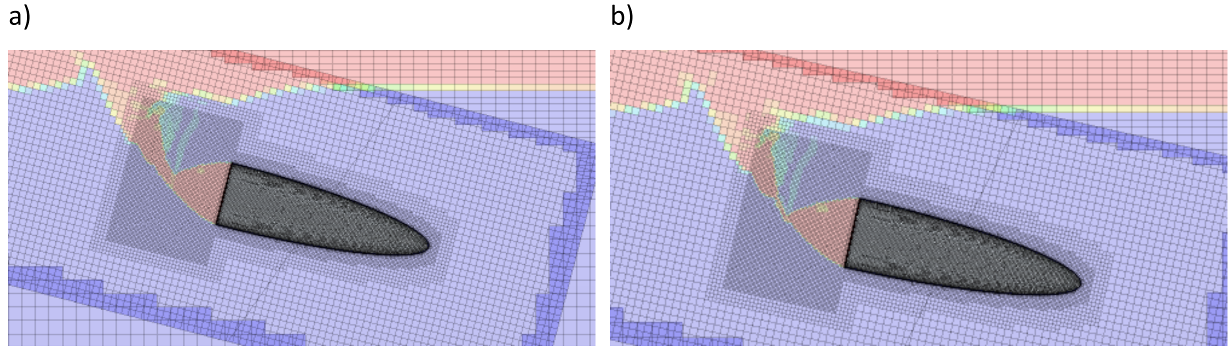

c)

d)

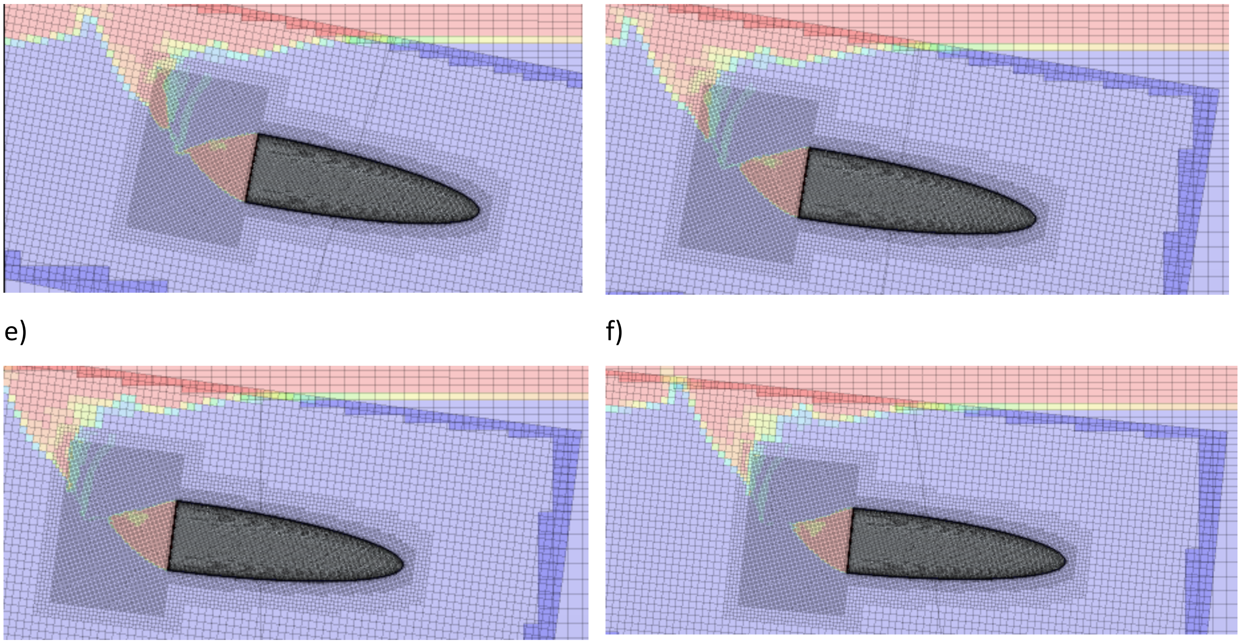

e)

f)

Figure 6.3: Beginning of the air cavity closure, 2-D, starting from solution time 0.756s with $\Delta t = 0.025s$, until 0.882s

a)

b)

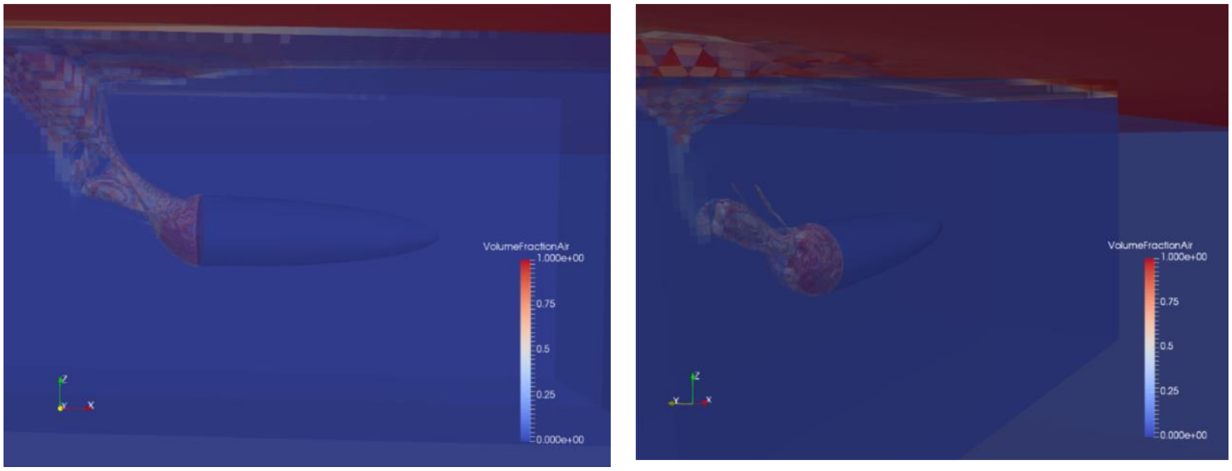

Figure 6.4: Visualization of the air cavity closure in 3D where a) shows the solution time 1.002 s and b) shows solution time 1.102 s

Figure 6.3 shows the air cavity and the beginning of the closure in the period between Figure 6.1 b) and c). As the pictures are in 2D, it is difficult to see the exact moment of air cavity closure later in the time-series. A 3D representation of the air cavity closure is shown in Figure 6.4.

6.1.3 Submerged phase after air cavity formation

The body will continue to rotate, and eventually the x_{body}-direction will be parallel to the water surface. At this position, the body is close to maximum submergence. The body still has a counter clockwise rotation, this can be seen in Figure 6.5. Shortly after maximum submergence, when the bow is turning upwards, the x_{body} motion and the buoyancy force will both have a positive contribution in the global z-direction. The point can be seen at 1.375 s in the x_{body} acceleration in Figure 6.2, where the body gets a positive acceleration contribution. There is a positive x_{body} acceleration contribution until the point where the gravitational forces excide the buoyancy forces at the water exit.

6.1.4 Water exit

As the body exits the water, the buoyancy acts upwards on the aft part, while the gravitational force acts downwards on the fore part. This creates a large increase in clockwise rotation, while the body gets deaccelerated in the negative vertical direction by the gravitational force. The small positive x_{body} acceleration from the gravitational force before re-entering the water, is due to the x_{body}-motion changes in the vertical global direction. As the body has a certain pop-up height, it is subjected to a second slamming at the re-entering of the surface. It is apparent as the peak at 3.6 s in z_{body} acceleration, Figure 6.2.

6.1.5 Sail away phase

After water exit and the second water entry, the body will have a negative acceleration in the body fixed x-axis as it is slowed down by resistance forces, and the only thing driving it forward is the initial water exit velocity.

6.2 Velocity

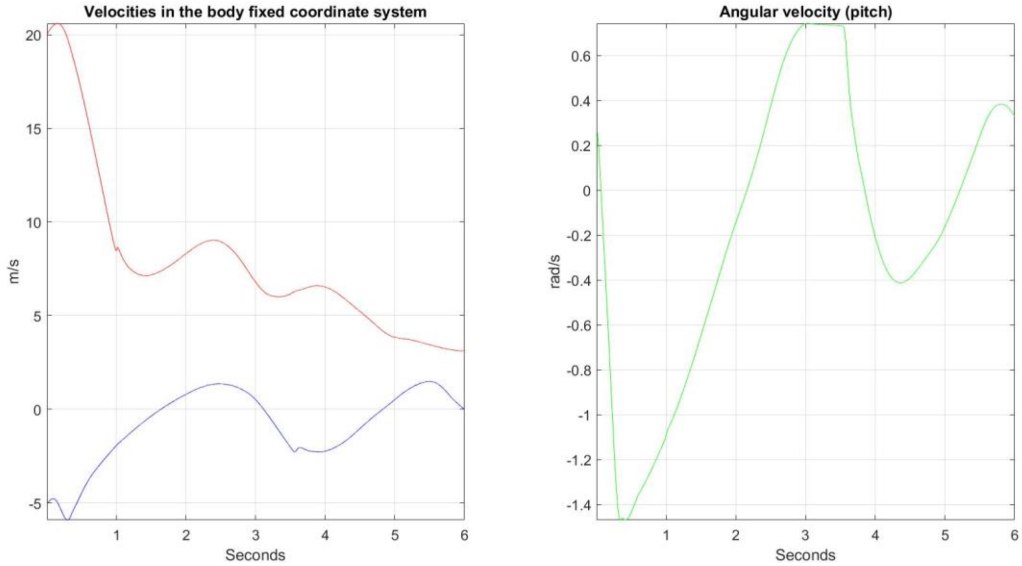

Figure 6.5: Velocity plot where the red is in the x_{body} *-direction and blue in* z_{body} *-direction*

The body fixed velocity in x-direction reaches its maximum value after approximately 0.25 seconds. After initial impact the velocity is rapidly decreasing. The body is resurfacing at 2.45 s, this is noticeable in the velocity plot as the body fixed velocities in both x and z has a local maximum for this point. The velocity plot is smother than the acceleration plot, which is logical as the acceleration is the time derivative of the velocity. The large acceleration peaks for the point of air cavity closure and second water entry are shown to have little effect on the velocity, they are noticeable as small discontinuities in the plot at 1.0 s in x_{body} and at 3.5 s in z_{body}, respectively. At 6 s, the body has a positive velocity in x-direction. This is beneficial as the sail away distance will increase as the time passes.

6.3 Motion

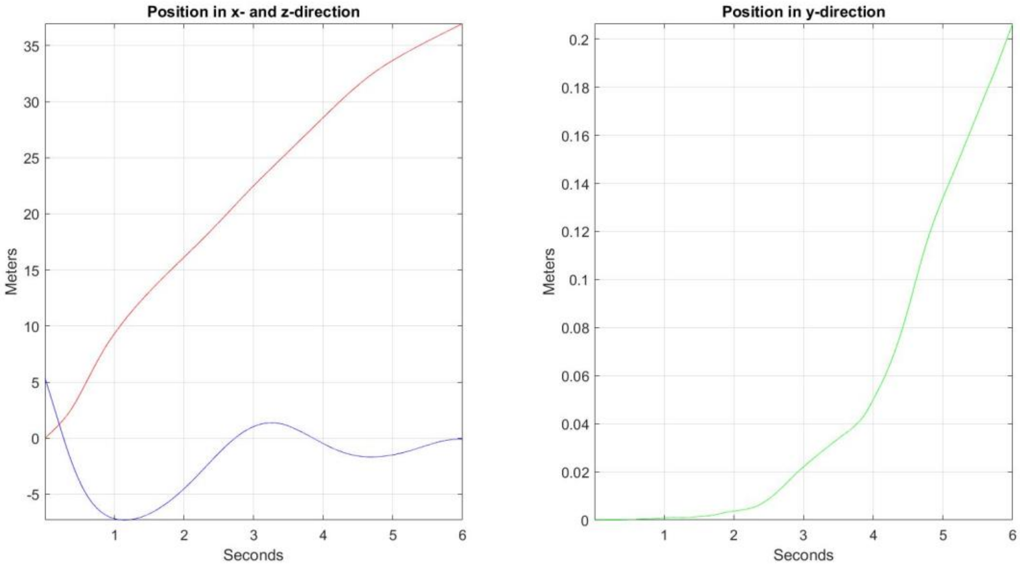

Figure 6.6: Position plot, where the red line is in the x-direction, blue in the z-direction and the green in y-direction

The position is the time integrated velocity. Figure 6.6 shows a continuous line which imply that the impulse forces inflicted at air cavity closure and at the second water entry are not large enough to make sudden changes in the position. The lifeboat reaches maximum submergence after approximately 1.2 seconds with a depth of 7 meters. After 6 seconds, the lifeboat has managed to sail 36 meters away from the point of initial water entry. As seen in Figure 6.5, the velocity is still positive at 6 s, which leads to an increase in sailing distance later on. By comparing the lifeboat motion in Figure 6.6 with Figure 2.8, the lifeboat trajectory shows resemblance with motion pattern 1, where the lifeboat pitches significantly at maximum submergence and ascent so that is surfaces with a positive forward velocity, as seen in Figure 6.1. According to DNV-GL, this is the preferred trajectory. (DNV-GL, 2016)

6.4 Pressure aft

The pressure on the aft part is mostly affected when the body is in the submerged phase, hence this is the period that will be discussed. To be sure of structural integrity in the aft part, e.g. for a weak part like a door, filtering of the pressure peaks is not an option since these large oscillations can results in local structural failure. Hence, the air cavity should ideally be modelled as compressible for such calculations to be utilized, as Tregde (2015) concludes with in his paper. (Tregde, 2015)

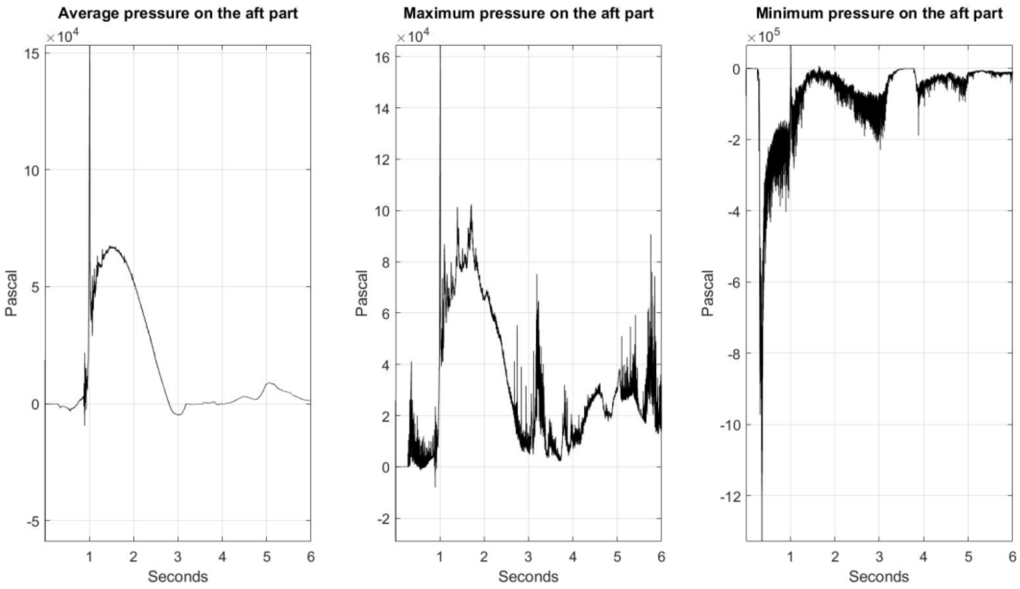

Figure 6.7: Pressure plots on the aft part

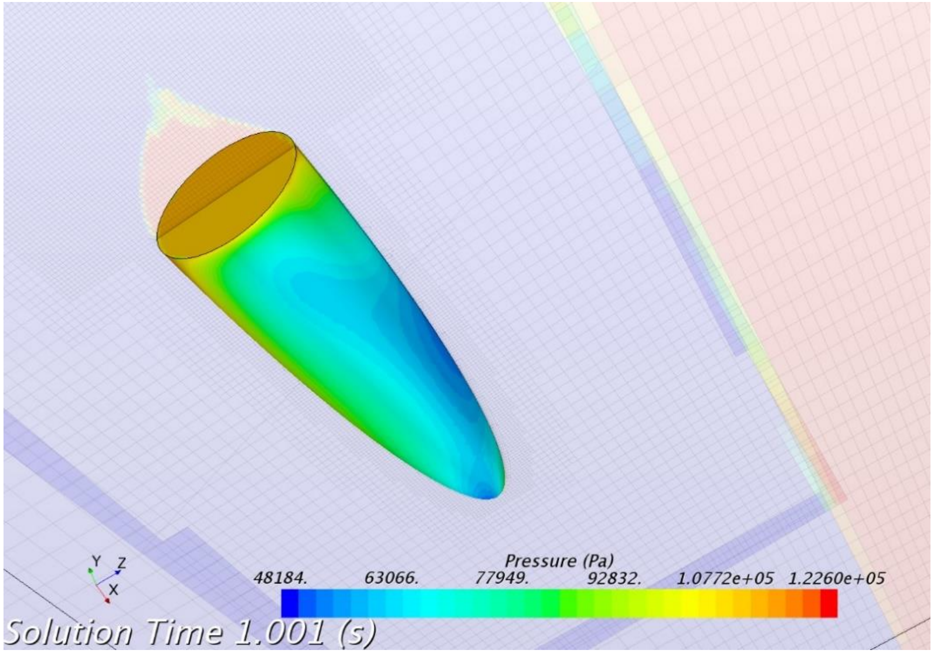

Figure 6.8: Pressure distribution on the lifeboat 7ms before the peak

The pressure is proportional to the acceleration, which means that the peaks should appear at the same distinctive time. By comparing Figure 6.2 and Figure 6.7 is it possible to see the resemblance of this. The air cavity closure is seen as the large peak in Figure 6.7 for average, maximum pressure and also a smaller positive peak for the minimum pressure. Figure 6.8 shows that the high pressures is in the area where the air cavity is located and the lower pressures seen in the minimum pressure plot, Figure 6.7, is in the area where the air cavity ends and water attaches to the body. Throughout the submerged phase, the average pressure and maximum pressure in Figure 6.7 follows the same tendency. As seen in Figure 6.8 the pressure is close to uniformly distributed on the aft part during this phase. The pressure increases until the air bubble is at maximum submersion, due to the hydrostatic pressure. After this the pressure is decreasing until the aft part is above the calm water level.

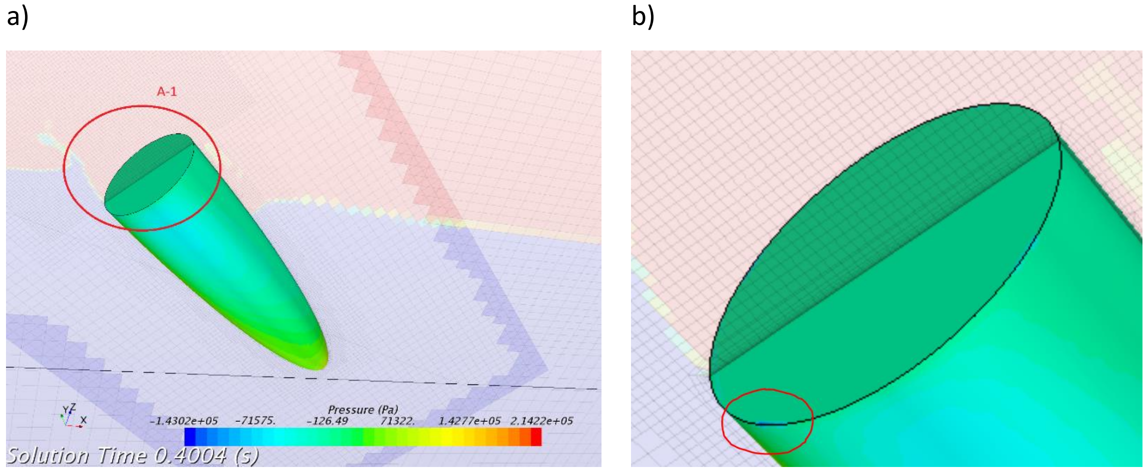

Figure 6.9: Minimum pressures from the splash crown, where a) shows the global and b) more locally of the same time instance

As seen in Figure 6.7 the minimum pressure has large negative values at approximately 0.4 s – 0.6 s, this indicates that the water entry splash crown and the air cavity formation creates a suction on the aft part. This is illustrated in Figure 6.9.

6.5 Comparison with theory

6.5.1 Air cavity investigation

As mentioned in 0, high Capillary number is beneficial to ensure air cavity formation. An air cavity was therefore expected, due to the relatively large viscous forces compared to the surface tension in water and the sharp corners in the aft part. In addition, surface tension has been neglected for the simulations due to its insignificance in the case of lifeboat diving, as mentioned in 0. For Bond number higher then 10^3, only deep and surface seal occurs, where the transition from deep seal to surface seal occurs for $Fr > \sqrt{150}$. This corresponds to a velocity greater than 60 m/s for the body in this thesis. Hence, deep seal is expected, corresponding well to Figure 6.3. f).

In section 0, the derivation between Froude number and closure time is obtained in equation [14]. From studying the VOF-picture at approximatly1 s, a deep seal is apparent. The air cavity height is clearly less than one half of the distance travelled from the entry point in the water surface to the aft part of the body. By studying the VOF-pictures, the aft part of the body gets submerged after 0.4284 s, and the air cavity initiation starts after approximately 0.6 s. The air cavity seems to be largest in diameter for this time instant, meaning that the expansion time is short compared to the collapse time, since the collapse seems to happen at approximately 1.0 s. This results in a closure time $T_c = t_0 + \delta t_2 = 0.17\ s + 0.4\ s = 0.57\ s$. Then by solving equation [14] with a characteristic diameter of 3 m, and a velocity of 20 m/s, the theoretical closing time is calculated to be

$$T_c = \frac{3m}{20m/s}\left(\frac{3}{2^{5/3}}\right)\left(\frac{20m/s}{\sqrt{9{,}81m/s^2 * 3m}}\right)^{2/3} = 0{,}34\ s$$

The body investigated in this thesis has a long cylindrical shape, but the dimensions, centre of gravity and density is somewhat different than the body investigated in the paper from (Yan, et al., 2009). An important assumption was that the cavity closure height, H_c was approximately $\frac{1}{3}$ of the cavity height H. For this case, the dimensions of H and H_c is difficult to measure, as the VOF pictures are in 2D. The main difference is that there is an oblique impact and a pitch velocity, the simplified lifeboat geometry has a low density and it is not axisymmetric as the centre of gravity is moved in z-direction. For this derivation, the vertical velocity is also assumed constant, though the decrease is significant. These differences prevent a good comparison.

6.5.2 Water exit

From theory (see section 2.5) the relationship between the pop-up height and the water exit velocity in the global vertical direction can be tested utilizing equation [16]. When the centre of gravity passes the water surface, the global vertical velocity is:

$$w_{global} = \frac{8.6m}{s} * \sin(27°) + \frac{1.25\ m}{s} * \cos(27°) = 5.02\ m/s$$

For the simplified case, then the pop-up height should approximately be

$$H_{pop-up} = \frac{v_{vert}^2}{2g} = 1.28\ m$$

From the motion plot, the pop up height is read to be 1.23 m, corresponding well with the assumption that energy is lost due to splash plume and wave making. (Truscott, et al., 2016)

6.6 Courant validation

An indication of the expected CFL were investigated for the coarsest grid discretization, mentioned in section 5.1. Therefore, a new validation is needed, though the time step used is two times smaller.

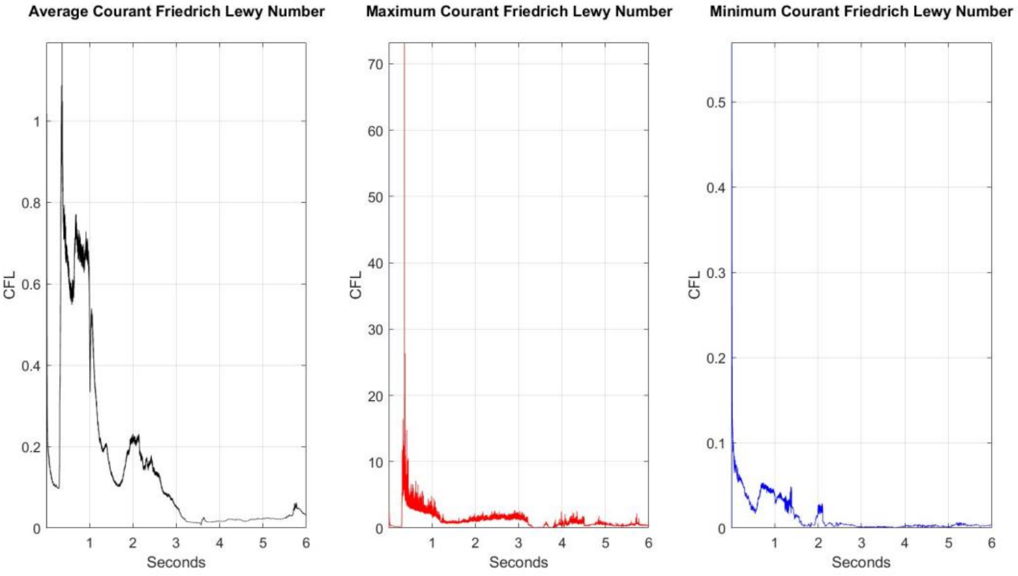

Figure 6.10: CFL number throughout the simulation

The average CFL number measured in the cells located around the aft part of the body bear resembles to the average CFL values for the coarsest mesh discretization, Δx_3, which is reasonable considering the solver approach for solving this value. There is still a distinctive peak at approximately 0.4 seconds, where problems related to solving the turbulence model occurred.

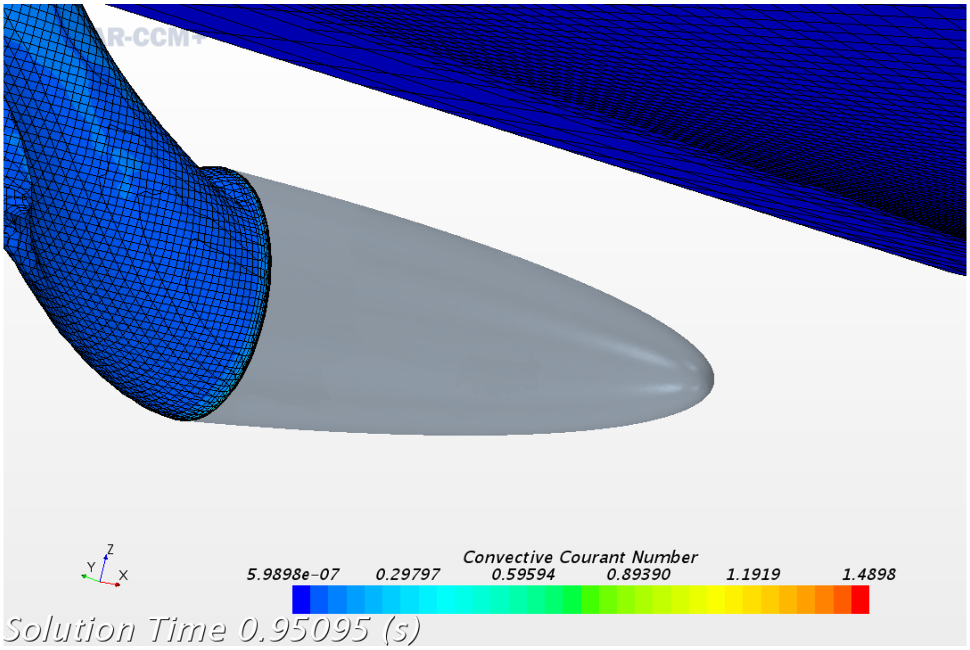

Figure 6.11: CFL visualization

The highest CFL values are still located around the sharp corners on the aft part of the body, but smaller in magnitude compared to the coarsest grid. This is probably a result of relatively similar prism layer distribution in terms of height for the varies mesh discretization’s, though the time step is halved.

7 Parameter investigation

Since a lifeboat is a last resort solution of escaping the mother vessel, the weather conditions will not likely be ideal. The launching and free-falling phase can therefore be affected, which results in difference in the behaviour in the four later phases, as described in section 2. The water entry angle and the velocity are two parameters that can be affected by wind loads and by which wave phase it is entering. Also, the centre of gravity can change, as it depends on the number of passengers and their seating arrangement. Hence, an investigation of the effect these changes can have, has been carried out. The chosen values are shown in Table 7.1. Only one parameter will be changed for each simulation, in order to examining the influence of the different parameters. However, if the free-falling time and distance increases, both velocity and water entry angle is likely to increase.

PARAMETER		**-**	**IC**	**+**	**Δ**
θ	[°]	55	60	65	5
COG_Z	[m]	-0.7	-0.5	-0.3	0.2
V	[m/s]	15.62	20.62	25.62	5

Table 7.1: Parameter investigation values

From these parameters, accelerations, velocities, air cavity formation, path and pressure has been studied to get an insight of how they are changing with the varying parameters.

7.1 Velocity

Three different velocities have been tested to investigate the effect they will have for the behaviour of the body. Their maximum values are 15.62 m/s, 20.62 m/s and 25.62 m/s. The ratio between the velocities in x_{body} and z_{body} is held constant.

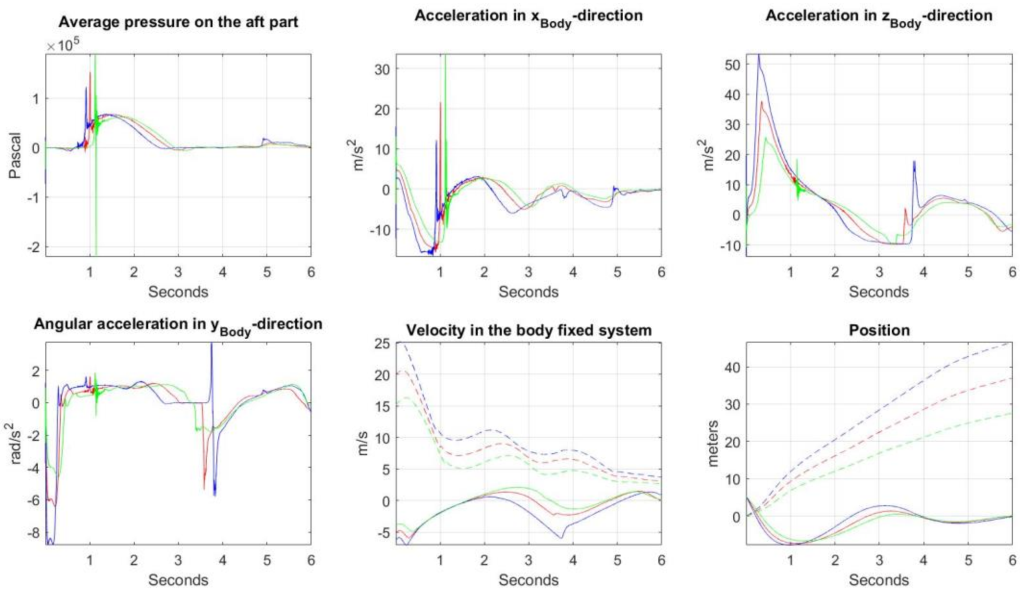

Figure 7.1: Green is 15.62 m/s, red is IC with maximum velocity 20.62 m/s and blue is 25.62 m/s. The accelerations and velocities are taken in the body fixed coordinate system. The dashed lines are in the x-direction, and the solid lines are in the z-direction in the velocity and position plots.

DISTINKTIVE PARAMETER	**15.62 m/s**	**INITIAL CONDITION 20.62 m/s**	**25.62 m/s**
CAVITY CLOSURE TIME (PEAK) [s]	1.121	1.009	0.915
WATER EXIT TIME [s]	3.073	2.730	2.366
POP-UP HEIGHT [m]	0.557	1.369	2.835
MAXIMUM SUBMERSION [m]	-6.633	-7.297	-7.700
SAILING DISTANCE AT 6 s [m]	27.635	36.969	46.619
VELOCITY x_{Body} AT 6 s [m/s]	2.709	3.109	3.685
ACCELERATION PEAK MAGNITUDE [m/s^2]	33.720	21.678	12.189
MAX PRESSURE AFTER CAVITY CLOSURE [kN/m^2]	62.390	67.460	68.420

Table 7.2: Distinctive values for comparison the change in water entry velocity

The plots in Figure 7.1 reveal great differences. The accelerations in x_{body} and z_{body} is clearly largest for the high impact velocity case. It also has the most negative angular acceleration at the water impact phase, hence it will contribute the most to the counter clockwise rotation. The air cavity closure occurs earlier for the case with the highest velocity, this compares well with equation [14] The global horizontal velocity at the point of maximum submergence has a significantly larger value for the case with the highest initial velocity, then for the two other cases. This, combined with a higher counter clockwise rotation, leads to high water exit velocity and angle. The result is an early water exit and a large pop-up height. As it "shoots" out of the water with high energy, it will get the longest sailing distance at 6 s. And since it also has the highest velocity at this point of time, it will have the best potential for sailing further away from the evacuation scene. The maximum submergence is also quite different, which is an important parameter since it is proportional to the hydrostatic pressure, when assuming constant density. High hydrostatic pressure is of concern for asymmetric geometry like appendages, as a result of the varying pressure loads. This can further cause implosions.

7.2 Water entry angle

A preferable water entry angle is approximately 60°. However, the different external forces affecting the lifeboat can change this. Three different water entry angles have been tested to investigate the effect they will have for the behaviour of the body. Their values are $55°$, $60°$ and $65°$.

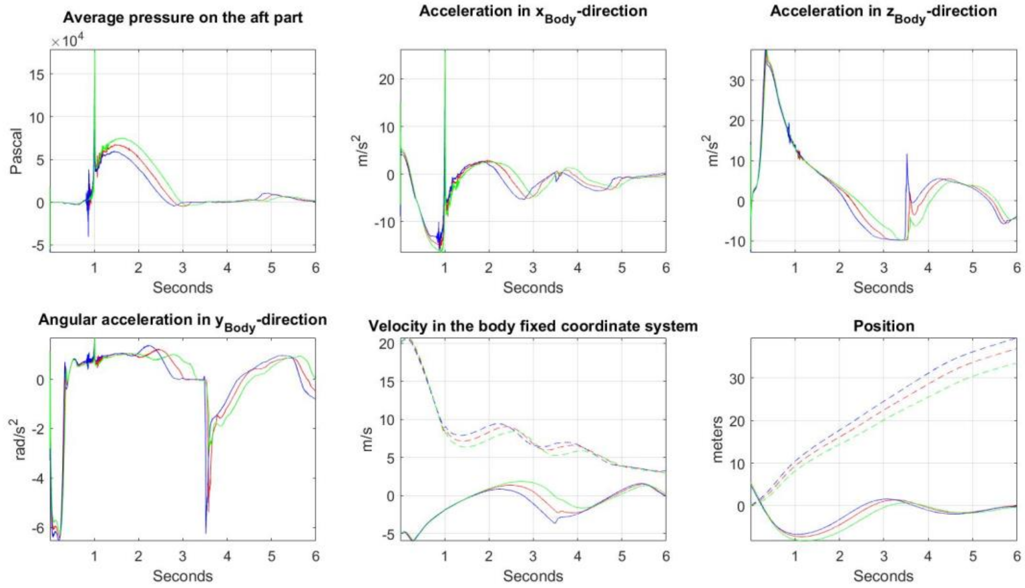

Figure 7.2: Plots of the results with different water entry angles, where blue is 55°, red is 60° and green is 65°. The accelerations and velocities are taken in the body fixed coordinate system. The dashed lines are in the x-direction, and the solid lines are in the z-direction for the velocity and position plots.

DISTINCTIVE PARAMETER	55 DEGREES	INITIAL CONDITION	65 DEGREES
CAVITY CLOSURE TIME (PEAK) $[s]$	1.004	1.009	1.012
WATER EXIT TIME $[s]$	2.515	2.730	3.104
POP-UP HEIGHT $[m]$	1.542	1.369	0.657
MAXIMUM SUBMERSION $[m]$	-6.723	-7.297	-8.290
SAILING DISTANCE AT 6 s $[m]$	39.482	36.969	33.608
VELOCITY x_{Body} AT 6 s $[m/s]$	3.237	3.109	2.941
ACCELERATION PEAK MAGNITUDE $[m/s^2]$	18.511	21.678	26.194
MAX PRESSURE AFTER CAVITY CLOSURE $[kN/m^2]$	60.040	67.460	75.290

Table 7.3: Distinctive values for comparison for a change in water entry angle

The motion plot in Figure 7.2 shows that maximum submergence increases with increasing water entry angle. This is logical since the velocity is constant in the x_{body}- and z_{body}-direction, hence the body gets an increased initial velocity contribution in the vertical direction, in combination with small differences in angular acceleration. The maximum submergence is an important parameter, as discussed above and highly influenced by the water entry angle. Thus, the water entry angle is a crucial parameter. The smallest water entry angle gives the shortest submerged time and the highest body fixed velocity in x-direction at water exit. The contribution to counter clockwise rotation in the submerge phase seems to be independent of the three tested water entry angles. Hence, the case with the lowest water entry angle gives the highest water exit angle. Thus, an increase in pop-up height with decreasing water entry angle. The high exit velocity also leads to the longest sailing distance in global x-direction. The velocity is positive after 6 s for all the cases. It is most positive for the smallest water entry angle, as the decreasing rate is approximately equal for the three cases after second impact. The maximum pressure occurs just after the point of maximum submergence, where the hydrostatical pressure is at maximum. The case with water entry angle of 65° have the deepest maximum submergence point, and will also experience the highest pressure on the aft part.

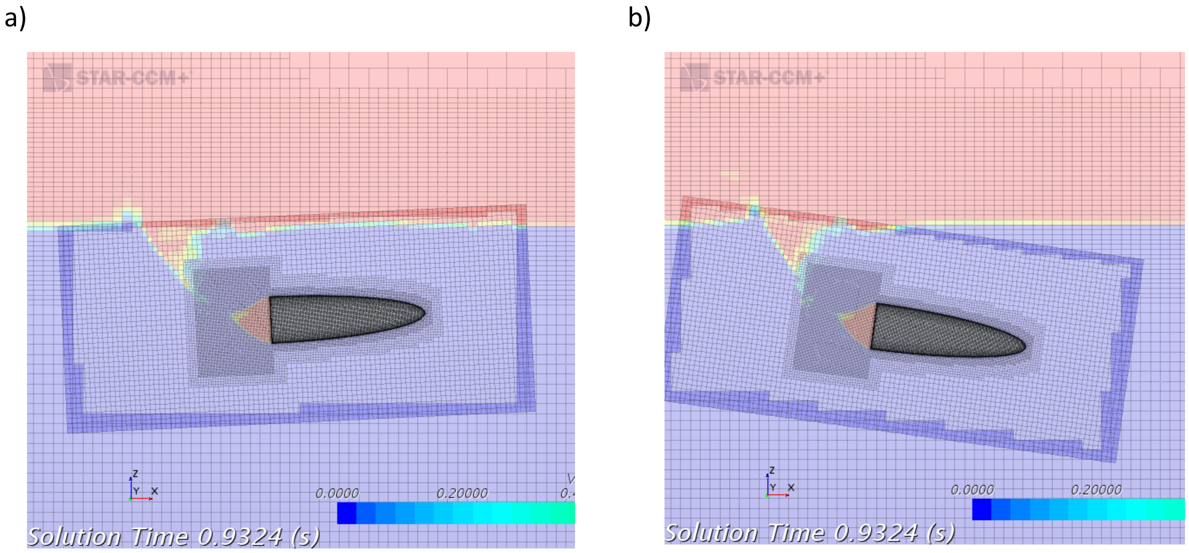

Figure 7.3: a) shows a picture of water entry angle 55° and b) shows a picture of water entry angle 65° at 0.9324s

The beginning of the air cavity closure can be seen from Figure 7.3, the time of the peak can be seen from Table 7.3. The VOF-pictures shows that case a) has started turning upwards, while case b) continues to decent.

7.3 COG

As earlier mentioned, the COG will be affected by the number of passengers and their seating arrangement. Three different values of COG in z-axis has been tested to see how the change in COG affects the behaviour of the free-falling lifeboat. The values are -0.3 m, -0.5 m and -0.7 m measure from the symmetrical centre line of the body.

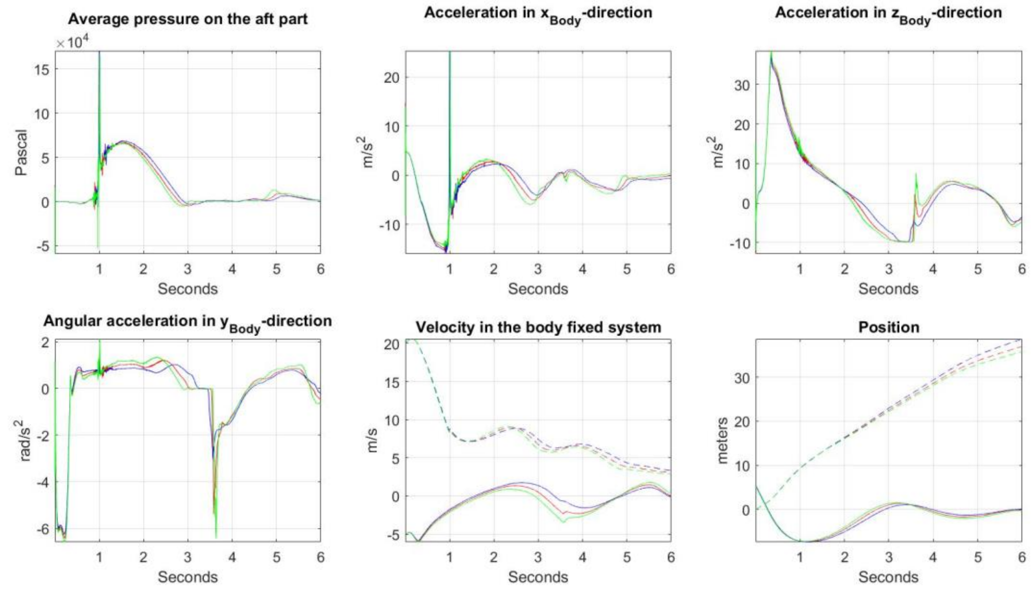

Figure 7.4: Result plots with different centre of gravity in z-direction, where blue is -0.3m, red is -0.5m and green is -0.7m. The accelerations and velocities are taken in the body fixed coordinate system. The dashed lines are in the x-direction, and the solid lines are in the z-direction for the velocity and position plots.

DISTICTIVE PARAMETER	-0.3 m	INITIAL CONDITION	-0.7 m
CAVITY CLOSURE TIME (PEAK) $[s]$	0.999	1.009	1.012
WATER EXIT TIME $[s]$	2.907	2.730	2.620
POP-UP HEIGHT $[m]$	1.083	1.369	1.516
MAXIMUM SUBMERSION $[m]$	-7.381	-7.297	-7.245
SAILING DISTANCE AT 6 s $[m]$	38.637	36.969	35.816
VELOCITY x_{Body} AT 6 s $[m/s]$	3.352	3.109	2.938
ACCELERATION x_{Body} PEAK MAGNITUDE $[m/s^2]$	25.306	21.678	25.297
MAX PRESSURE AFTER CAVITY CLOSURE $[kN/m^2]$	68.980	67.460	66.270

Table 7.4: Distinctive values for comparison of a change in centre of gravity in z-direction

The motion plot in Figure 7.4 reveals that the deepest maximum submergence, and the highest pressure after cavity closure, occur when the COG_Z is moved upwards. However, the difference is relatively small between the different cases. When the COG_Z is moved upward, the gravity-buoyancy arm becomes relative smaller. This result in a small counter clockwise rotation contribution in the water entry and in the submerged phase to the point where the body lies horizontal in the water. After this point, the gravity-buoyancy arm will contribute to a clockwise rotation. The behaviour is the same when moving the COG_Z downward, but the arm is now longer, and contributes to a larger counter clockwise rotation before taking the horizontal position. This leads to the highest water exit angle, despite that the gravity-buoyancy arm counteract this rotation in the ascent. The water exit speed is approximately the same for all three cases, thus the most negative COG_Z gives the highest pop-up height. The water exit occurs last, and with the lowest water exit angle, for the case with the least negative COG_Z. This case gives the longest sailing distance as it has the largest water exit velocity.

7.4 Conclusion/ Discussion for the parameter investigation

The results shows that changing the maximum initial velocity with $\pm$ 5 m/s has the largest effects on the behaviour of the body. It manifests as the highest and lowest values in the air cavity closure time, pop-up height, acceleration peak magnitude, horizontal sailing distance and velocity at 6 s. It also manifests as the least maximum submergence and earliest water exit time for the lowest and highest initial velocity, respectively. By changing the water entry angle with $\pm 5°$, it shows great effect in the maximum average aft pressure, as it also has the largest maximum submergence. The highest and lowest values in maximum submergence is found for the highest and lowest water entry angle, respectfully. The latest water exit time and deepest submergence is also found for the highest water entry angle. The rearrangement of the COG with $\pm$ 0.2 m in z_{body} gave smallest effects, the only significant difference was the angular accelerations and the pop-up height difference.

8 Free-falling lifeboats in wave conditions

As mentioned, an evacuation scenario where free-falling lifeboats are utilized will probably not consist of calm water, perhaps with the exception of a fire scene. A probable scenario is diving in storm conditions. Then wind, waves and current will have large effect on the free-falling lifeboat. The waves can be breaking, leading to strongly non-linear effects. All the different external forces makes the topic even more complex. In this section, the lifeboat will be tested in incident regular waves to see how the forces affects the behaviour of the free-falling lifeboat. Although the effective diving height can change dependent on which wave phase the body enters in, which can lead to changes in the impact velocity and the water entry angle, these parameters has been held constant.

8.1 Modeling waves in Star-CCM+

In Star CCM+, the waves are modelled in physics, under continua. The wave model is applicable for marine applications with motion in six degree of freedom. It requires a three-dimensional space, an eulerian multiphase material and volume of fluid (VOF) as the eulerian multiphase model. The VOF wave properties consists of two wave damping constants f_1 and f_2, a damping exponent n_d and a forcing constant. For enabling damping of waves, the vertical motion must be resisted. This is arranged by adding a resistance term into the vertical velocity (w) equation:

$$S_z^d = \rho \, (f_1 + f_2 \, |w|) \, \frac{e^{\kappa} - 1}{e^{1} - 1} \, w \tag{38}$$

Where:

$$\kappa = \left(\frac{x - x_{sd}}{x_{ed} - x_{sd}} \right)^{n_d} \tag{39}$$

x_{sd} and x_{ed} is the point where the waves damping starts and ends, respectively.

The forcing of the discretized Navier-Stokes equation towards the theoretical solution is achieved by introducing a source term to the transport equation on the form:

$$q_{\phi} = -\gamma\rho(\phi - \phi^{*}) \qquad [40]$$

Where γ is the forcing coefficient, ϕ is the current solution of the transport equation and ϕ^{*} is the value of the forced solution. The problems associated with reflection of surface waves at boundaries are eliminated by introducing wave forcing. (Steve CD adapco, 2016)

The VOF waves model is selected, and it is possible to choose alternative wave settings; Flat wave, first order VOF waves, fifth order VOF waves, Cnoidal waves, superposition waves and irregular waves. For this thesis, where the purpose is to study the behaviour of the lifeboat in waves, regular first order VOF waves will be sufficient, as the physics will be easier to interpret.

The first order VOF wave set-up let the user chose wave length or period, wave height, advancing direction, vertical direction, point of water level of where the first down crossing point is located, wind and current specifications and if deep water approximations is to be applied. Light and heavy fluid density, that is the density of air and water, are also specified here.

In able to run the simulation in wave conditions, all the field functions are changed to first order VOF waves. The domain boundaries specified in region are all set to velocity inlet, except for one of the domain boundary, which have to be set as pressure outlet. The pressure outlet boundary condition is more sensitive to the motion of fluid, and for the cases with head waves, this boundary has been set on the top of the domain. The domain and their boundaries can be seen in Figure 4.3.

8.2 First order VOF waves

The first order VOF waves approach generates regular periodic sinusoidal waves. When assuming a wave propagating in the positive x-axis with a wave crest in $x = 0$, the horizontal particle velocity can be written as:

$$u = a\omega \cos(\boldsymbol{K} \cdot \boldsymbol{x} - \omega t)\, e^{Kz} \tag{41}$$

and a vertical velocity as:

$$w = a\omega \sin(\boldsymbol{K} \cdot \boldsymbol{x} - \omega t)\, e^{Kz} \tag{42}$$

The surface elevation is given by:

$$\eta = a * \cos(\boldsymbol{K} \cdot \boldsymbol{x} - \omega t) \tag{43}$$

- a is the wave amplitude
- $\omega = \frac{2\pi}{T}$ is the wave frequency
- $\boldsymbol{K}$ is the wave vector
- $K = \frac{2\pi}{\lambda}$ is the magnitude of the wave vector
- z is the vertical distance from the mean water level

The wave period is given by

$$T = \frac{2\pi}{\omega} \tag{44}$$

And the wave length is given by

$$\lambda = \frac{2\pi}{K} \tag{45}$$

For finite water depths, the dispersion relation between the wave period and the wave length is given as

$$T = \left(\frac{g}{2\pi\lambda}\tanh\left(\frac{2\pi d}{\lambda}\right)\right)^{-0.5} \tag{46}$$

It is assumed that the free-falling lifeboat will dive in deep water depth ($d > \frac{\lambda}{2}$). At this theoretical intersect, hyperbolic tangent of π is close to 1 and it continues to move asymptotically toward 1 as the ratio $\frac{d}{\lambda}$ increases. Thus, for deep water depth, the dispersion relation can be simplified to:

$$\lambda = \frac{gT^2}{2\pi} \tag{47}$$

and it is independent on the water depth value. (Steve CD adapco, 2016)The phase velocity is given as

$$c_p = \frac{\omega}{K} \tag{48}$$

The maximum horizontal particle velocities for linear waves occurs at the wave crest and in the wave trough, with opposite direction. The particle velocity in the wave crest has the same direction as the wave propagation. They are purely horizontal velocities, and can be taken as

$$u_{max} = a\omega \tag{49}$$

The largest vertical velocity is to be located in the mean surface on either side of the wave crest. It is acting upward and downwards in the front and behind of the wave crest, respectively. It can be taken as

$$w_{max} = \pm a\omega \tag{50}$$

(Steve CD adapco, 2016)

8.3 Wave forces on the body

By adding waves into the simulation, the body gets subjected to additional forces. Waves are responsible for Froude-Krylov forces, diffraction forces and additional drag. The non-viscous forces are the Froude-Krylov force and the diffraction force. For the Froude-Krylov force, the undisturbed waves generate an unstable pressure field. The diffraction force comes from disturbance in the waves from the submerged or floating body.

The dynamic pressure dependent on the wave phase, wave amplitude and water depth, and is given as

$$P_{dyn} = \rho g a * \cos(kx - \omega t)\, e^{Kz} \tag{51}$$

The drag force on a body with relative fluid-body velocity v_r is given as

$$F_D = \frac{1}{2}\rho v_r^2 C_D A \tag{52}$$

Where C_D is the drag coefficient and A is the projected area. (Faltinsen, 1990) (DNV-GL, 2016)

8.4 Selecting wave parameters

When applying first Order Stokes waves to the simulation, a wave length and a wave height must be selected. When modelling first order regular wave in Star-CCM+, the waves cannot have a too large steepness, $\frac{h}{\lambda}$, wave height over wave length. If this is the case, they will get unstable and eventual break, as it will in nature. To find a steepness that makes the waves behave like first order regular waves, several waves with different steepnesses has been tested. It is desirable to have waves that will properly reveal the effect of wave interference, that is waves with high particle velocities. This resulted in waves with high steepness without breaking. The wave height and wave length that were chosen for all the different wave phases and wave headings were chosen to be 7 m and 85 m, respectively. To see how the steepness affects the behaviour of the body, two additional wave heights has been tested. The wave length has been held constant, and the two additional wave heights are chosen to be 5 m and 3 m.

8.5 Selecting wave heading and wave phases

It is desirable to investigate diving in different wave headings and wave phases to see how these affects the behaviour of the body. The wave heading is specified in Star CCM+ by deciding the advancing direction and the point of water level, that is the point of the first down crossing point. This is selected in the first order VOF waves in physics under continua. The point of water level must be specified in the same direction as the advancing direction. The wave phases are selected so that the particle velocity will act in four different direction at impact. The wave phases chosen are shown in Figure 8.1, where $0\ rad$ gives horizontal particle velocity in the wave propagation direction, $\frac{\pi}{2}\ rad$ gives upward particle velocity, $\pi\ rad$ gives horizontal particle velocity in opposite direction of the wave propagation and $\frac{3\pi}{2}\ rad$ gives downwards particle velocity.

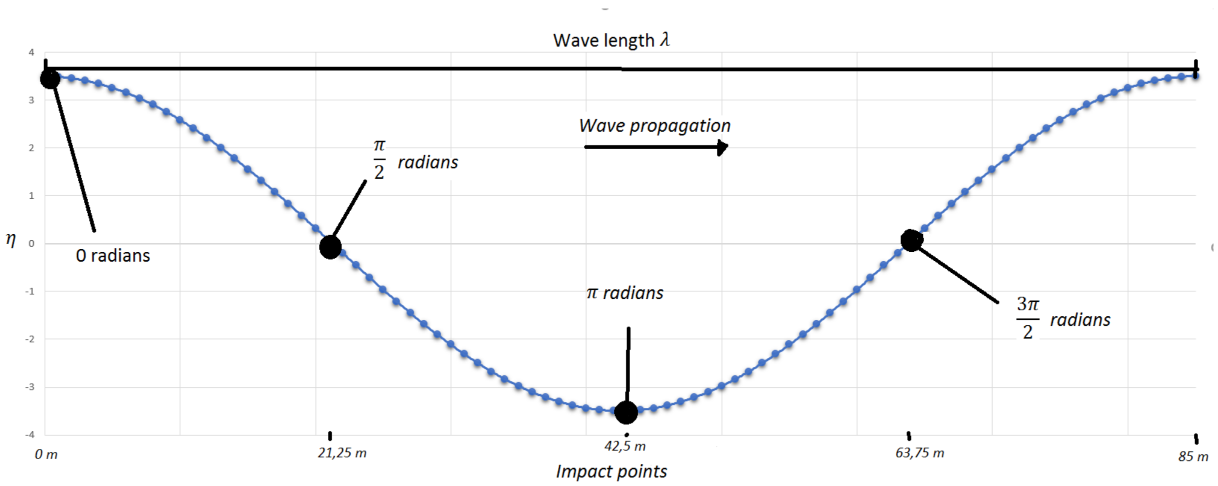

Figure 8.1: Wave phase impact points

CASE NUMBER	WAVE HEADING	PHASE	WAVE HEIGHT	WAVE LENGTH
1	Following	0 rad	7 m	85 m
2	Following	$\frac{\pi}{2}$ rad	7 m	85 m
3	Following	π rad	7 m	85 m
4	Following	$\frac{3\pi}{2}$ rad	7 m	85 m
5	Head	0 rad	7 m	85 m
6	Head	$\frac{\pi}{2}$ rad	7 m	85 m
7	Head	π rad	7 m	85 m
8	Head	$\frac{3\pi}{2}$ rad	7 m	85 m
9	Beam	0 rad	7 m	85 m
10	Beam	$\frac{\pi}{2}$ rad	7 m	85 m
11	Beam	π rad	7 m	85 m
12	Beam	$\frac{3\pi}{2}$ rad	7 m	85 m
13	Following	0 rad	5 m	85 m
14	Following	0 rad	3 m	85 m
15	Head	π rad	5 m	85 m
16	Head	π rad	3 m	85 m
17	Beam	$\frac{\pi}{2}$ rad	5 m	85 m
18	Beam	$\frac{\pi}{2}$ rad	3 m	85 m

Table 8.1: Simulated cases

8.6 Modifications of the mesh from flat wave conditions

The bow position of the body is placed 20 cm above the water surface in every case. Thus, for the cases where the body enters in a wave trough or a wave crest, the body-fixed coordinate system and all the parts in the overset mesh is to be translated in the global z-direction. The simulations were first run with the coarse mesh to see how the waves affected the trajectory. As the overset follows the body, it is possible to see how the overset interacts with the other parts in the grid. And as mention in 4.2 Boundary conditions, the finer cells should not be smaller than halve the cell size it interacts with. The time step was set to 0.001 s, which enables highlighting of possible turbulence problems. The course mesh simulations revealed that the water surface was too short for some cases, as the finest cells interacted with the course ones. Hence, an increase in the water surface part was necessary. It also revealed that the air cavity closes outside the “box-behind” part of the overset for when the body enters in head waves in a crest, hence an increase along the body fixed x-axis was necessary to properly capture the air cavity closure. For the cases of diving in beam-sea waves, the overlap and water surface part where increased in the y_{global}-direction, as the body will get significant translation in this direction.

8.7 Results

The output that will be presented from the simulations are acceleration, position, angular velocity and surface average pressure. The sway accelerations, sway motion, roll velocity and pitch velocity are insignificant for following-sea waves and head-sea waves, and will not be presented for these two headings.

The accelerations and position are measured in the centre of gravity of the body. The z_{body} position is plotted with mean water surface as the zero point referance in the global z-axis. For beam-sea waves, the positive y-axis is in the portside direction. For some of the acceleration and average pressure aft plots, some noise is detected right before and after the air cavity closure (at approximately 6 s), these small peaks will not be taken into account when the distinctive values are measured, as they are assumed to be unphysical. The reason for this is that the air is modelled as incompressible, while in reality it will be compressible. These peaks are assumed to have small effect on the global behaviour, due to their short duration. The six degrees of freedom are defined as showed in Figure 8.2.

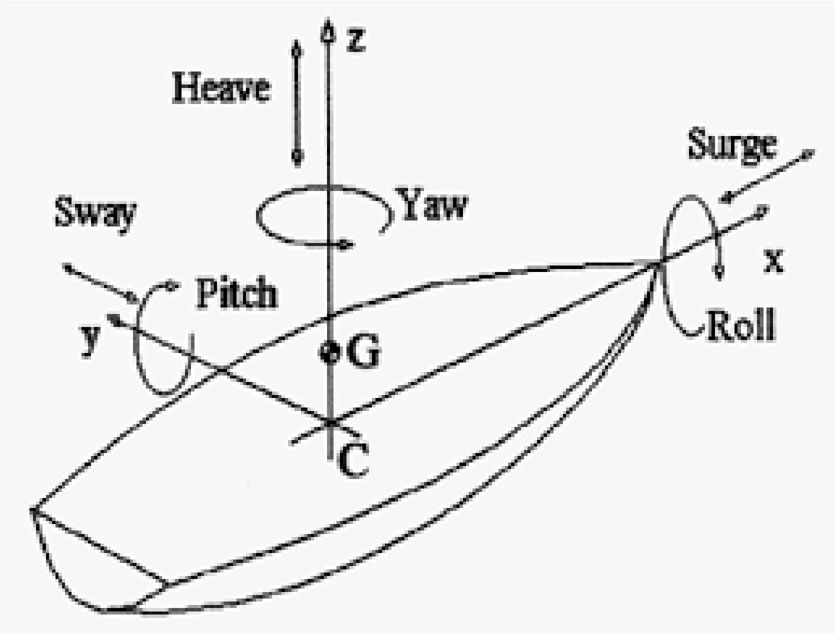

Figure 8.2: Definition of the six degrees of freedom

8.7.1 Case 1, following sea, 0 radians, wave height 7 m

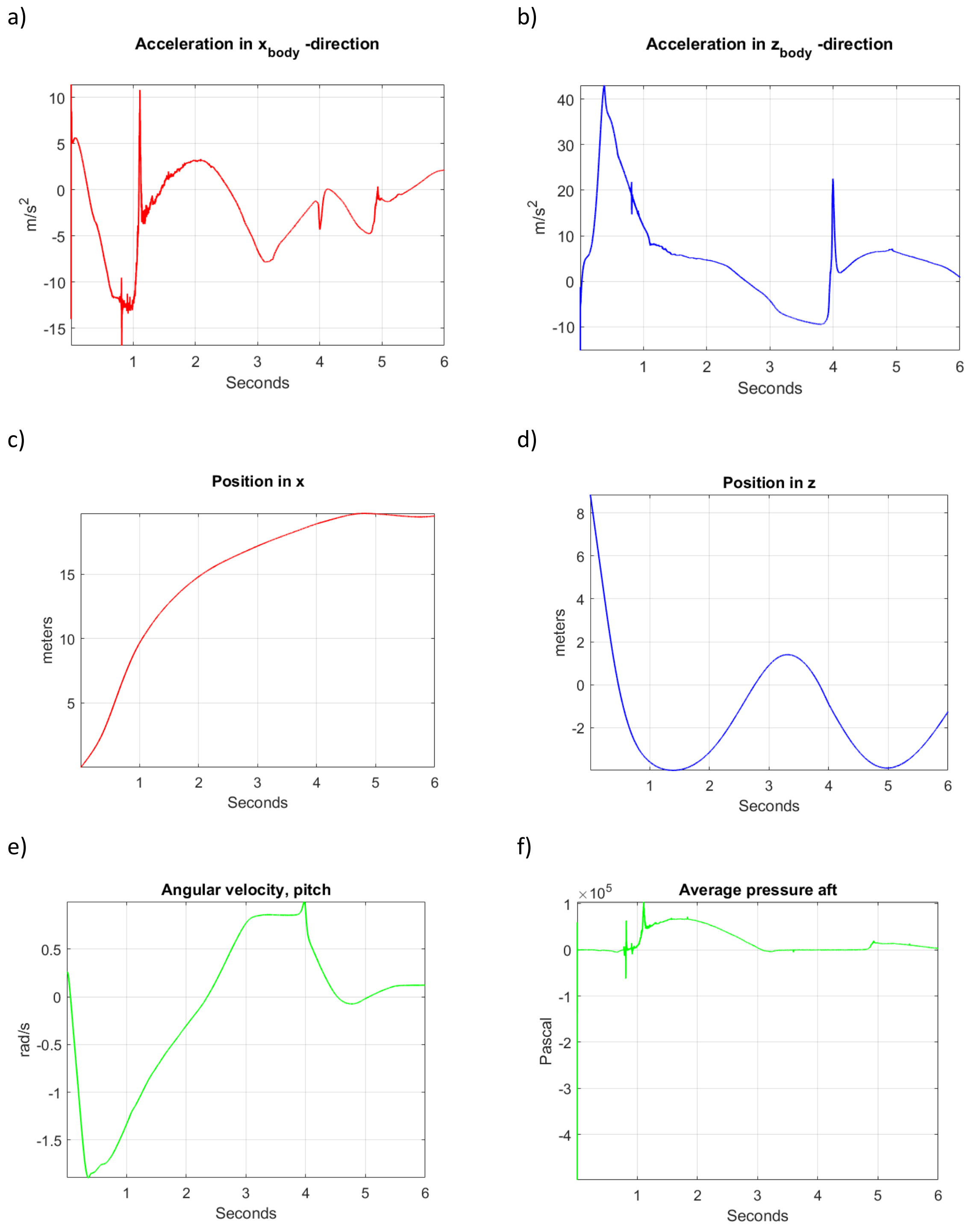

Figure 8.3: Computed time-histories for acceleration, position, angular velocity and average pressure aft, case 1

The body dives into a wave crest where the horizontal particle velocity is at its maximum and in the same direction as the wave propagation. The bow gets an added motion in the global x-direction in the entering phase. This leads to fast counter clockwise pitching, and increase slamming loads in the aft part, leading to a large positive acceleration in z_{body}. The increase of the counter clockwise pitch velocity stops due to slamming on the aft part. This is also where the acceleration in z_{body} has its maximum. In the early water entry phase, the wave propagates faster than the body in the global x-direction, and as the body has turned counter clockwise, the aft part is the first to get into the wave phase where the velocity is acting downwards. This causes a contribution to counter clockwise rotation, however small. And combined with the large initial counter clockwise rotations, it leads to a high water exit angle, and thus low contribution in x_{global} water exit velocity. The result is a short sailing distance in x_{global} direction, and as the body eventually is located in a wave trough, it gets a small translation towards the evacuation scene, as seen in Figure 8.3 c).

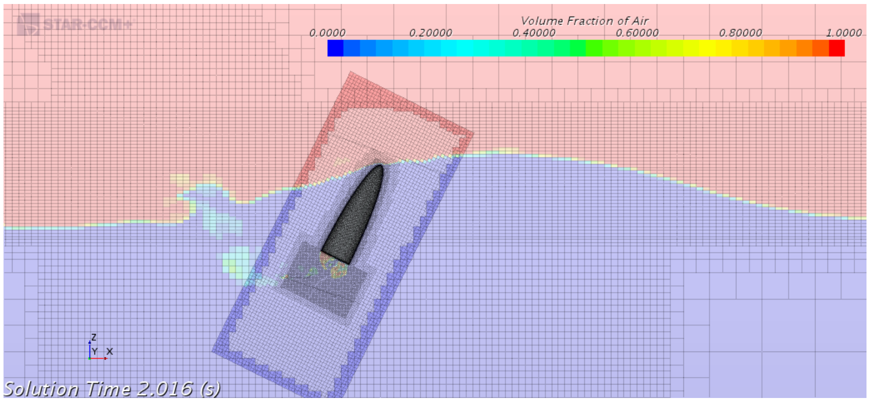

Figure 8.4: Case 1, the body exits the water with high water exit angle and at a short distance from the impact position.

8.7.2 Case 2, following sea, $\frac{\pi}{2}$ radians, wave height 7 m

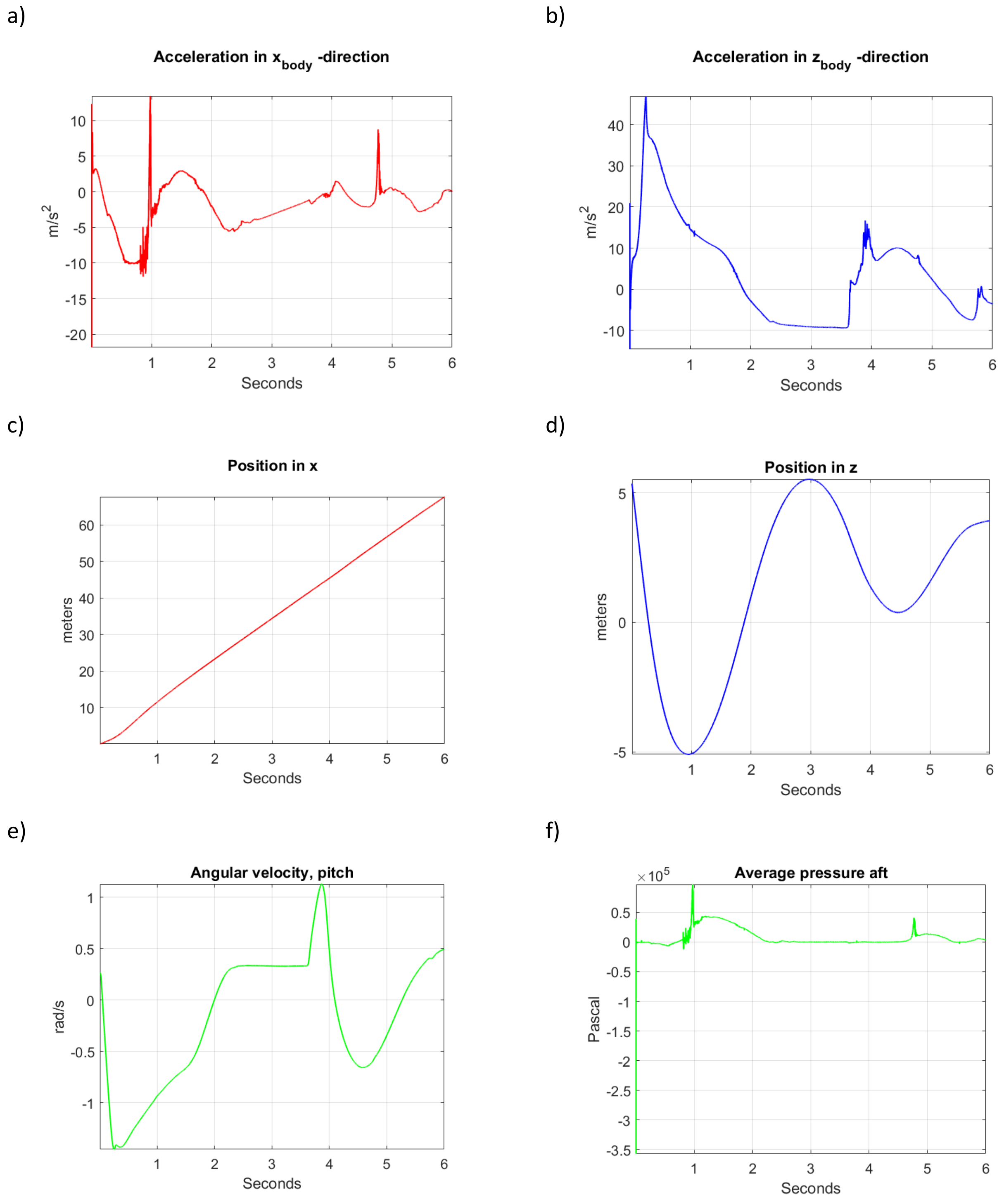

Figure 8.5: Computed time-histories for acceleration, position, angular velocity and average pressure aft, case 2

The body dives into a wave phase where the particle velocity is acting upwards, increasing the momentum in the counter clockwise direction, and leads to large accelerations on the body. For this case, the slope of the wave creates a small angle between the body centre line and the surface of the wave. This results in a short time before the slamming of the aft part occurs. The wave propagation velocity is approximately the same as the body velocity in the global x-direction, and the body exits at a short distance behind the wave phase $\frac{\pi}{2}$ radians. As the fluid motion is acting in the same direction as the body, it contributes together with the buoyancy force to push the body through the water surface with large x_{body} velocity. This results in a relatively long air time. The propagation velocity of the waves is almost equal to the global x-velocity when the body flies through the air. Hence, the body re-enters the water surface in the phase $\frac{\pi}{2}$ radians. When the body re-enters the surface, it breaks up the linear behaviour near the wave, and the kinetic energy is transferred from the wave crest to the body, and as seen in Figure 8.5 c) it gets the longest sailing distance of all the cases, by far. The peak apparent at 4.8 s, in Figure 8.5 a), comes from the breaking crest slams into the aft of the body.

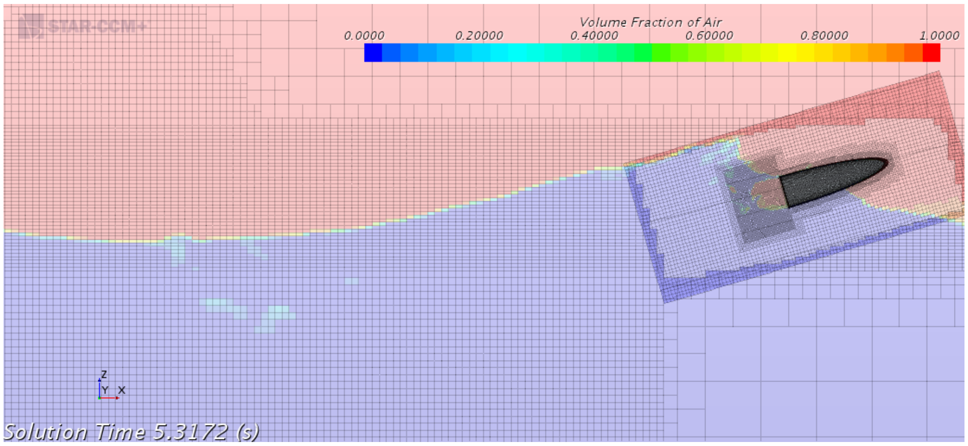

Figure 8.6: Case 2 at 5.3 s. The body is affected by the wave crest after the re-entering of the surface.

8.7.3 Case 3, following sea, π radians, wave height 7 m

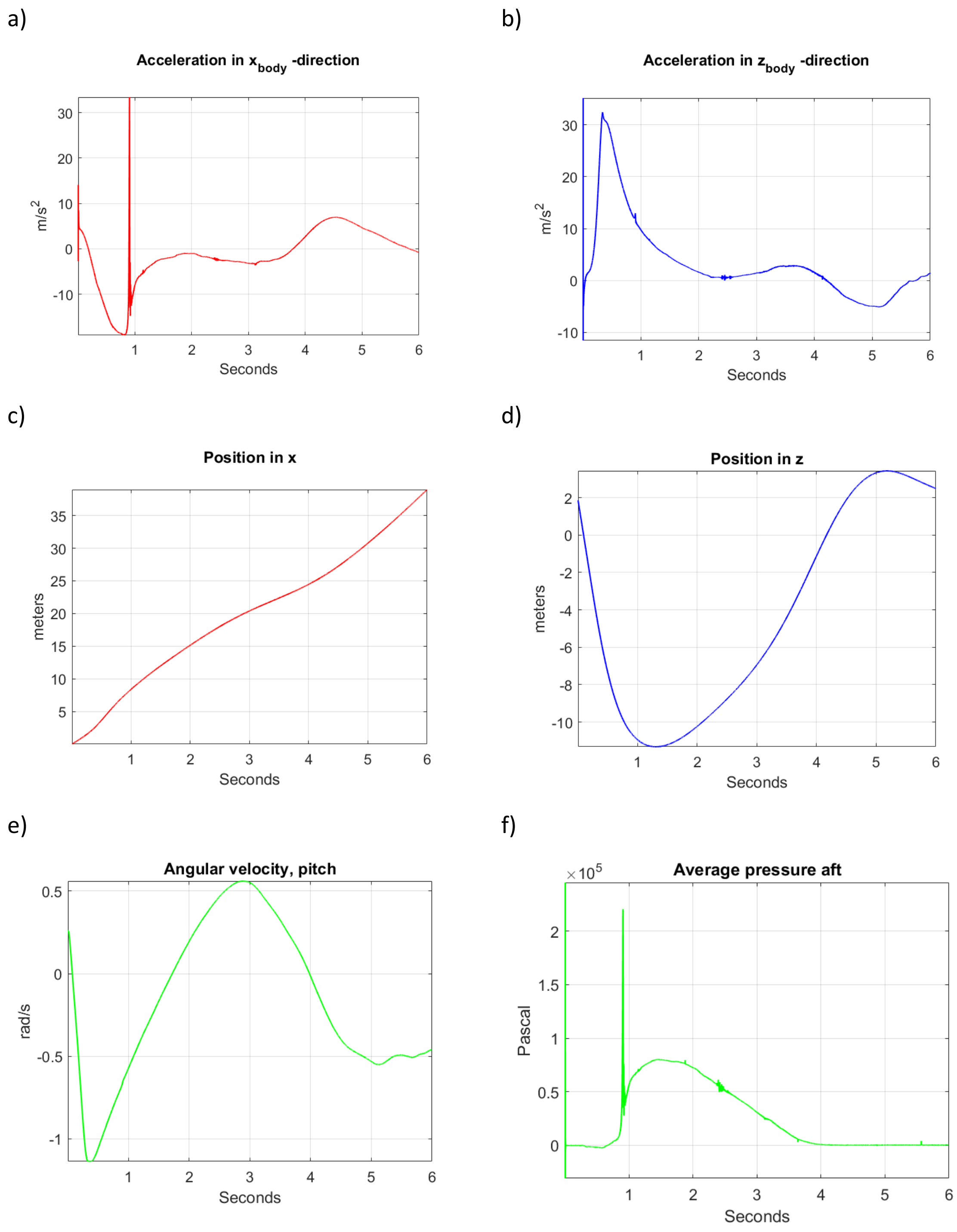

Figure 8.7: Computed time-histories for acceleration, position, angular velocity and average pressure aft, case 3

The body dives into a wave trough, where the particle velocity is acting in the opposite direction of the wave propagation. It causes a relatively low counter clockwise pitch rotation, the body is downward directed for a longer time, and this leads to smaller slamming forces on the aft part. Figure 8.7 b) shows the relative small peak at 0.3 s. Eventually the body gets into the $\frac{\pi}{2}$ phase, as the wave propagating faster than the body. The particle velocity in this phase is acting upward and in the same direction as the buoyancy, hence the aft part is pushed in this direction. This resulting in that the body exiting the water surface with the aft first in the $\frac{\pi}{2}$ phase. The body is eventually located in the wave crest where it gets a large contribution in forward motion as the wave crest pushes on the aft part. Case 3 gets a large average surface pressure as it has a submerged value of almost 12 m below the mean water surface, hence a large hydrostatical pressure at this point. However, the body is located under a wave trough, hence a reduction in average pressure due to the dynamic pressure.

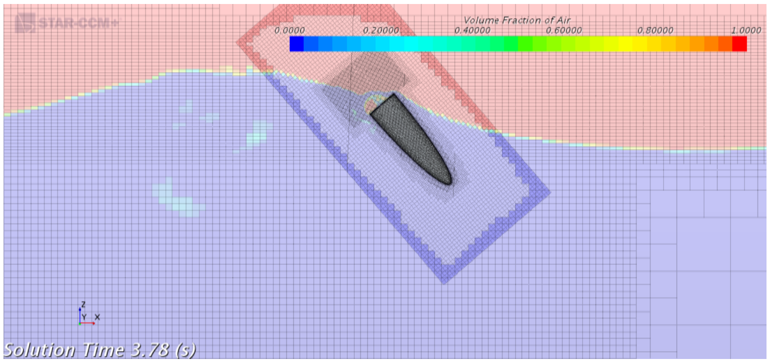

Figure 8.8: Case 3, right before water exit. The body exits with the aft first

8.7.4 Case 4, following sea, $\frac{3\pi}{2}$ radians, wave height 7 m

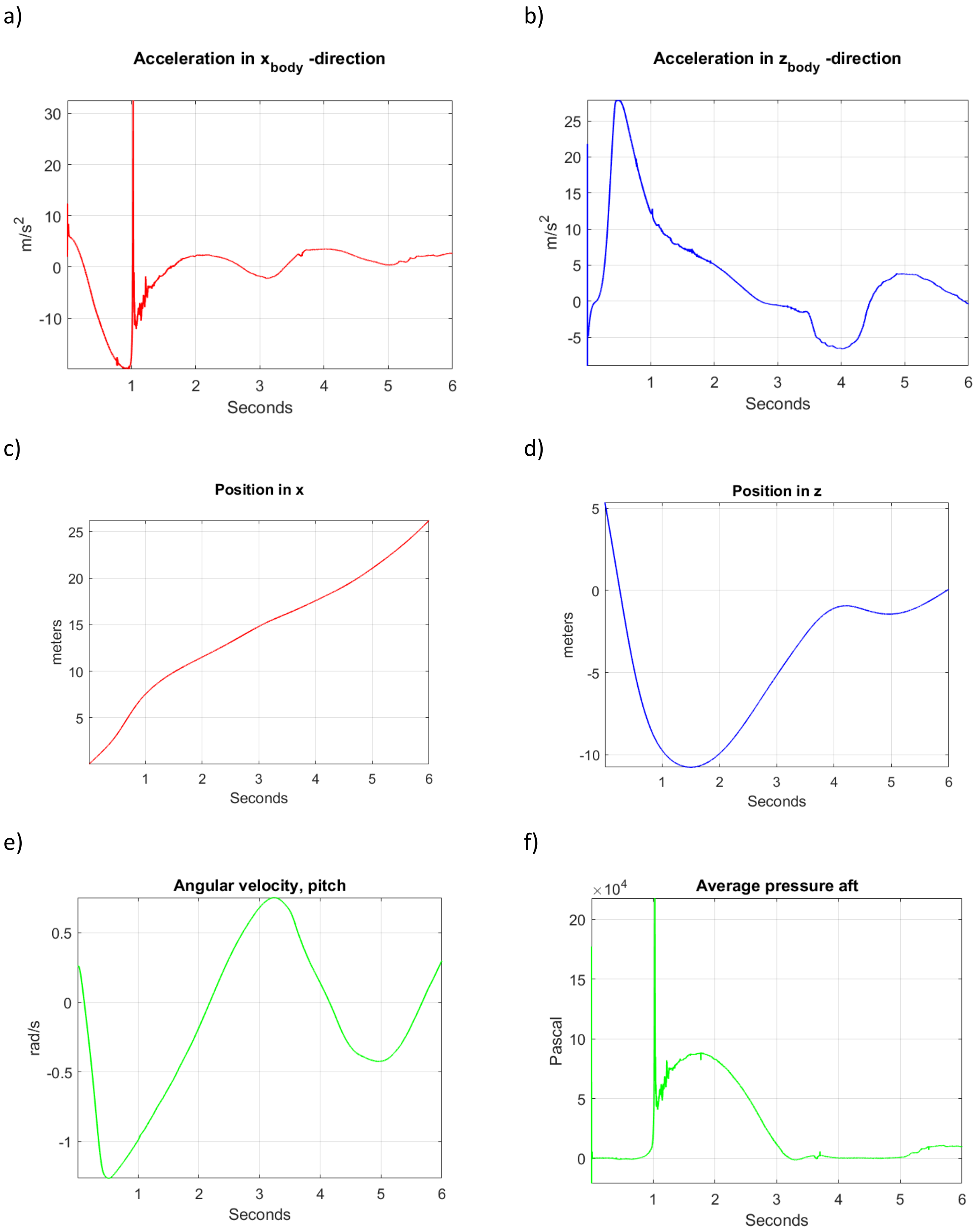

Figure 8.9: Computed time-histories for acceleration, position, angular velocity and average pressure aft, case 4

The body dives into a wave phase where the particle velocity is acting in the negative vertical direction. Since the particle velocity is acting in the same direction as the vertical motion of the body, there is a relative small maximum z_{body} acceleration in the water entry phase. The wave elevation decreases as the body moves downwards, causing a late slamming of the aft part, hence the counter clockwise pitch acceleration works for a relative long time. The body has a relatively small x_{global} motion in the water entry phase, hence it is soon affected by the particle velocity in the negative x_{global} direction close to the wave trough. Water exit occurs in the wave trough with a small forward motion. The penetration of the water surface breaks up the linearity of the wave, leading to a positive acceleration at the end of the time series, as the wave crest pushes the body forward.

8.7.5 Case 5, head sea, 0 radians, wave height 7 m

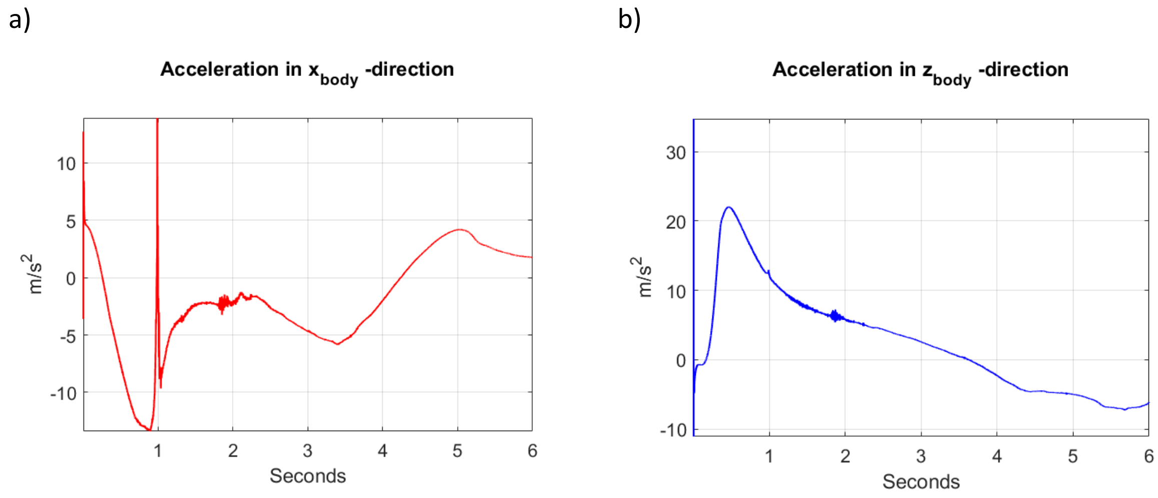

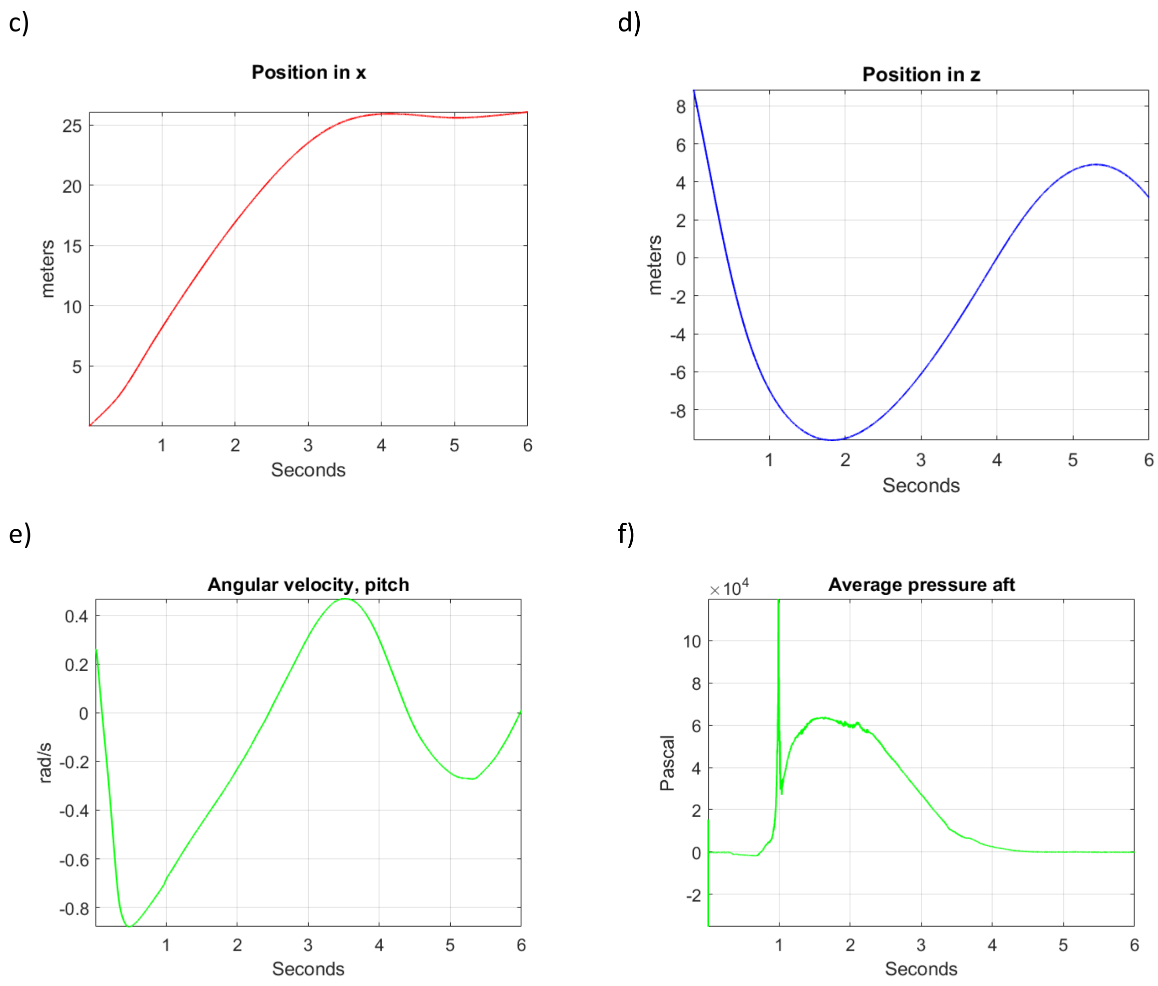

Figure 8.10: Computed time-histories for acceleration, position, angular velocity and average pressure aft, case 5

The body enters in the wave crest, in head-sea waves. The fluid velocity is acting in the same direction as the wave propagation and in the opposite direction of the motion of the body. This creates a small angular velocity in the water entry phase, which leads to small slamming loads on the aft of the body. The body is soon influences by the $\frac{3\pi}{2}$ wave phase, where the fluid velocity is acting downwards. The body gets a large maximum submergence, with a slow counter clockwise rotation. The counter clockwise rotation is eventually reversed, as the body is eventually located in the $\frac{\pi}{2}$ phase where it gets lifted up by the buoyancy force which acts in the volume centre, and exiting the surface with the aft first. Then it gets a small translation in the direction of the wave propagation as it is located on the wave crest.

8.7.6 Case 6, head sea, $\frac{\pi}{2}$ radians, wave height 7 m

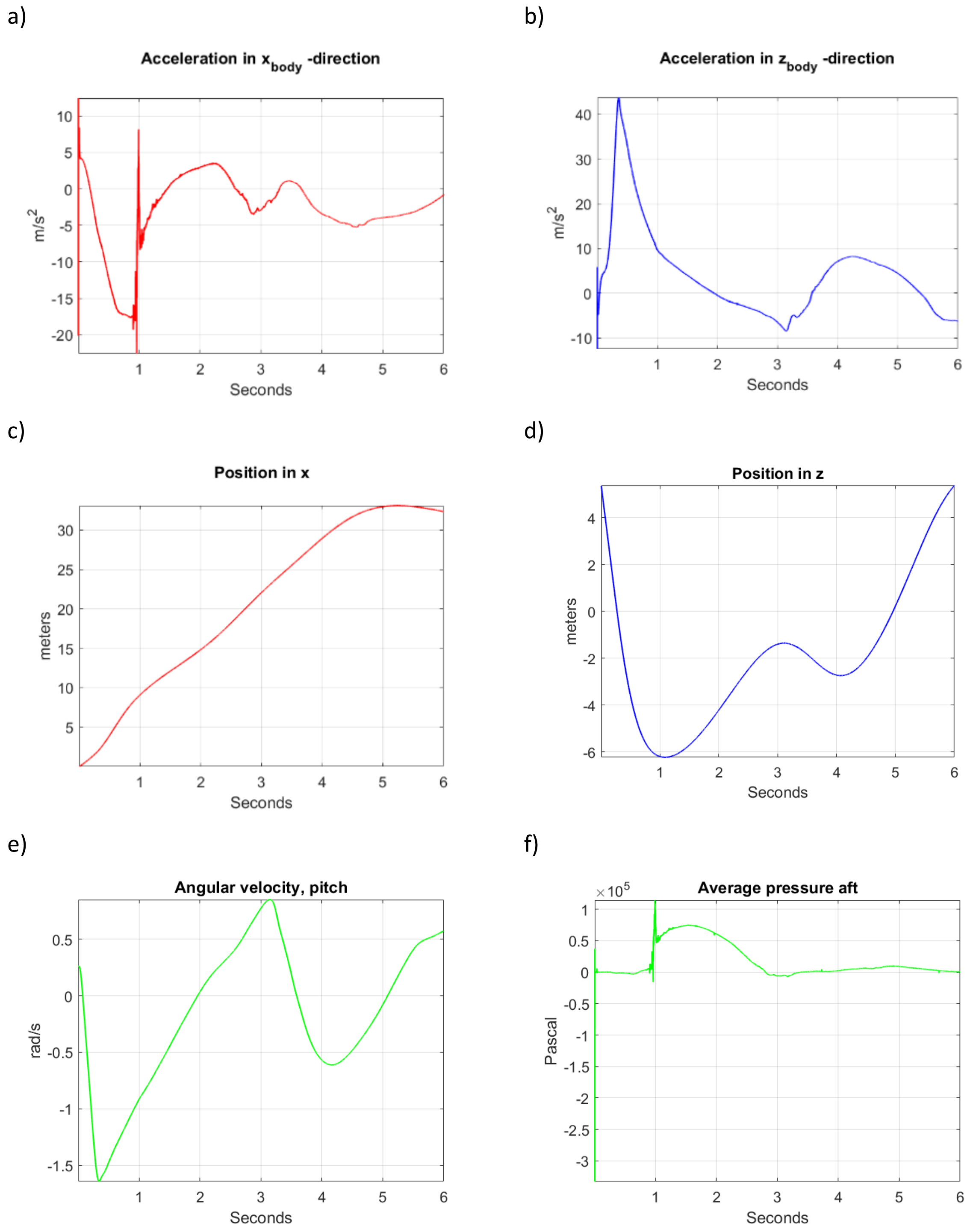

Figure 8.11: Computed time-histories for acceleration, position, angular velocity and average pressure aft, case 6

The body dives into a wave phase where the particle velocity is acting upwards. This contributes to a larger moment in the counter clockwise direction, hence it contributes to counter clockwise rotation. The body is moving in opposite direction of the wave propagation, and after water entry, it starts moving in under the wave crest where the fluid velocity is opposite to the body, creating additional drag, and relatively large accelerations in the negative x_{body}-direction can be seen in Figure 8.11 a). The counter clockwise rotation gets reversed when the body moves towards the $\frac{3\pi}{2}$ phase where the bow gets affected by the negative vertical particle velocity and the aft has the largest buoyancy contribution. It exits with a small water exit angle, between the $\frac{3\pi}{2}$ phase and the wave trough. After the exit, it gets a small positive acceleration contribution as it re-enters in the wave trough. At the end of the simulation, the body is located in a wave crest, getting a small translation in the negative x_{global} direction.

8.7.7 Case 7, head sea, $\boldsymbol{\pi}$ radians, wave height 7 m

a)

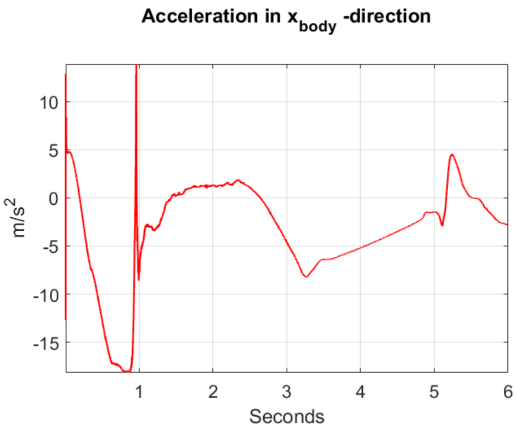

b)

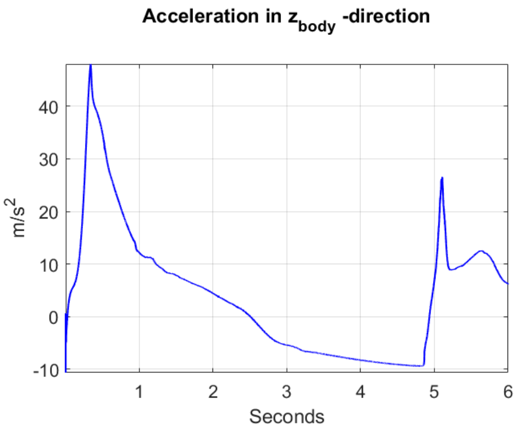

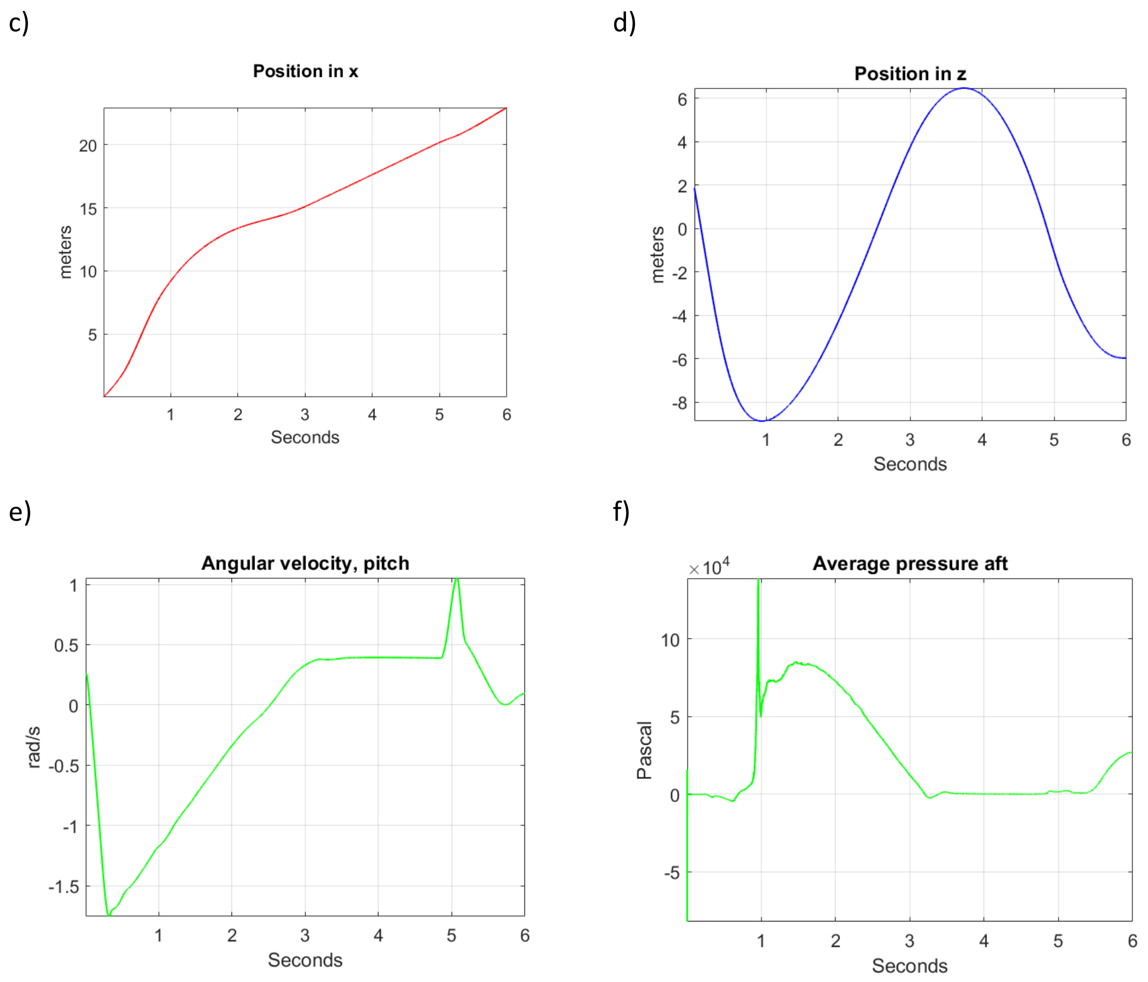

Figure 8.12: Computed time-histories for acceleration, position, angular velocity and average pressure aft, case 7

The body dives into a wave trough, where the particle motion is acting in the global positive x-direction. As the bow is moved in this direction, it results in a large pitch velocity, and a large z_{body} accelerations from the slamming of the aft part. The wave is propagating in the opposite direction of the body. Hence, the body is moving toward the wave phase where the particle velocity is acting upwards. As it enters this phase, the body has an approximately horizontal position. It still has a counter clockwise pitch velocity initiated in the water entry. The upward directed fluid velocity affects the fore part first, creating a small momentum in the counter clockwise rotation. And as it moves in under the wave crest, it has large surge motion contribution in the vertical direction from the buoyancy force. The body exits in a wave crest, and then it flies through the air, and re-enters with the keel aft corner first, this creates additional clockwise pitch and the fore part experience large second slamming forces. It is apparent as the peak in Figure 8.12 b) at 5.1 s.

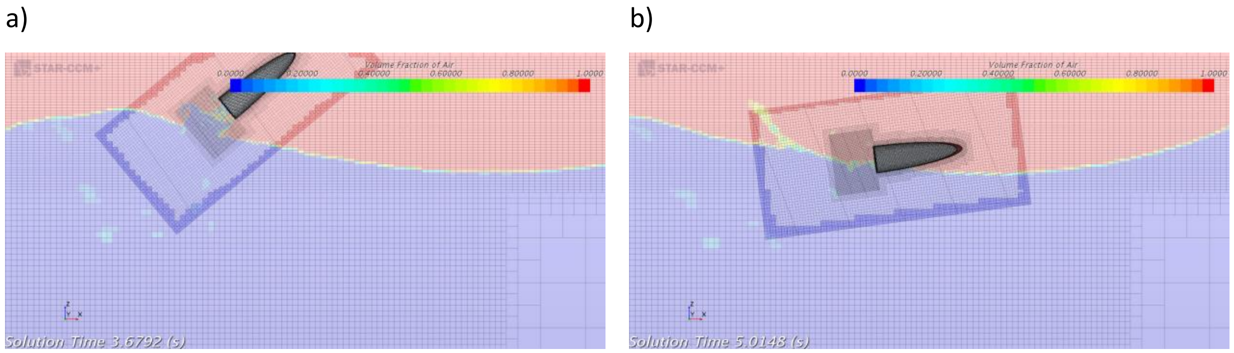

Figure 8.13: a) the body exits from the wave crest at high velocity, b) the body re-enters the water surface with the lower aft part first.

8.7.8 Case 8, head sea, $\frac{3\pi}{2}$ radians, wave height 7 m

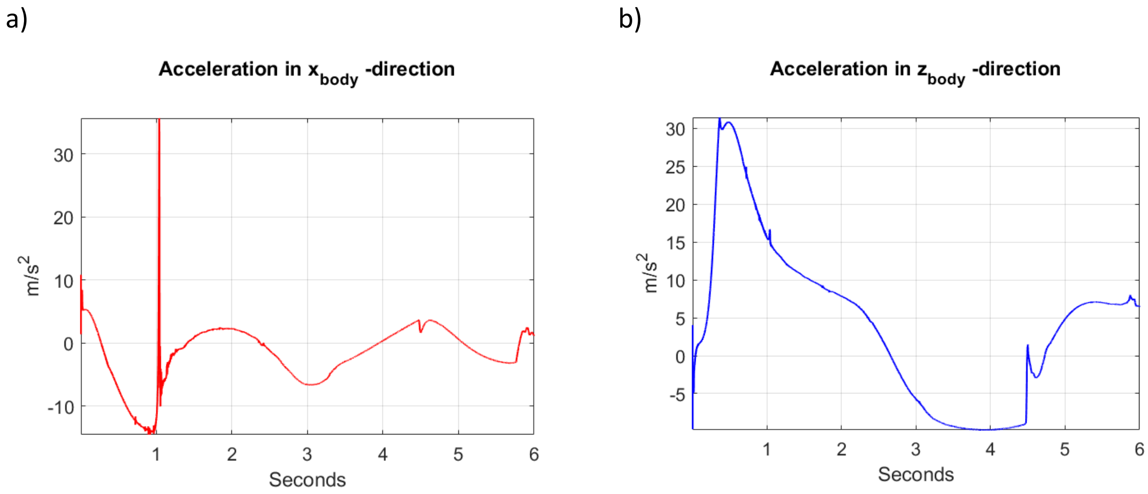

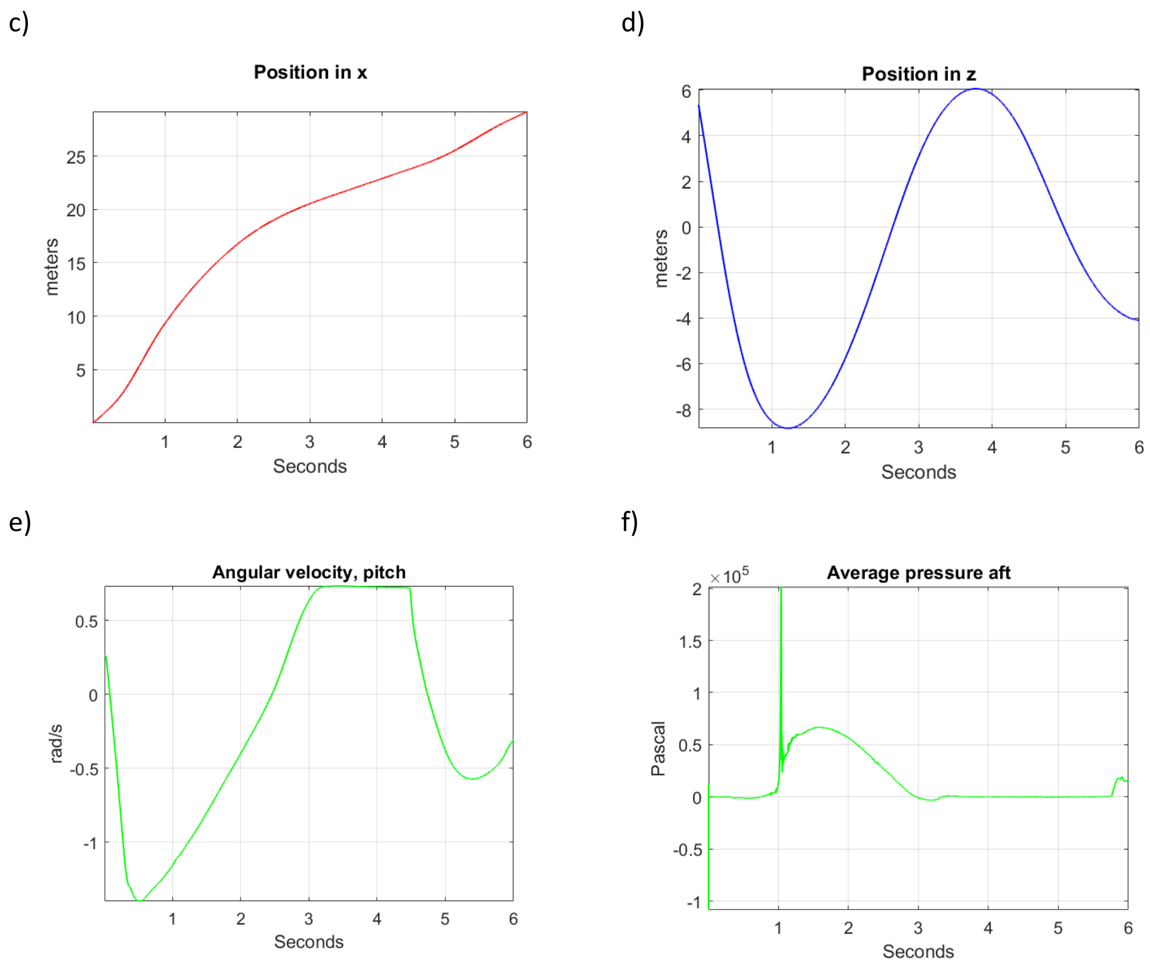

Figure 8.14: Computed time-histories for acceleration, position, angular velocity and average pressure aft, case 8

The body is diving into a wave phase where the particle motion is acting downwards. The relative fluid-body velocity is relatively low, hence the deaccelerations in x_{body} and z_{body} are relatively small. For this case, the body and the particles are moving in the same direction in the tree first phases. After water entry, the body takes the horizontal position under the wave trough, where the particle velocity is in the positive x-direction. Then the body rotates counter clockwise towards an upward vertical direction, the same direction as the particle motion in the phase $\frac{3\pi}{2}$, where it exits through the water surface. Hence, there is a relative small fluid-body velocity in these phases. The kinetic energy from the exit leads to a large pop-up, so that the body flies over the wave crest and re-enters in the $\frac{3\pi}{2}$ phase, where the water entry angle between the body and the surface of the wave is close to zero degrees. However, the velocity has a large x_{body} component compared to the z_{body} component, also the fluid is moving downwards, hence a smaller relative body-fluid velocity and a small second slamming, seen as the acceleration peak in z_{body} direction at approximately 4.6 s, Figure 8.14 b).

8.7.9 Case 9, beam sea, 0 radians, wave height 7 m

a)

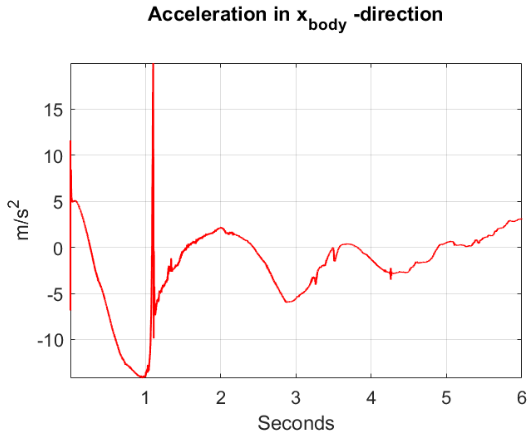
Acceleration in x_{body} -direction

b)

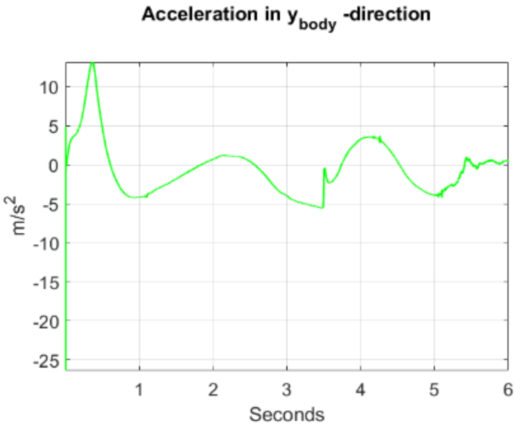
Acceleration in y_{body} -direction

c)

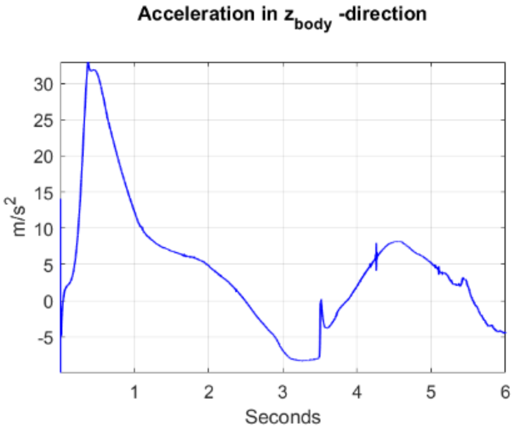
Acceleration in z_{body} -direction

d)

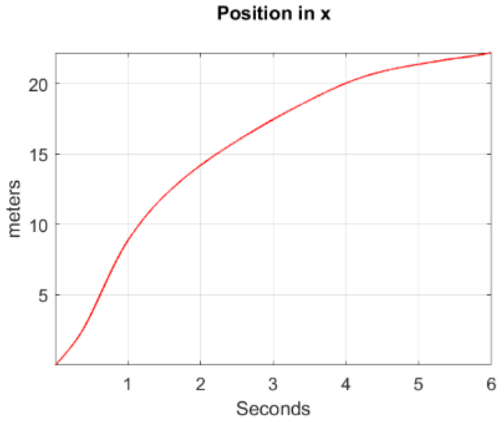
Position in x

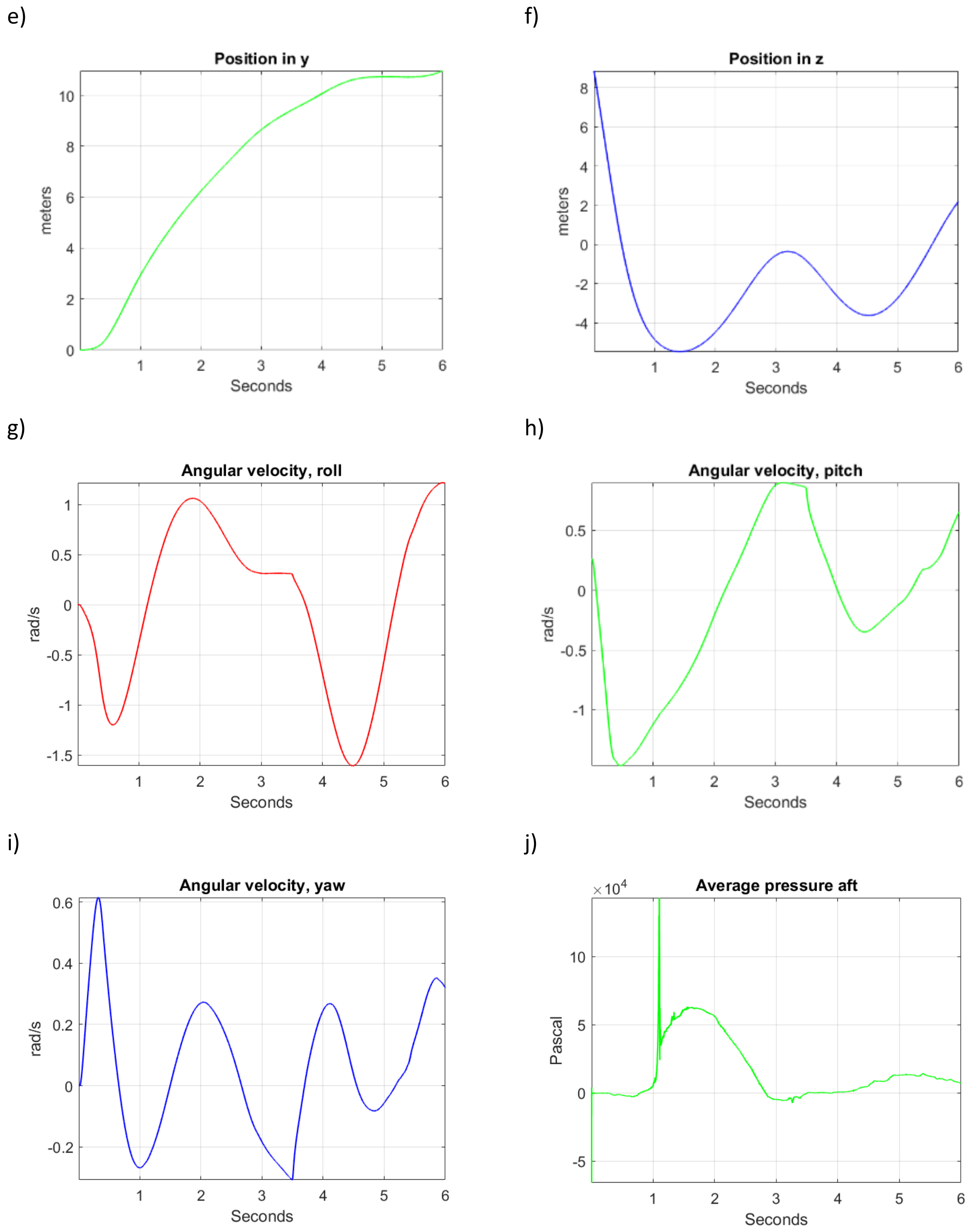

Figure 8.15: Computed time-histories for acceleration, position, angular velocity and average pressure aft, case 9

The waves propagate from starboard to port side, in the positive sway direction. Unlike for following- and head-sea waves, the body experiences an acceleration in y_{body} as well as roll and yaw rotations. For this case, the body dives into a wave crest where the particle velocity is at its maximum and in the same direction as the wave propagation. The body gets a positive acceleration in y_{body}, that is in the portside direction. It also gets a relative large positive yaw velocity and a negative roll velocity. This leads to a translation in y-direction with the direction of the bow more turned towards the direction of the wave propagation. The water exit occurs in the $\frac{3\pi}{2}$ phase. The upwards particle velocity contributes to a small pop-up height, and the second slamming is noticeable at 3.6 s in Figure 8.15 c) After water entry, the yaw and roll oscillates between positive and negative rotations. The body gets a relative small sailing distance in x-direction and a large translation in the positive y-direction.

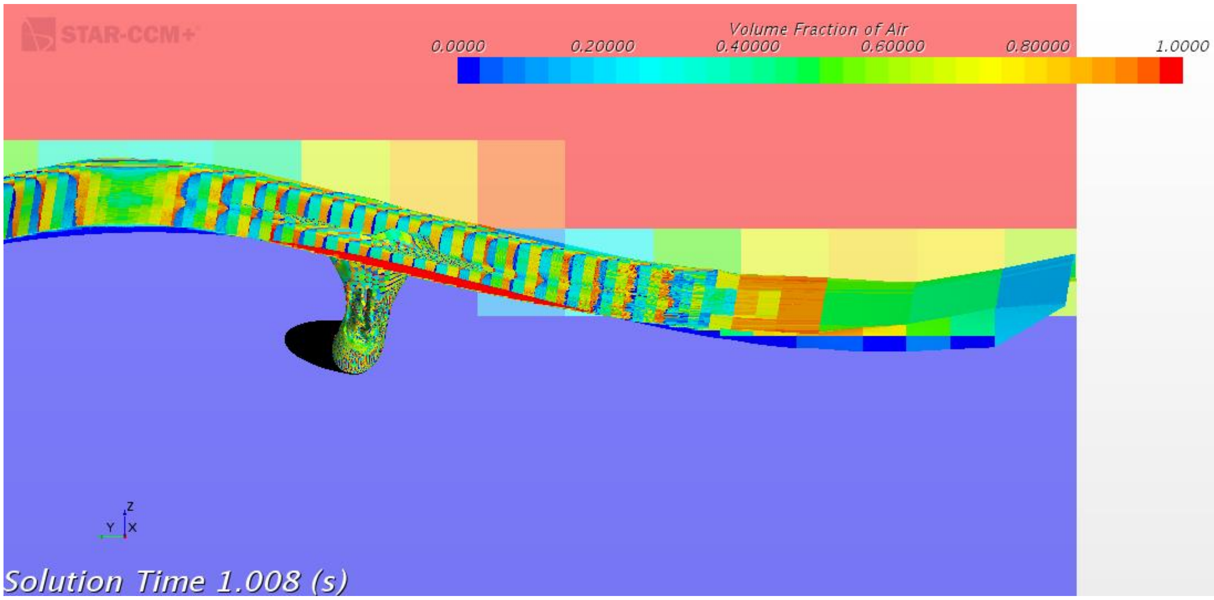

Figure 8.16: The body has been affected by the wave crest, and has started to move in port side direction

8.7.10 Case 10, beam sea, $\frac{\pi}{2}$ radians, wave height 7 m

a)

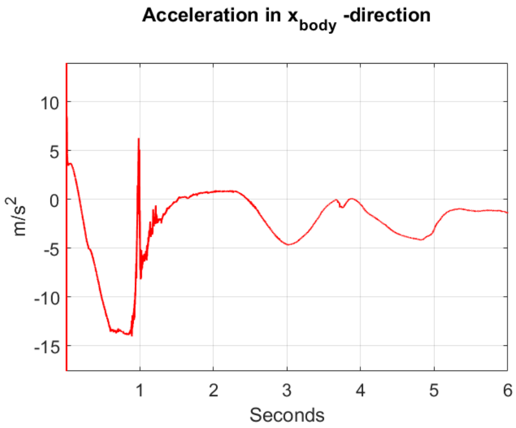

Acceleration in x_{body} -direction

b)

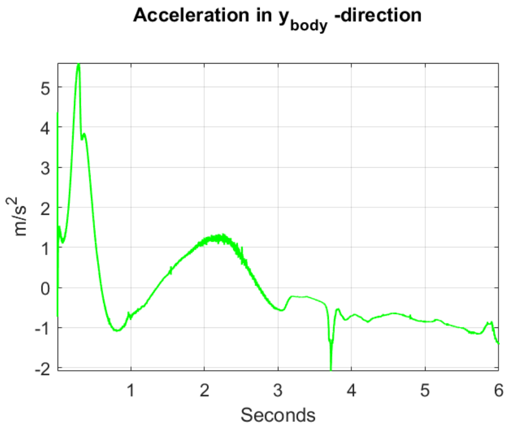

Acceleration in y_{body} -direction

c)

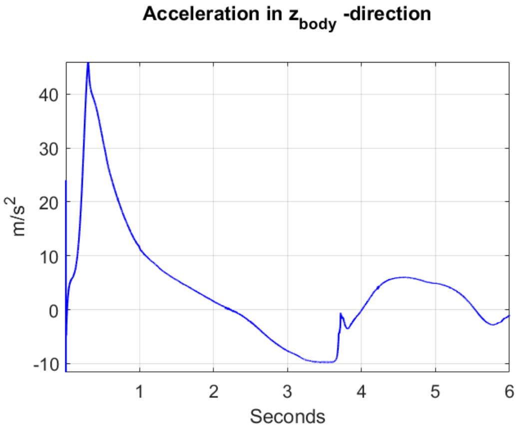

Acceleration in z_{body} -direction

d)

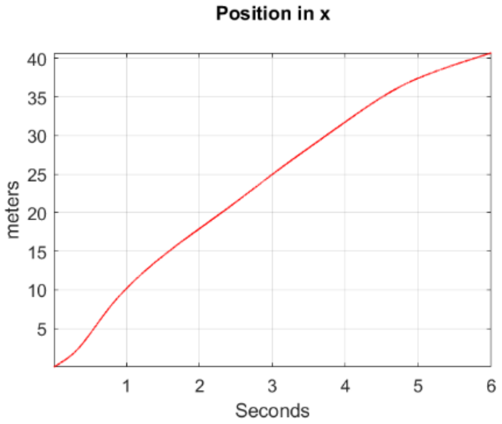

Position in x

e)

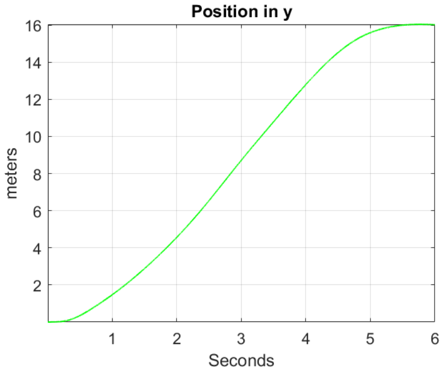

Position in y

f)

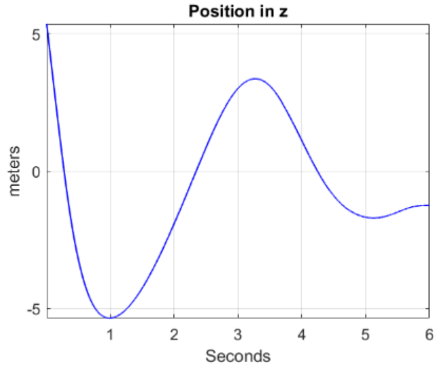

Position in z

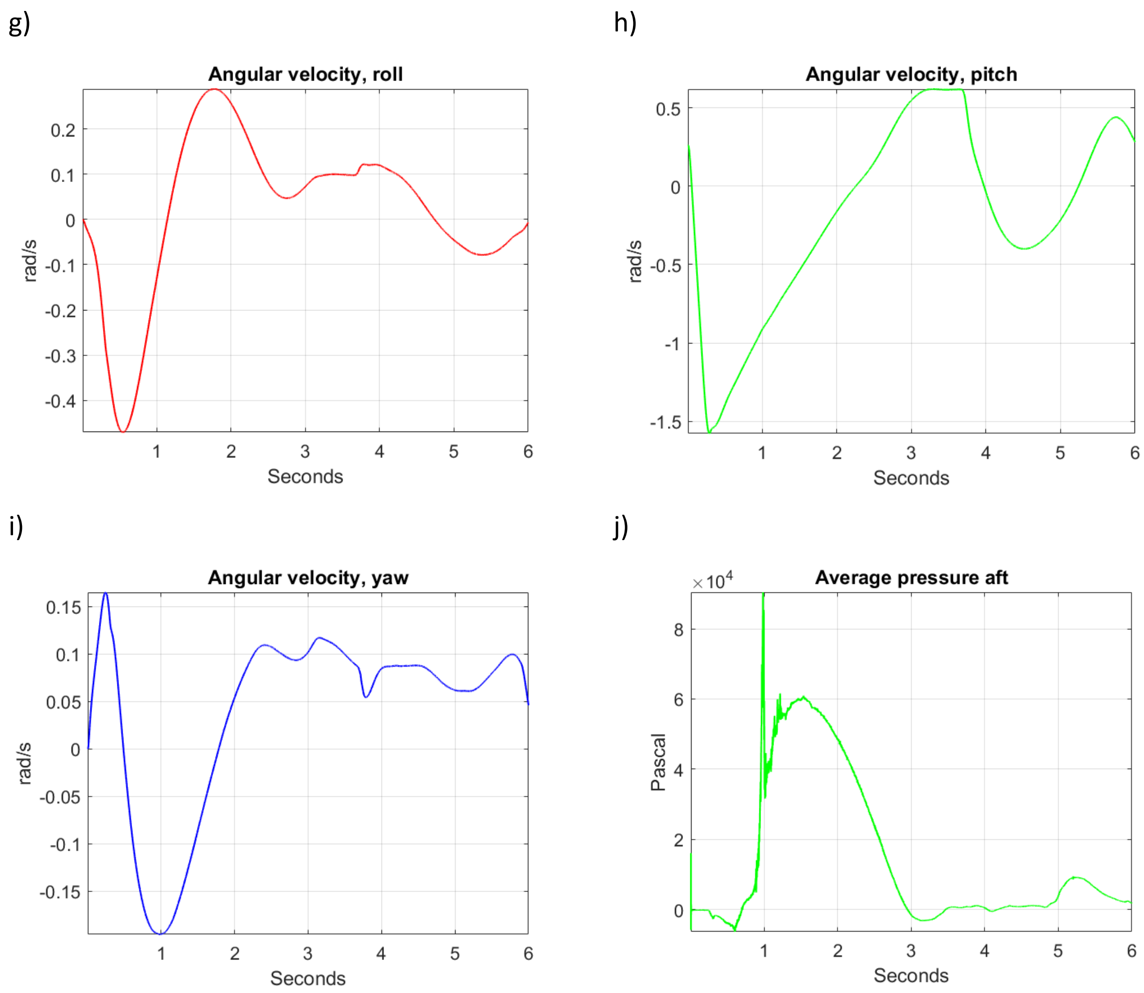

Figure 8.17: Computed time-histories for acceleration, position, angular velocity and average pressure aft, case 10

The body dives into a wave phase where the particle velocity is acting upward, and the body gets a large deacceleration. Since there is none or small lateral motion of the particles in the early water entry phase, there is small effects in yaw and roll. The following phase is the wave crest, the body exits in this phase where the lateral particle velocity is at its maximum. There is a small pop-up height, that results in a small second slamming, apparent at 3.75 s in Figure 8.17 a), b) and c). The body gets a combined rotation from roll pitch and yaw, leading to surge motion towards the wave propagation direction. However, the resulting rotation is relatively slow, resulting in a large translation in both x_{global} and y_{global} direction.

8.7.11 Case 11, beam sea, π radians, wave height 7 m

a)

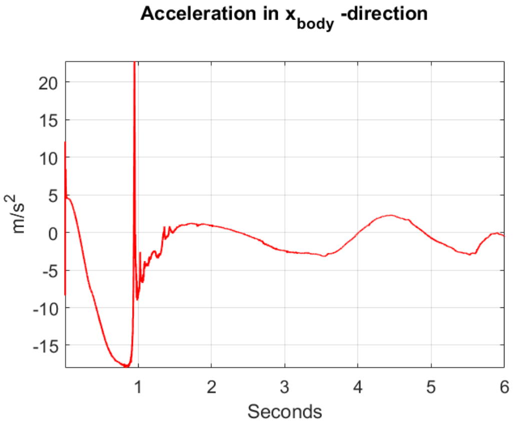

b)

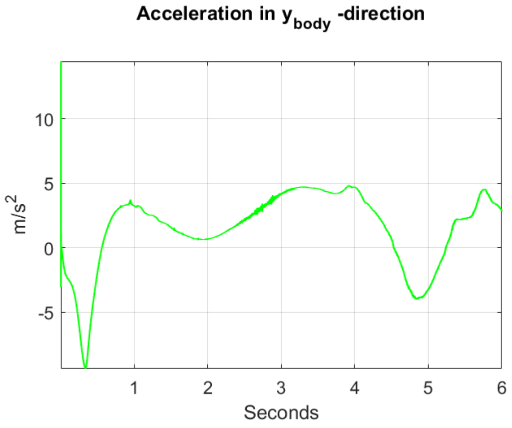

c)

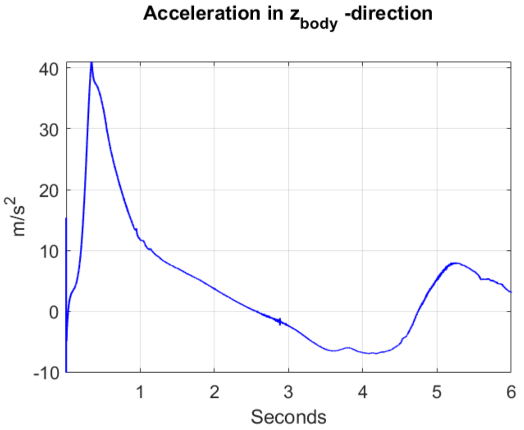

d)

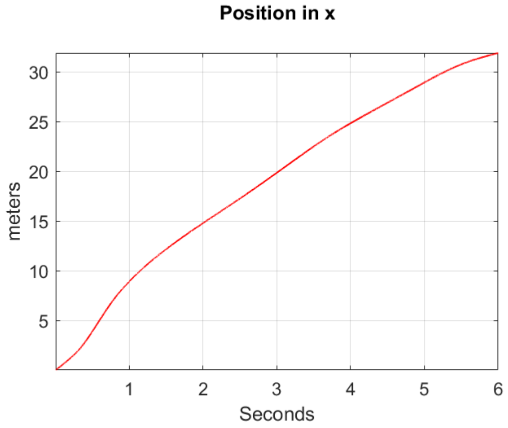

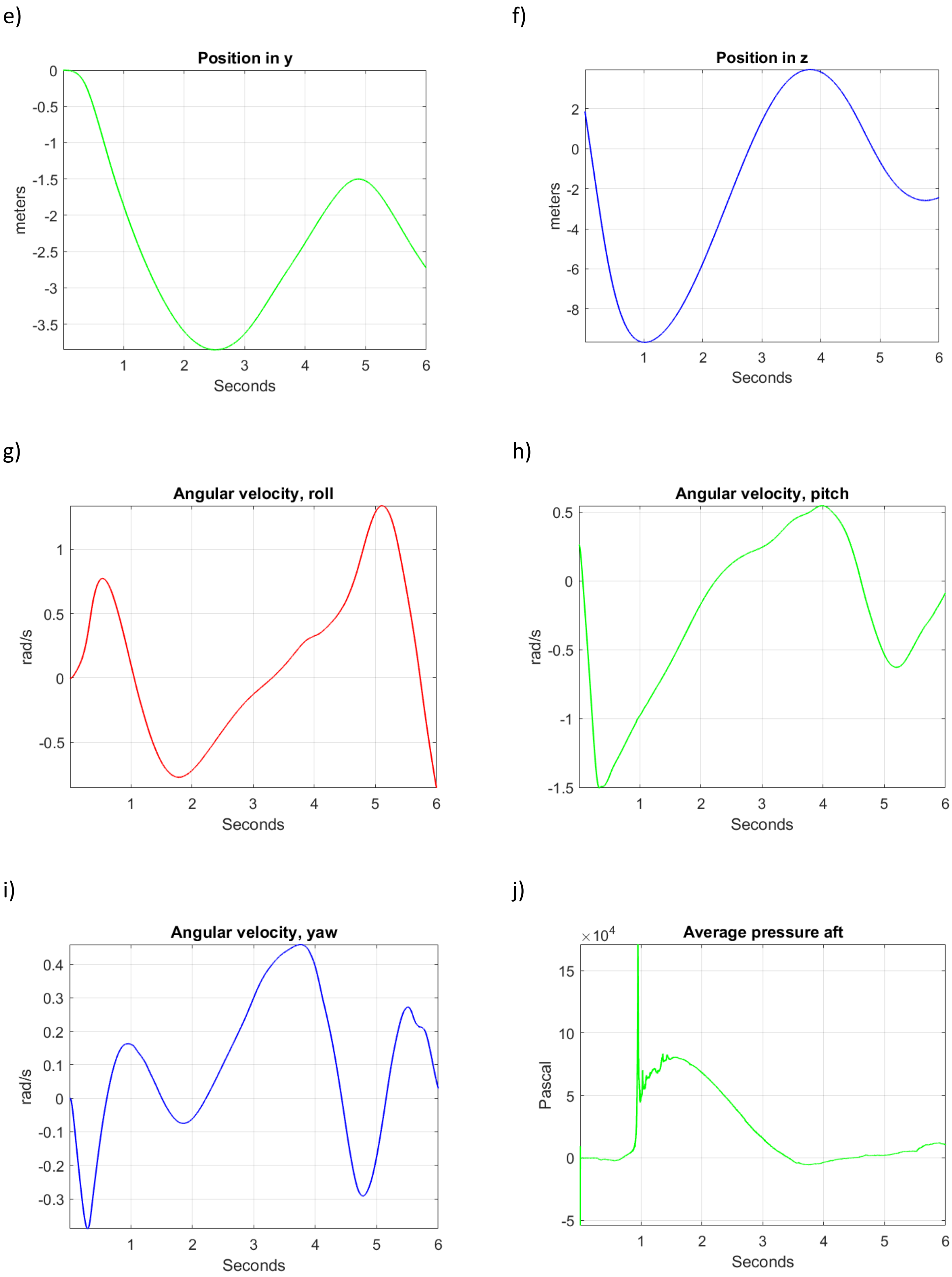

Figure 8.18: Computed time-histories for acceleration, position, angular velocity and average pressure aft, case 11

The body dives into a wave trough where the particle velocity is acting in the opposite direction of the wave propagation. The body gets large negative sway acceleration, positive roll velocity and negative yaw velocity. Like for case 9, but in opposite direction and with some smaller magnitude. The body gets a y_{global} component in surge motion, leading the body out of the $x - z$ plane. The body exits in the wave crest. The penetration of the surface disturbs the linear behaviour of the wave, and the kinetic energy from the wave crest transfers to the body in the wave propagation direction. After some time, the body gets realised from these effects and moves down in the wave trough where it is gets moved in the opposite direction of the wave propagation.

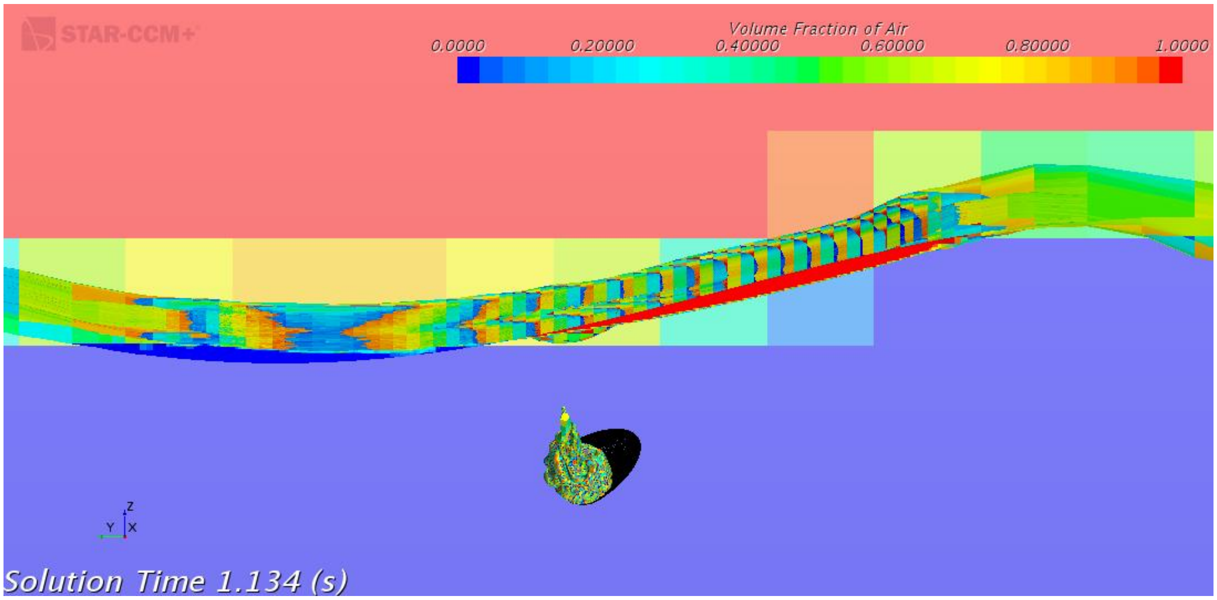

Figure 8.19: The body has been affected by the wave trough, and has started to move in starboard direction

8.7.12 Case 12, beam sea, $\frac{3\pi}{2}$ radians, wave height 7 m

a)

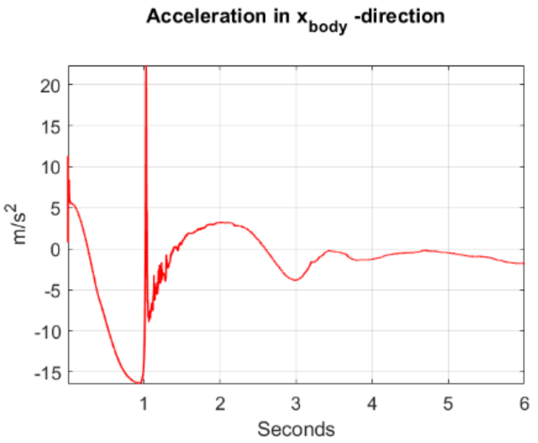

b)

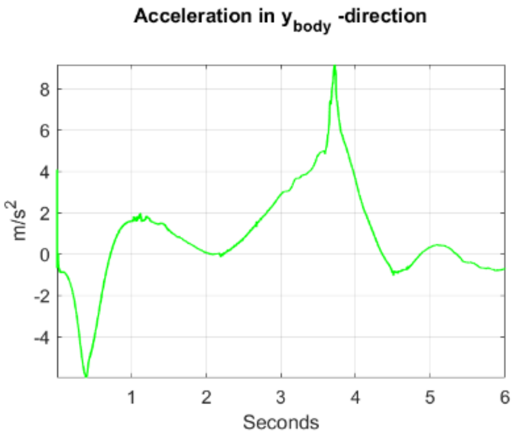

c)

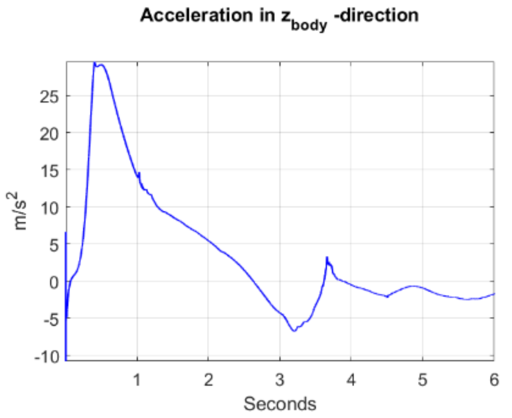

d)

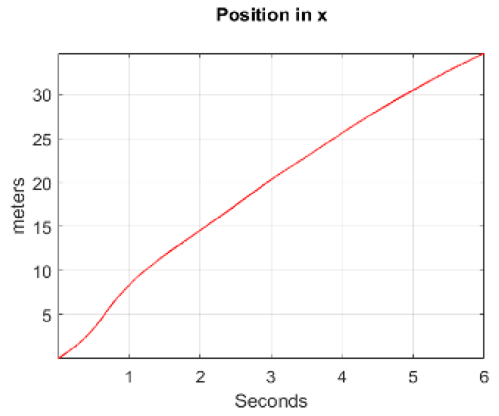

e)

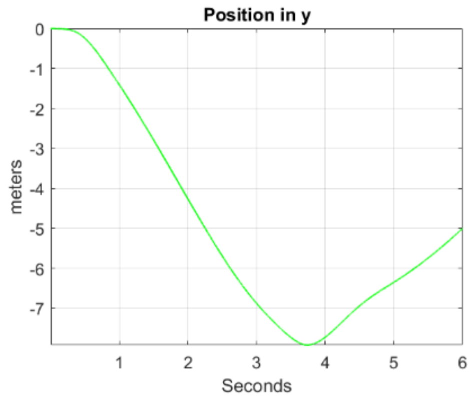

f)

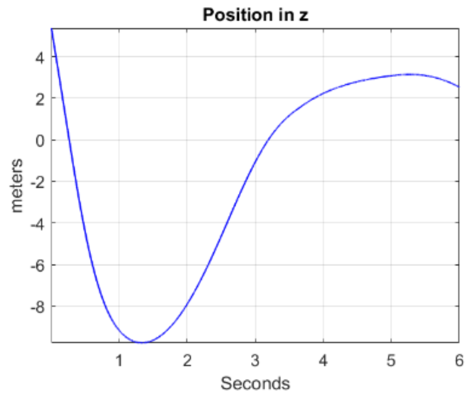

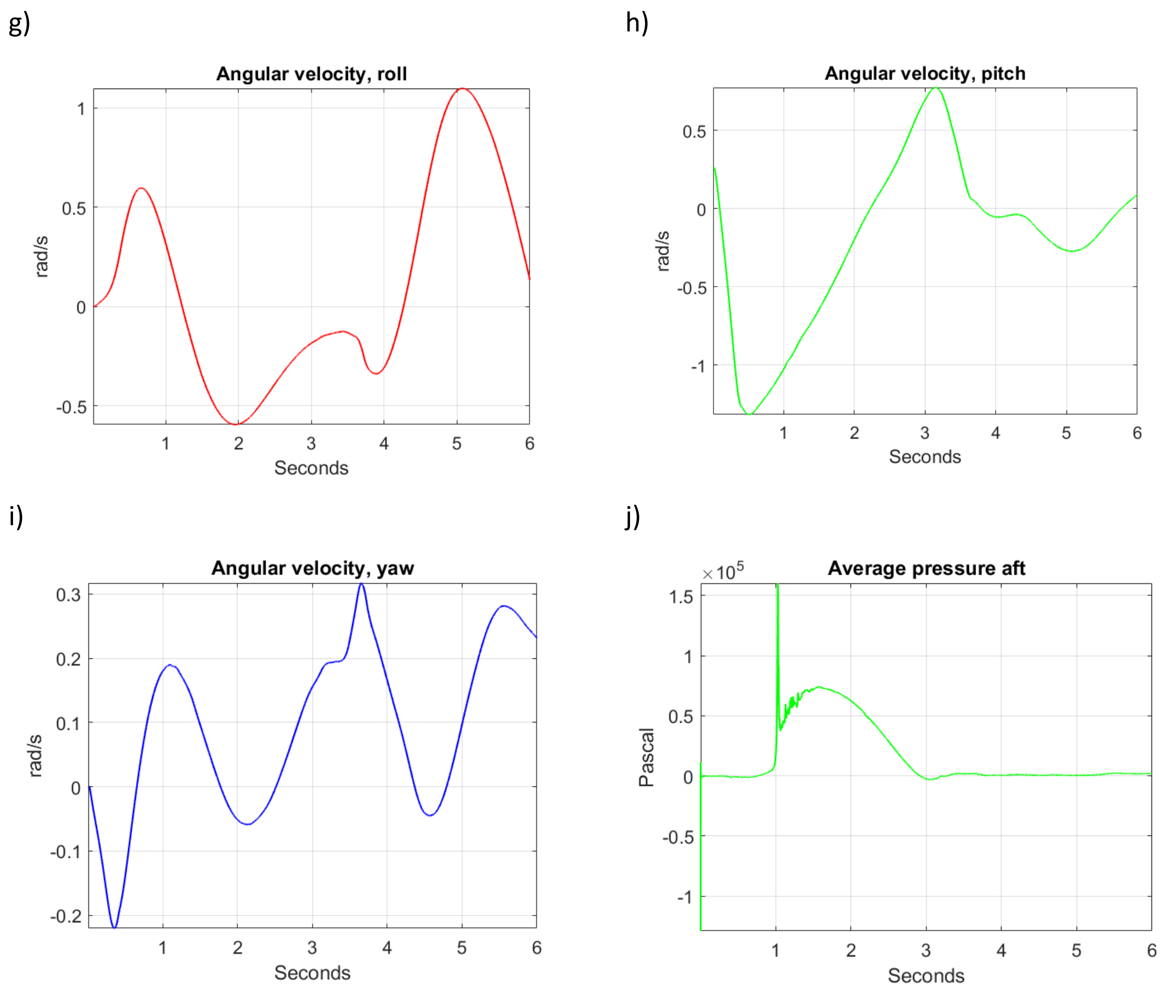

Figure 8.20: Computed time-histories for acceleration, position, angular velocity and average pressure, case 12

The body dives into the $\frac{3\pi}{2}$ phase where the particle velocity is acting downwards, and the body experience relatively small deaccelerations. Then follows a wave trough, as the wave is propagating from star board to port side, hence the translation in sway. Since there is none or small lateral motion of the particles in the water entry phase, there are small effects in yaw and roll. Then the body starts getting affected by the wave trough phase, and the body gets a translation opposite to the wave propagation direction. The body exits in the $\frac{\pi}{2}$ phase where the fluid velocity is acting upwards. The penetration of the surface causes non-linear effects, and at the wave crest the body gets translation in the direction of the wave propagation.

8.7.13 Case 13, following sea, 0 radians, wave height 5 m

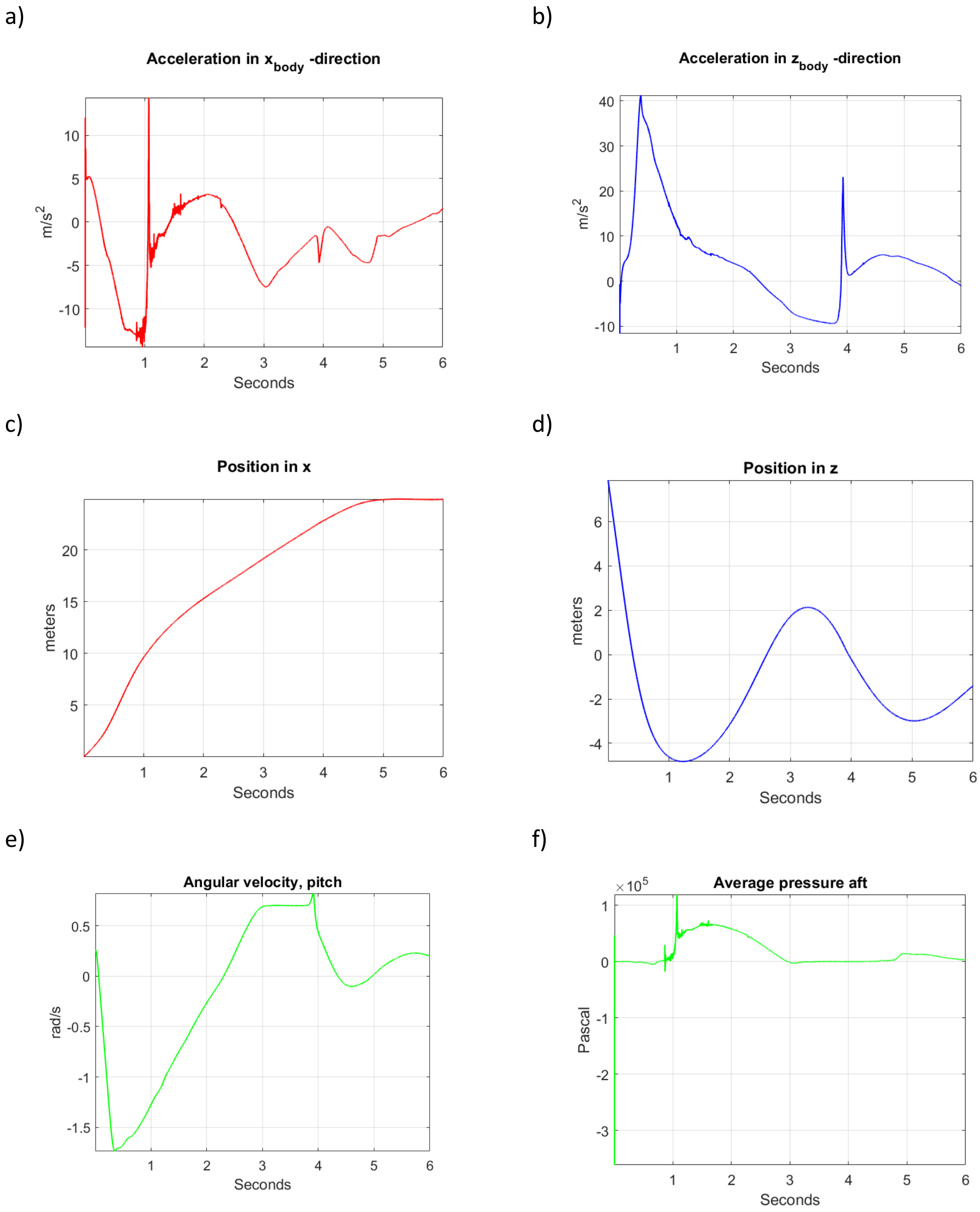

Figure 8.21: Computed time-histories for acceleration, position, angular velocity and average pressure, case 13

This case is to be compared to case 1 and 14, the only parameter that is changed is the wave height. The body dives in the wave crest. The particle velocity is dependent on the wave amplitude, and this leads to smaller horizontal velocities in the wave crest. This shows to have effect, however small, in the counter clockwise pitch velocity and the acceleration peak in the aft part slamming, both these gets reduced with reduced steepness. In cases of diving in a wave crest, the submergence will increase when the wave amplitude is lowered, as the other initial conditions are kept constant. This is due to the initial z_{global} position and the reduced counter clockwise pitch rotation. The second slamming has approximately the same contribution for Case 1 and Case 13, as their motions are quite similar after the water entry phase.

8.7.14 Case 14, following sea, 0 radians, wave height 3 m

a)

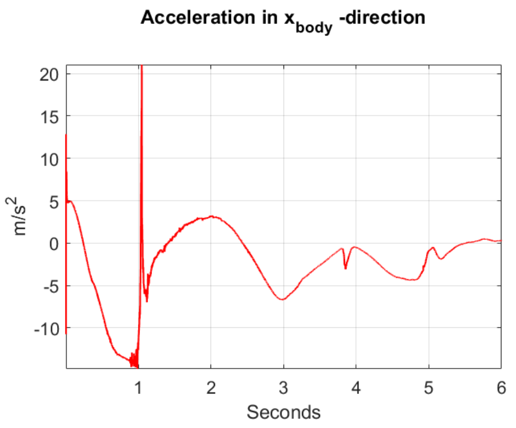

b)

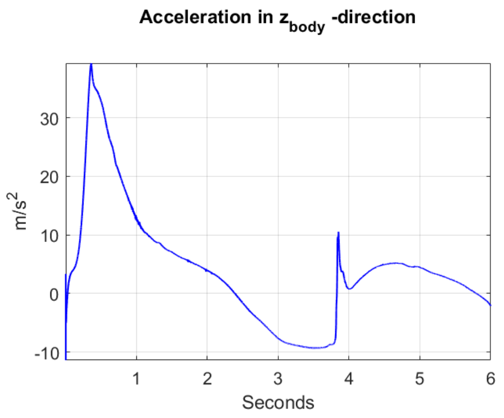

c)

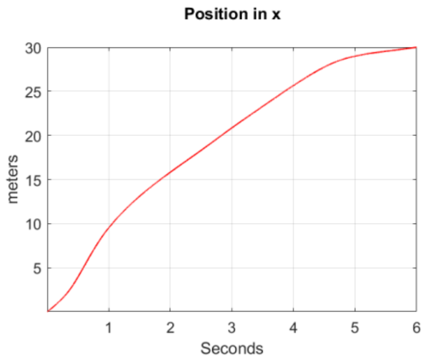

d)

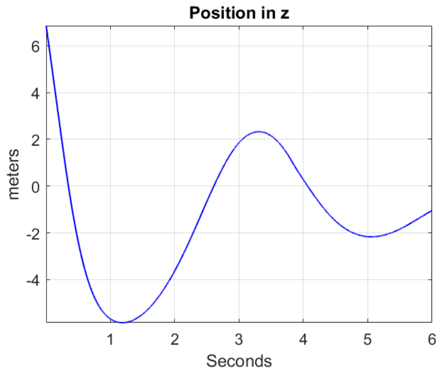

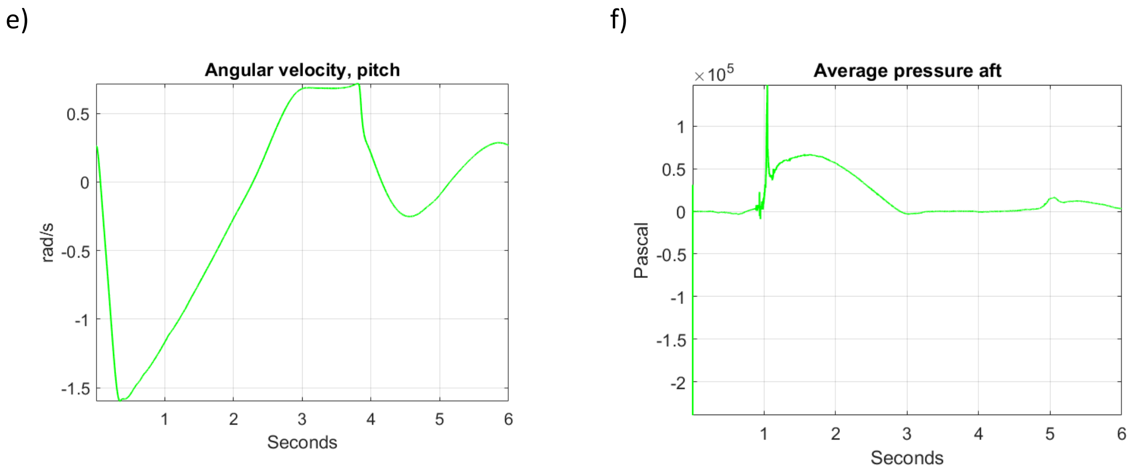

Figure 8.22: Computed time-histories for acceleration, position, angular velocity and average pressure, case 14

This case is to be compared with case 1 and 13, the only parameter that is changed is the wave height. The wave amplitude is further reduced from case 13. This further reduces the counter clockwise pitch velocity and the z_{body} acceleration in the aft part slamming. It gets a deeper submergence for reasons mention in 8.7.13. However, the pressure is measured on the aft part which has a larger submergence point for the cases with larger wave height, these cases will also have a larger dynamic pressure at 1.65 s, as the aft is located closer to the wave crest and the dynamic pressure is proportional to the wave amplitude. Hence, case 14 gets the lowest maximum average pressure aft at this point. The relative small counter clockwise pitch velocity leads to a larger surge motion in the x_{global} direction at water exit, which leads to smaller second slamming forces and a longer sail away distance.

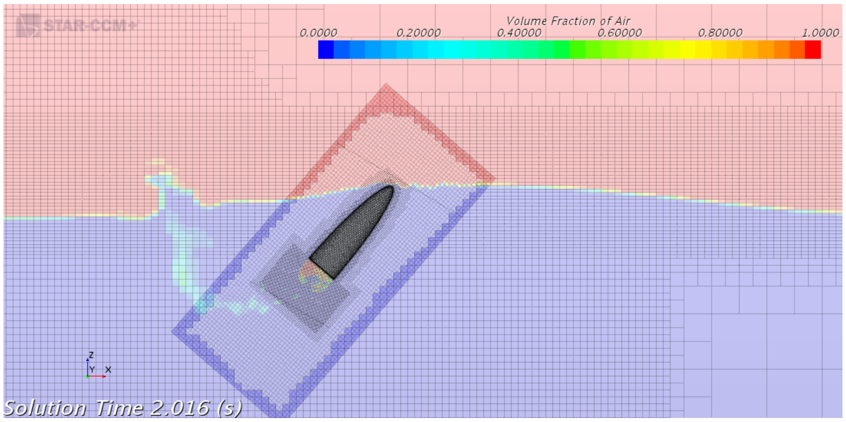

Figure 8.23: The body exits with a smaller water exit angle than for Case 1, this is clearly visual by comparing with Figure 8.4

8.7.15 Case 15, head sea, π radians, wave height 5 m

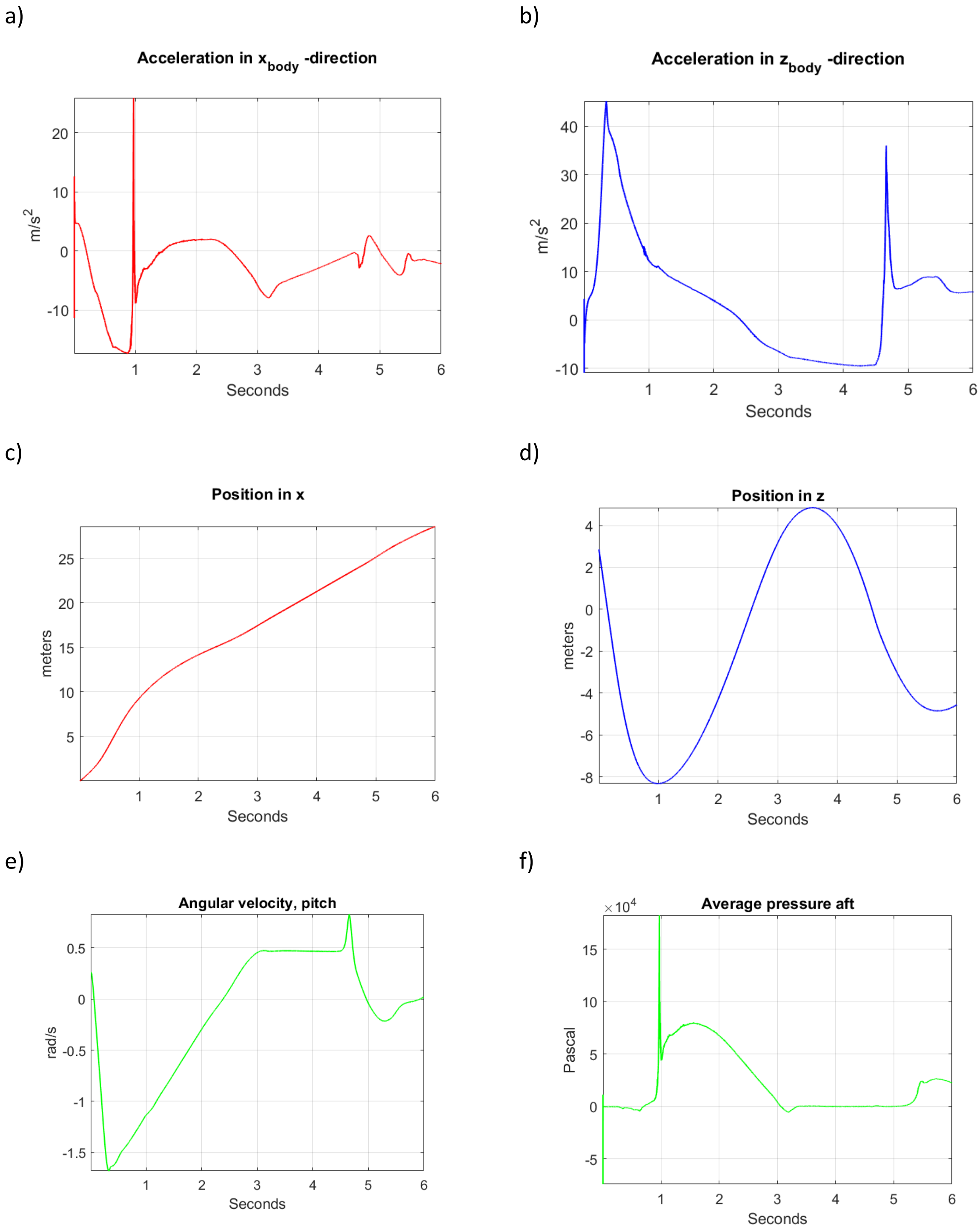

Figure 8.24: Computed time-histories for acceleration, position, angular velocity and average pressure, case 15

This case is to be compared with case 7 and 16, the only parameter that is changed is the wave height. The body dives into a wave trough, with smaller horizontal velocities than for case 7. This manifests in the counter clockwise pitch velocity and smaller slamming on the aft part in the water entry phase, though the difference is relatively small. Case 14 starts the water entry one meter above case 1. The difference in maximum submergence is relatively small, as Case 14 gets a smaller counter clockwise pitch contribution in the water entry phase. The second slamming is larger than for case 7. This is due the re-entering water entry angle is close to zero, which is a critical angle for this geometry, large changes in added mass.

8.7.16 Case 16, head sea, π radians, wave height 3 m

a)

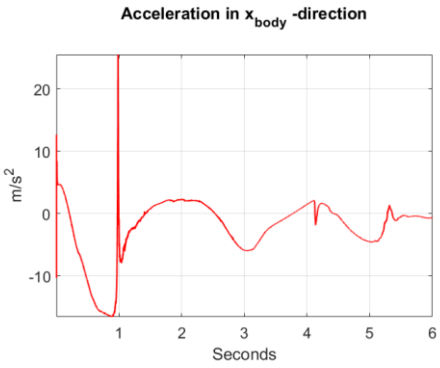

b)

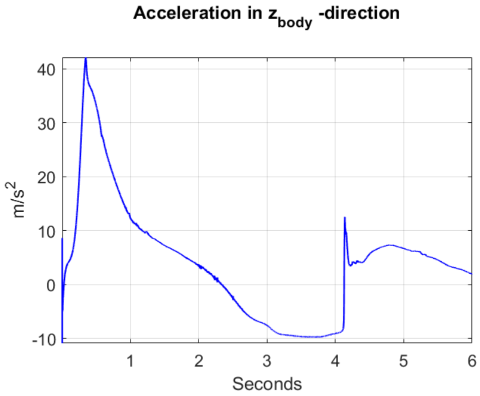

c)

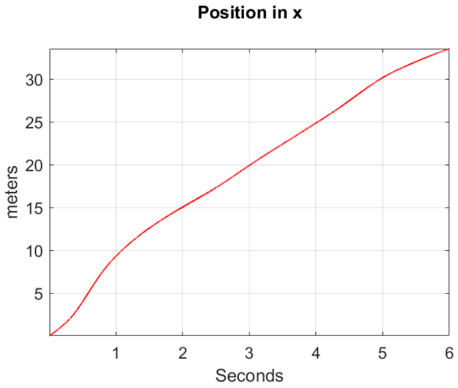

d)

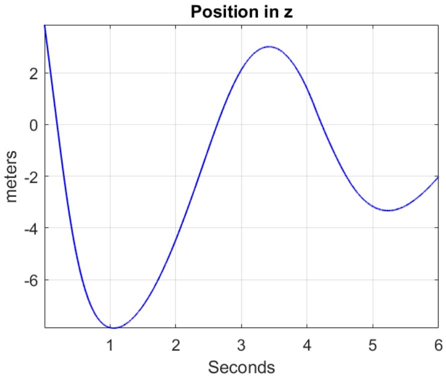

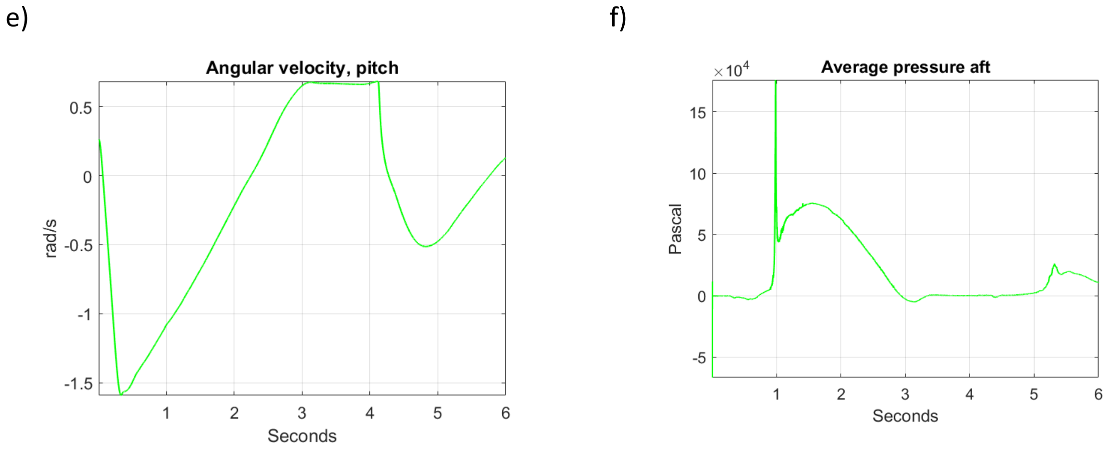

Figure 8.25: Computed time-histories for acceleration, position, angular velocity and average pressure, case 16

This case is to be compared with case 7 and 15, the only parameter that is changed is the wave height. The water entry effects get further reduced with the smaller wave height, so does the second slamming acceleration in z_{body}. The body still exits a little behind the wave crest, but the effective pop-up height gets decreased due to the decreased difference between wave crest and wave trough. Hence a reduced re-entering velocity. However, the body gets a large change in pitch at second impact, seen at 4.1 s, in Figure 8.25 e). This leads to large accelerations in the same direction as the z_{body} in the fore part.

8.7.17 Case 17, beam sea $\frac{\pi}{2}$ radians, wave height 5 m

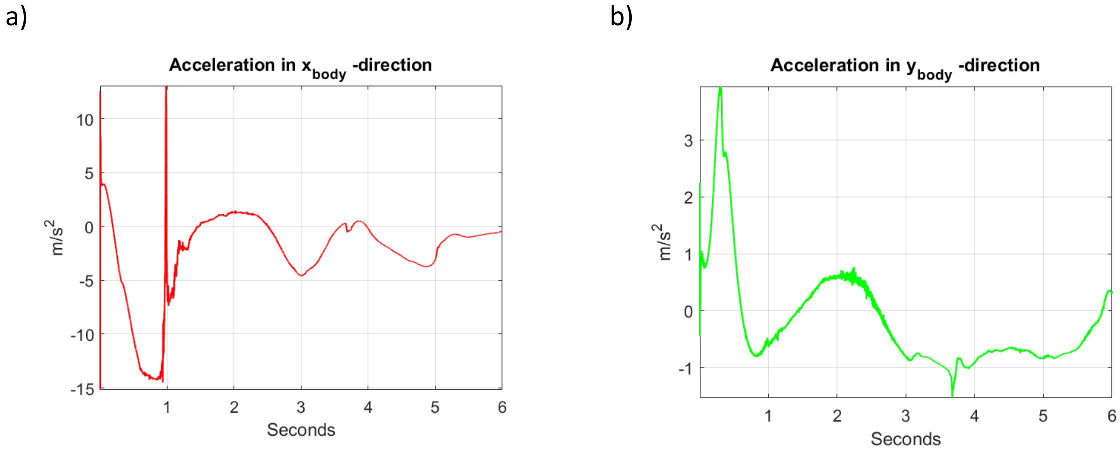

c)

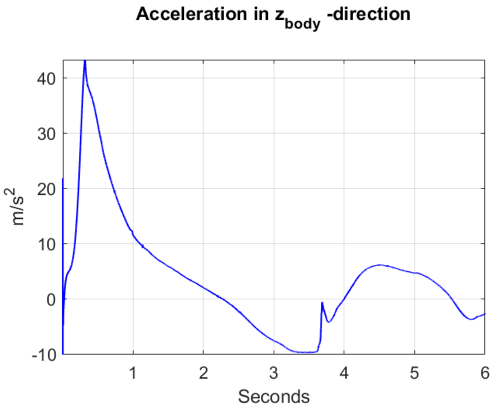
Acceleration in z_{body} -direction
m/s^2
40
30
20
10
0
-10
1
2
3
4
5
6
Seconds

d)

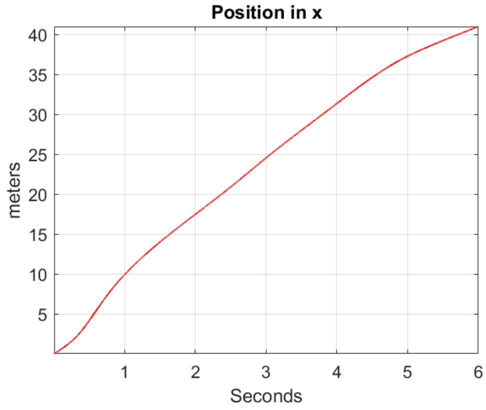
Position in x
meters
40
35
30
25
20
15
10
5
1
2
3
4
5
6
Seconds

e)

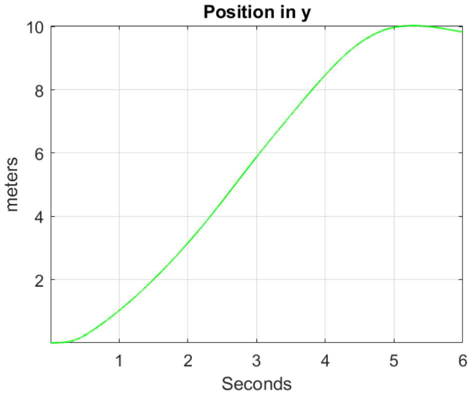
Position in y
meters
10
8
6
4
2
1
2
3
4
5
6
Seconds

f)

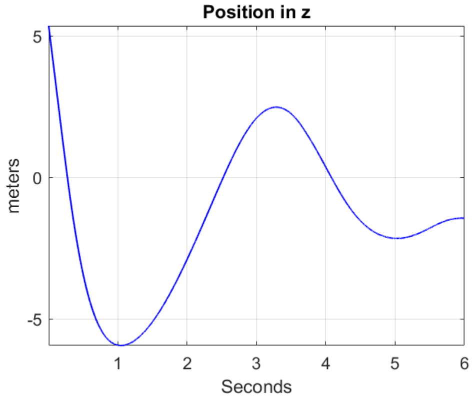
Position in z
meters
5
0
-5
1
2
3
4
5
6
Seconds

g)

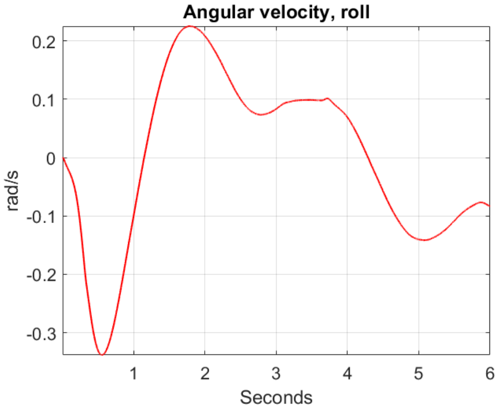
Angular velocity, roll
rad/s
0.2
0.1
0
-0.1
-0.2
-0.3
1
2
3
4
5
6
Seconds

h)

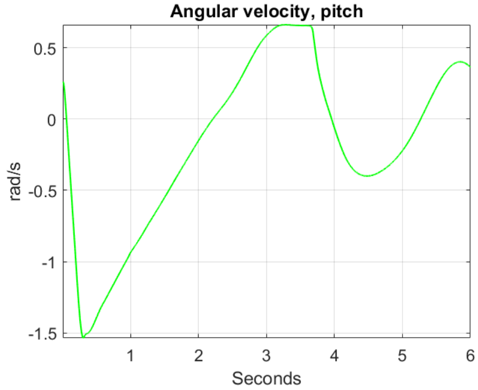
Angular velocity, pitch
rad/s
0.5
0
-0.5
-1
-1.5
1
2
3
4
5
6
Seconds

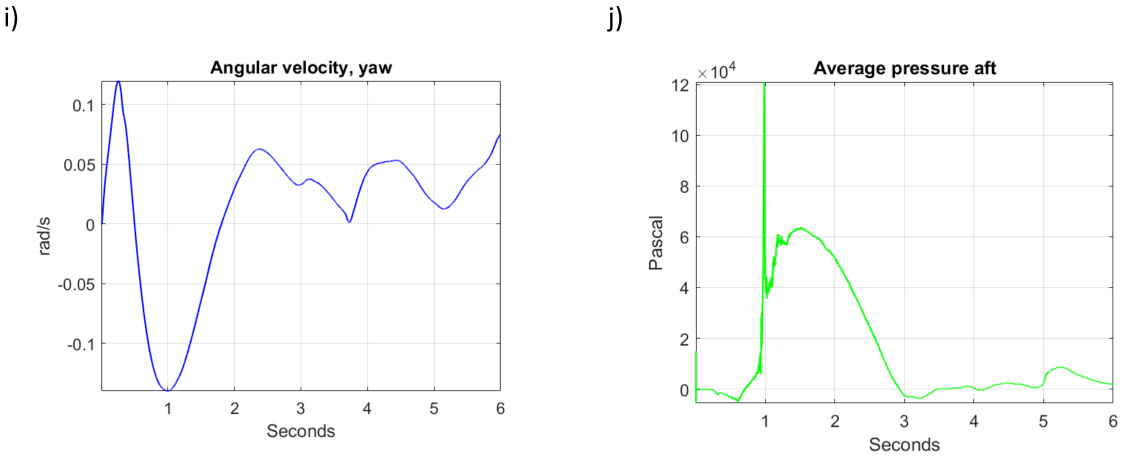

Figure 8.26: Computed time-histories for acceleration, position, angular velocity and average pressure, case 17

This case is to be compared with case 10 and 18, the only parameter that is changed is the wave height. The fluid velocity is acting upwards at the point of impact. This fluid velocity is reduced by reducing the wave amplitude. The largest differences are in the sway acceleration and in the y_{body} position. Both decreases as the particle velocity in the next phase, the wave crest, is lower than for case 10.

8.7.18 Case 18, beam sea $\frac{\pi}{2}$ radians, wave height 3 m

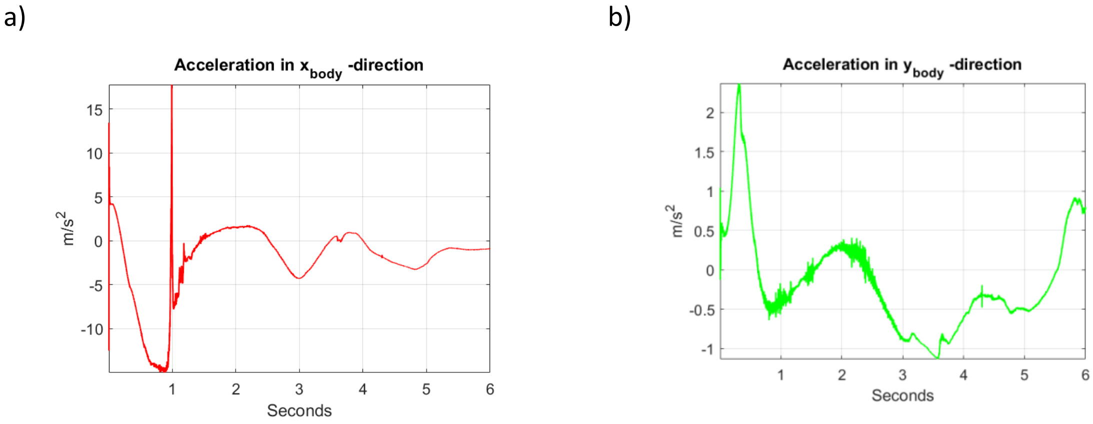

c)

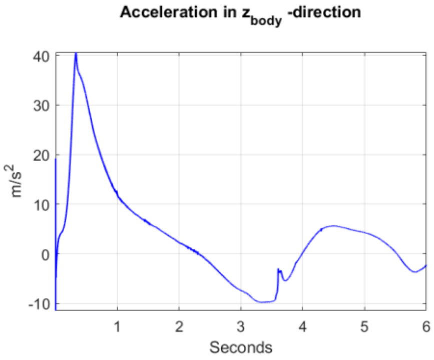
Acceleration in z_{body} -direction
m/s^2
40
30
20
10
0
-10
1
2
3
4
5
6
Seconds

d)

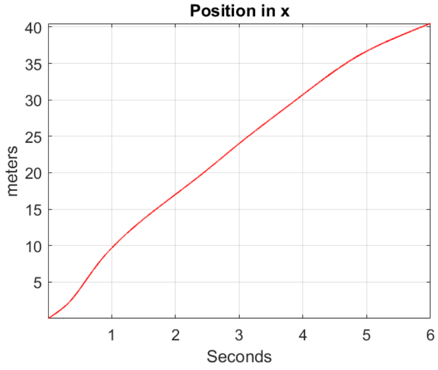
Position in x
meters
40
35
30
25
20
15
10
5
1
2
3
4
5
6
Seconds

e)

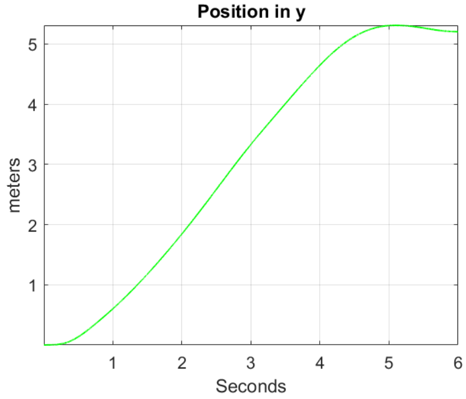
Position in y
meters
5
4
3
2
1
1
2
3
4
5
6
Seconds

f)

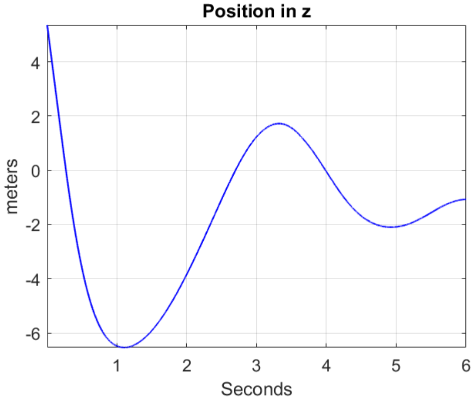
Position in z
meters
4
2
0
-2
-4
-6
1
2
3
4
5
6
Seconds

g)

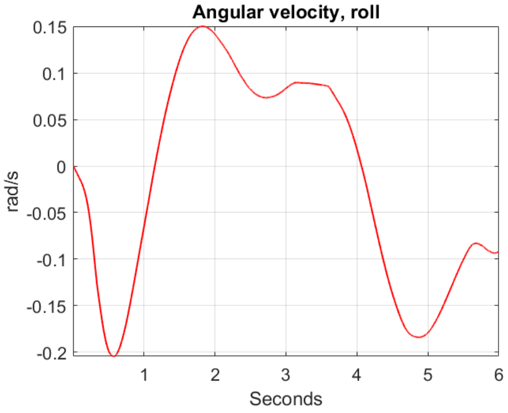
Angular velocity, roll
rad/s
0.15
0.1
0.05
0
-0.05
-0.1
-0.15
-0.2
1
2
3
4
5
6
Seconds

h)

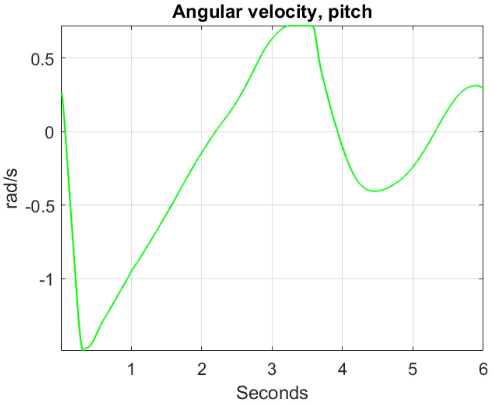
Angular velocity, pitch
rad/s
0.5
0
-0.5
-1
1
2
3
4
5
6
Seconds

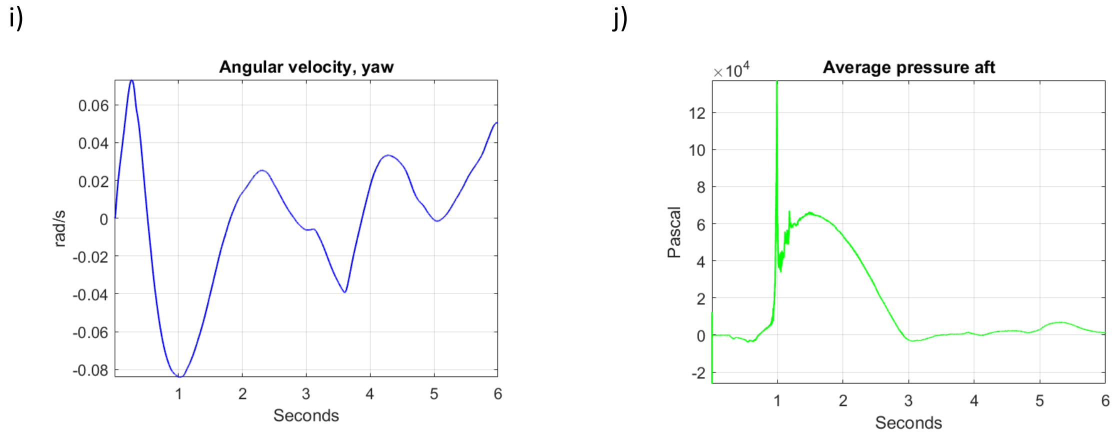

Figure 8.27: Computed time-histories for acceleration, position, angular velocity and average pressure, case 18

This case is to be compared with case 10 and 17, the only parameter that is changed is the wave height. All the effects are reduced from case 10 and 17, except for the maximum submergence and the average pressure aft. They have increased as the relative velocity between the body and the fluid in the downward direction is reduced. The deep submergence leads to larger hydrostatic pressure. However, the difference is relatively small, as the dynamic pressure are larger under a wave crest with higher amplitude.

8.7.19 Summarising the results

A list of distinctive parameter points, their values and for which case number they occur are presented below. Each table summarize the results from the different wave headings.

Following-sea waves

Description of distinctive parameter points	Value	Phase (radians) / Case number
Largest acceleration in $\boldsymbol{x_{body}}$, before air cavity closure	-19.8 m/s^2	$\frac{3\pi}{2}$ / Case4
Largest acceleration in $\boldsymbol{z_{body}}$	46.8 m/s^2	$\frac{\pi}{2}$ / Case2
Largest pitch velocity	-1.89 rad/s at 0.3 s	0 / Case1

Largest acceleration-peak in $\boldsymbol{x_{body}}$ at air cavity closure	33.4 m/s^2	π / Case3
Largest average pressure aft, after air cavity closure.	87800 Pa	$\frac{3\pi}{2}$ / Case4
Largest second slamming acceleration peak in $\boldsymbol{z_{body}}$	22.4 m/s^2	0 / Case1
Longest sailing distance in global x-direction after 6 s.	67.65 m	$\frac{\pi}{2}$ / Case2
Shortest sailing distance in global x-direction after 6 s.	19.5 m	0 / Case1

Table 8.2: Distinctive values for simulations in following-sea waves

Head waves

Description of distinctive parameter points	Value	Phase (radians)/Case number
Largest acceleration in $\boldsymbol{x_{body}}$, before air cavity closure	-18.0 m/s^2	π / Case 7
Largest acceleration in $\boldsymbol{z_{body}}$	48.0 m/s^2	π / Case 7
Largest acceleration-peak at air cavity closure in $\boldsymbol{x_{body}}$	35.4 m/s	$\frac{3\pi}{2}$ / Case 8
Largest pitch velocity	-1.75 rad/s, at 0.3 s	π / Case 7
Largest average pressure aft, after air cavity closure.	85100 Pa	π / Case 7
Largest second slamming acceleration peak in $\boldsymbol{z_{body}}$	37.4 m/s^2	π / Case 15
Longest sailing distance in global x-direction after 6 s.	33.4 m	π / Case 16
Shortest sailing distance in global x-direction after 6 s.	22.9 m	π / Case 7

Table 8.3: Distinctive values for simulations in head-sea waves

Beam waves

Description of distinctive parameter points	Value	Phase (radians) / Case number
Largest acceleration in $\boldsymbol{x_{body}}$, before air cavity closure	18.0 m/s^2	π / Case11
Largest acceleration in $\boldsymbol{y_{body}}$, before air cavity closure	13.1 m/s^2	0 / Case9
Largest acceleration in $\boldsymbol{z_{body}}$, before air cavity closure	45.8 m/s^2	$\frac{\pi}{2}$ / Case10
Largest roll velocity	-1.6 rad/s, at 4.5 s	0 / Case9
Largest pitch velocity	-1.6 rad/s, at 0.3 s	$\frac{\pi}{2}$ / Case10
Largest yaw velocity	0.6 rad/s, at 0.3 s	0 / Case9
Largest acceleration-peak in $\boldsymbol{x_{body}}$ at air cavity closure	22.7 m/s^2	π / Case11
Largest average surface pressure after air cavity closure.	80530 Pa	π / Case11
Largest second slamming acceleration peak in $\boldsymbol{z_{body}}$	3.3 m/s^2	0 / Case12
Longest sailing distance in global x-direction after 6 s.	40.6 m	$\frac{\pi}{2}$ / Case10
Shortest sailing distance in global x-direction after 6 s.	22.2 m	0 / Case9
Longest translation in y-direction	16.0 m	$\frac{\pi}{2}$ / Case10

Table 8.4: Distinctive values for simulations in beam-sea waves

The distinctive values are found for the different headings, they seem to be dependent on which wave phase the body dives into and the direction of the particle velocity, hence the wave heading. The air cavity closure acceleration peak in x_{body} is dependent on the pressure. This consist of the hydrostatical pressure, which increases with increasing water depth, and the hydrodynamic pressure which is dependent on the wave amplitude and the wave phase. So is the maximum average pressure on the aft part after air cavity closure. The phases that gives the largest submergences are the phases π and $\frac{3\pi}{2}$, where the fluid velocity directions are horizontal and downward, respectively. The wave phase π is the wave trough, hence the large submergence is natural, as the initial position already is lowered. The maximum acceleration in z_{body} occurs for the wave phase $\frac{\pi}{2}$ for two of the different headings. This is where the particle velocity acting upwards which leads to high relative fluid-body velocities and large slamming on the aft part. Also for head sea, the phase $\frac{\pi}{2}$ gives large acceleration in z_{body}, but diving in a wave trough gives larger counter clockwise pitch velocity, and a larger slamming force on the aft part.

There is small difference in air cavity closure time, but the acceleration peak value in x_{body} shows great differences. However, the magnitude of the peak is not realistic as the air is modelled as incompressible, though it may give indication of which cases that can accept large cavity closure accelerations peaks when the air is modelled as compressible.

Diving in beam-sea in a wave crest or a trough, do not create large differences in z_{body} and x_{body} accelerations. But it leads to accelerations in y_{body} which do not occur for following sea and head sea. The body gets a translation in the global y-direction, and it gets dependent on a larger area free for other vessels or constructions.

The second slamming is dependent on the parameters in the water exit, where the wave form and wave phase are of importance. If the body exits in the upper part of the wave with high velocity, the second slamming at the re-entering can be severe.

8.8 CAR-value investigation

In order to see how the different wave heading and phases are affecting the passengers, a calculation of CAR-values have been performed. The body fixed accelerations and the angular accelerations are filtered by a 20 Hz low pass Butterworth fourth order filter. An example of a filtration result of the body-fixed accelerations and angular accelerations are showed in Figure 8.28.

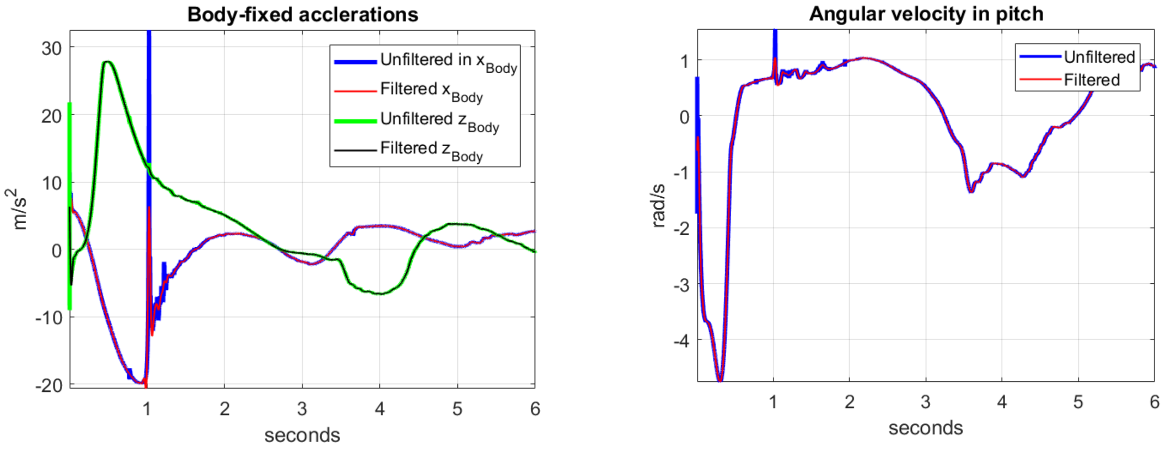

Figure 8.28: Superimposed filtered and unfiltered body-fixed accelerations and angular acceleration for case 1.

Figure 8.28 shows that the short time duration peaks get filtrated. The largest peaks are filtrated in the time interval of the air cavity collapsing. The air is modelled as incompressible and creates unrealistic large peaks, and thus the purpose of the filtration. The accelerations are calculated for two different passenger-positions. These positions are at 10 % and 90 % of the total length of the body, that is in aft part and fore part, respectively. The origin of the seat coordinate system in Figure 2.10 is placed along the x_{body} axis, where the centre of gravity is the origin. Shown in Figure 8.29.

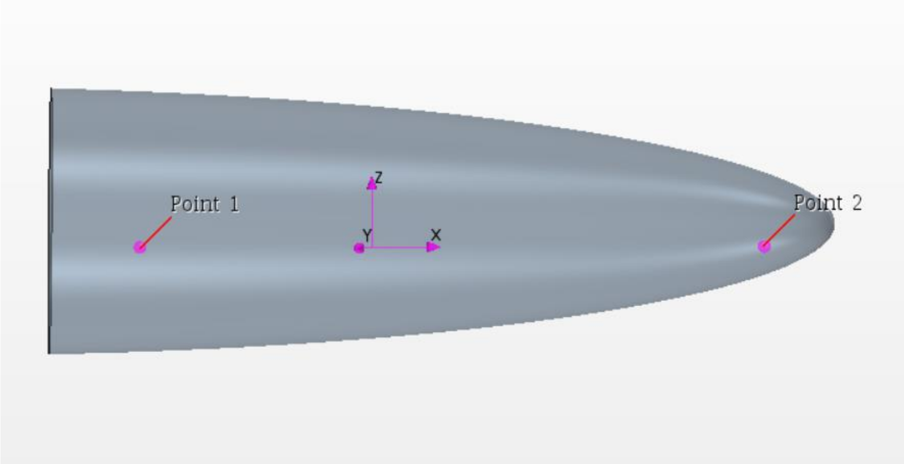

Figure 8.29: The body-fixed coordinate system and the two measured positions

The passengers are locking toward the stern, so that they will accelerate into the back of the seat as the body gets deaccelerated in the water entry and in the early submerged phase. There are none y- or z-arms in the position of the chosen seat-origin, and the calculation of the accelerations that will be inserted in equation [19] are the following:

$$a_x = \ddot{\eta}_1 \tag{53}$$

$$a_y = \ddot{\eta}_2 + \ddot{\eta}_6 * x \tag{54}$$

$$a_z = \ddot{\eta}_3 - \ddot{\eta}_5 * x \tag{55}$$

- $\ddot{\eta}_1$, $\ddot{\eta}_2$ and $\ddot{\eta}_3$ are the filtrated body-fixed acceleration in x, y and z, respectively.
- $\ddot{\eta}_5$ and $\ddot{\eta}_6$ are the filtrated angular accelerations in pitch and yaw, respectively.
- x is the position from centre of gravity to the position of the seat-origin. These are -2.75 m for Point 1 and 5.25 m for Point 2.

The acceleration and angular acceleration values are obtained by Star CCM+ and then filtrated in MATLAB R2017a for further calculations. The CAR values for the different cases are presented in Figure 8.33 to Figure 8.41. The CAR_2 formula has been applied for the calculations, as the passengers will experience into seat accelerations in the water entry phase. In the later phases, where positive x_{body} accelerations will occur, this will be a conservative approach, as it will give higher values than for CAR_1.

Case 1

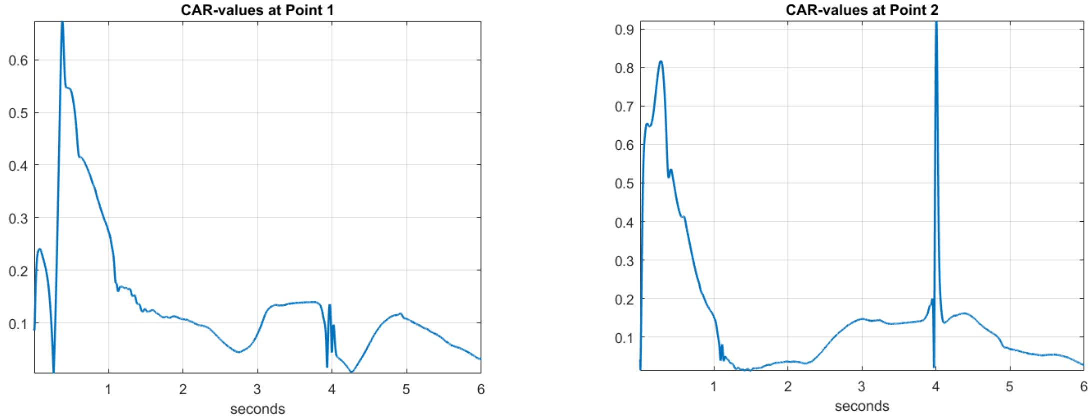

Figure 8.30: Computed time-histories for CAR- values, case 1

Case 2

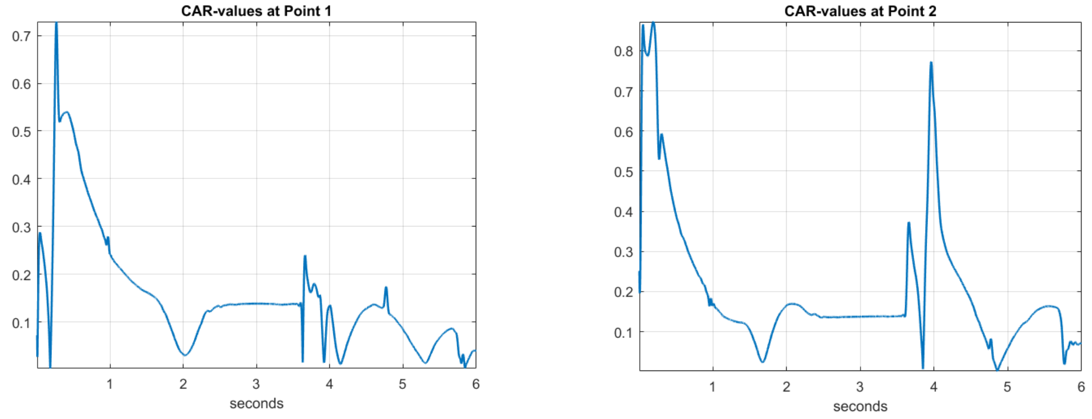

Figure 8.31: Computed time-histories for CAR- values, case 2

Case 3

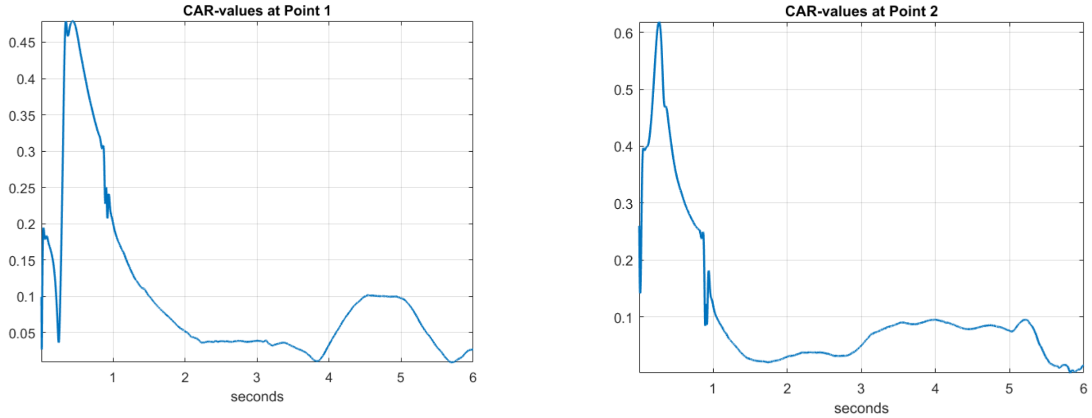

Figure 8.32: Computed time-histories for CAR- values, case 3

Case 4

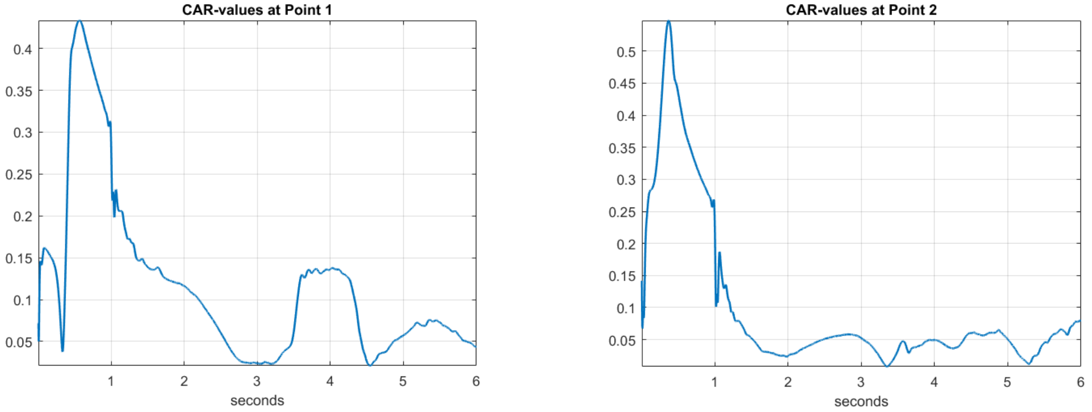

Figure 8.33: Computed time-histories for CAR- values, case 4

Case 5

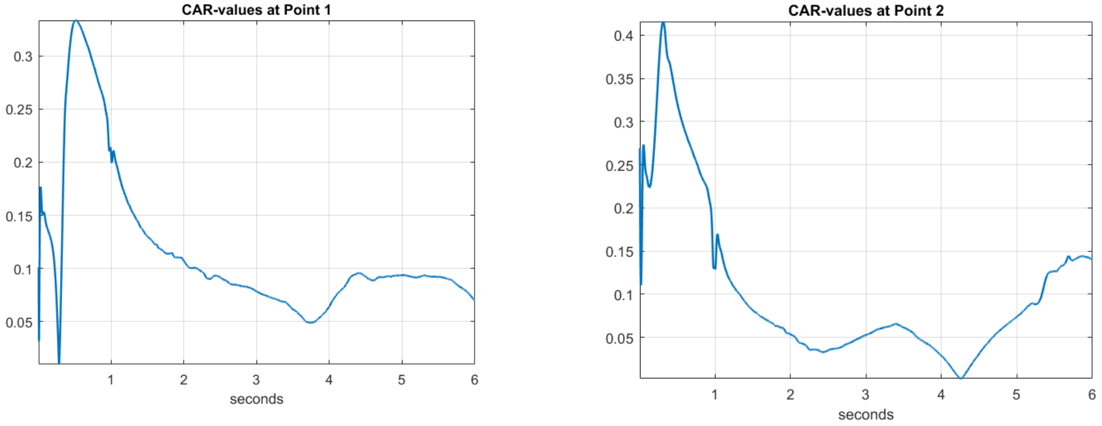

Figure 8.34: Computed time-histories for CAR- values, case 5

Case 6

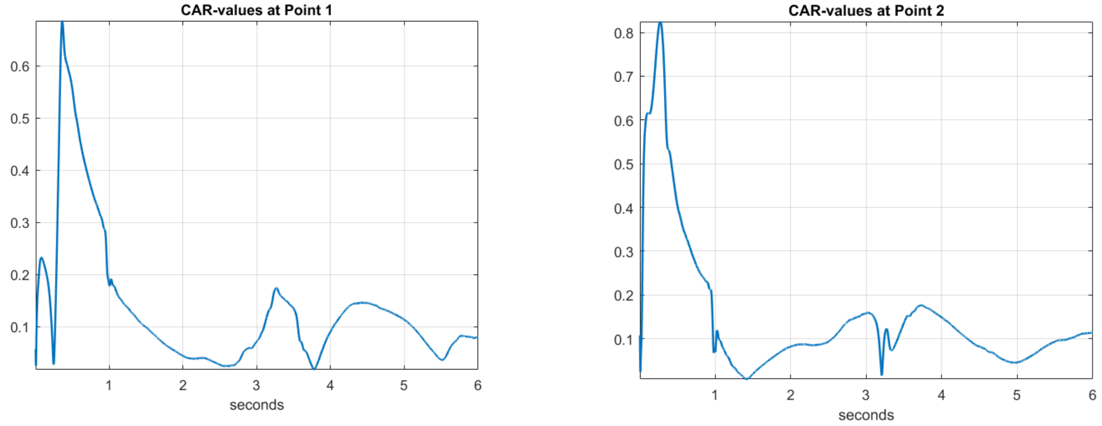

Figure 8.35: Computed time-histories for CAR- values, case 6

Case 7

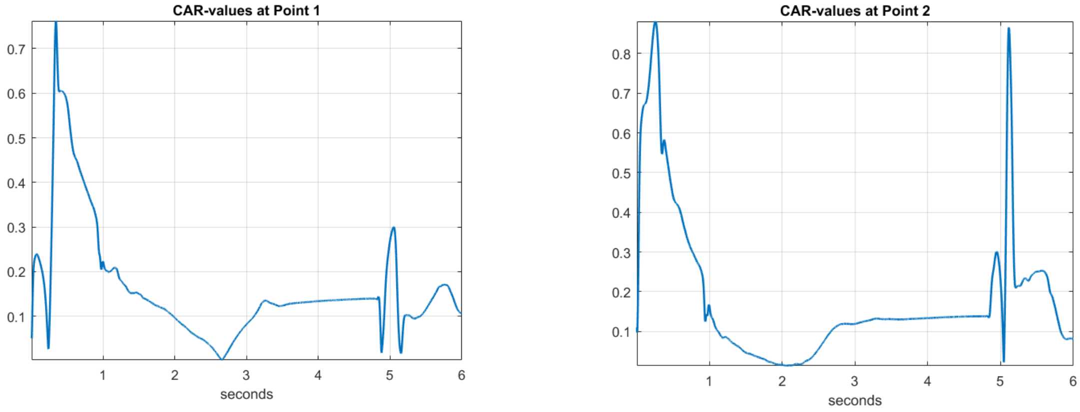

Figure 8.36: Computed time-histories for CAR- values, case 7

Case 8

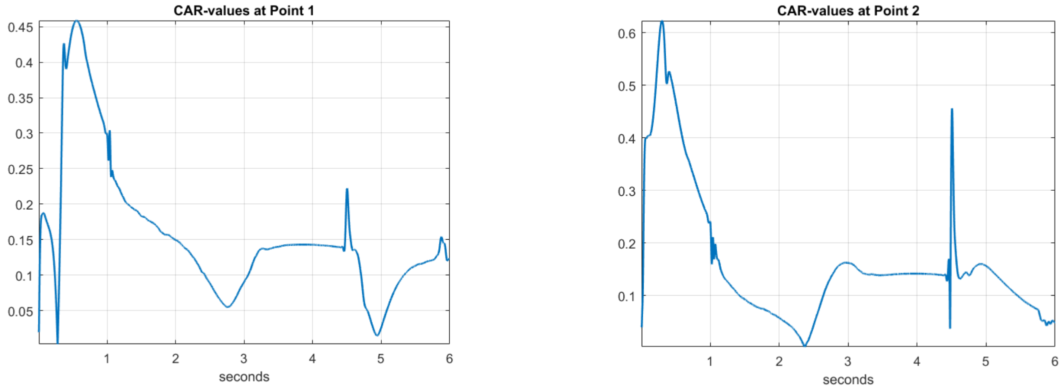

Figure 8.37: Computed time-histories for CAR- values, case 8

Case 9

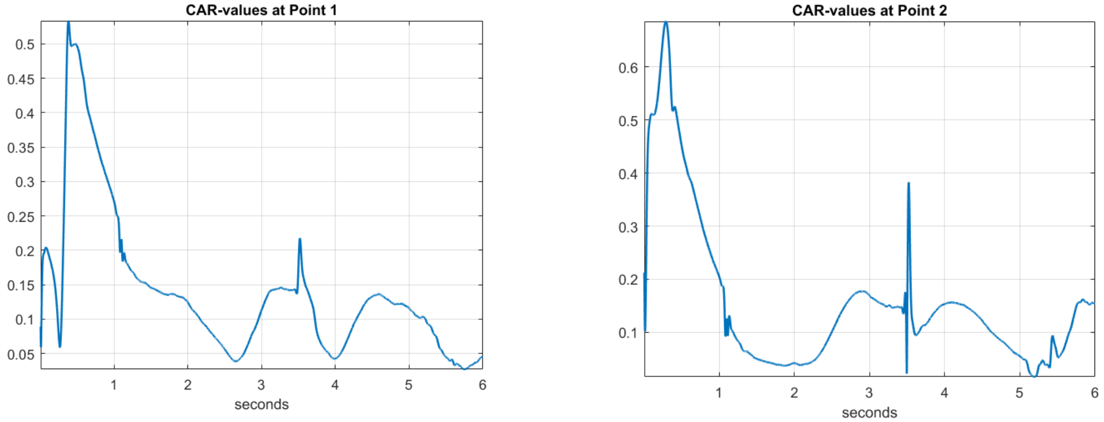

Figure 8.38: Computed time-histories for CAR- values, case 9

Case 10

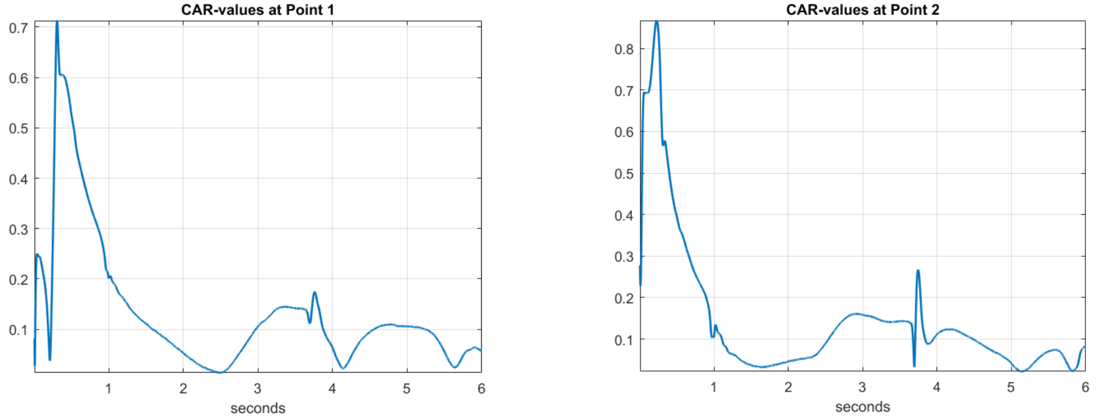

Figure 8.39: Computed time-histories for CAR- values, case 10

Case 11

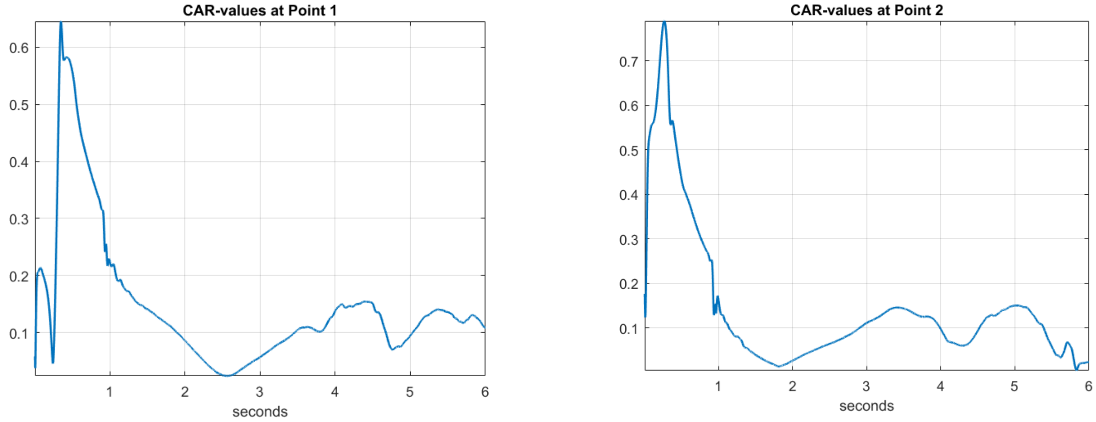

Figure 8.40: Computed time-histories for CAR- values, case 11

Case 12

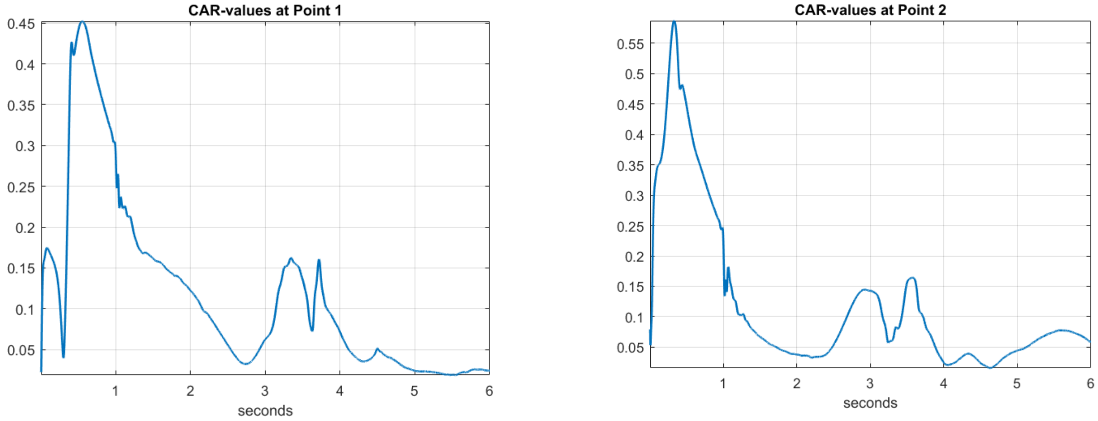

Figure 8.41: Computed time-histories for CAR- values, case 12

Case 13

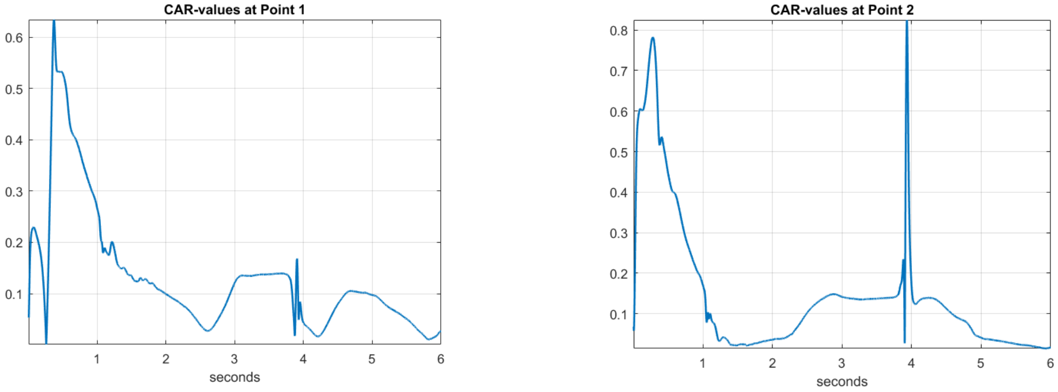

Figure 8.42: Computed time-histories for CAR- values, case 13

Case 14

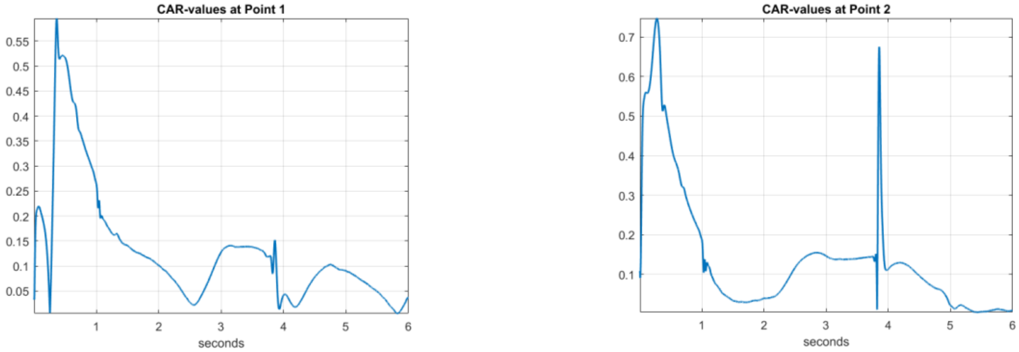

Figure 8.43: Computed time-histories for CAR- values, case 14

Case 15

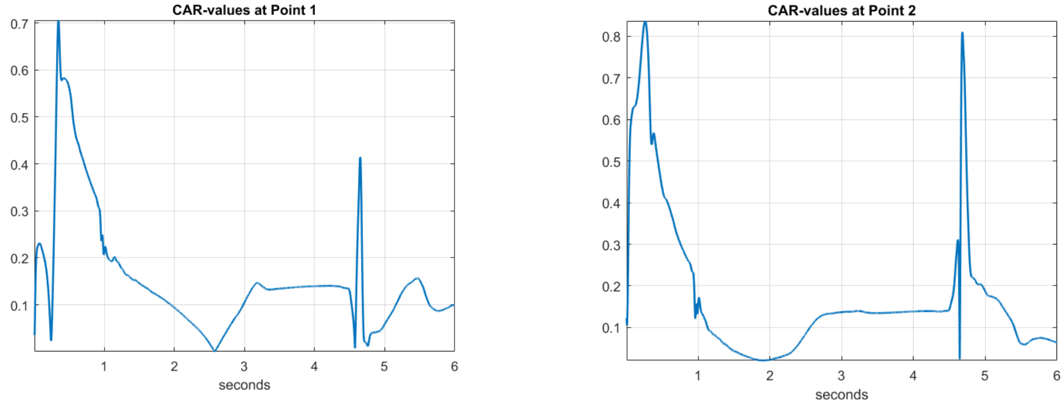

Figure 8.44: Computed time-histories for CAR- values, case 15

Case 16

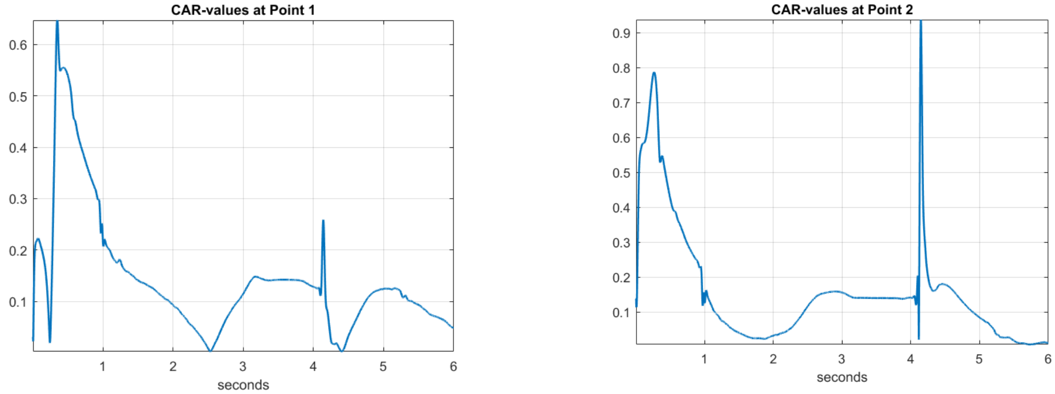

Figure 8.45: Computed time-histories for CAR- values, case 16

Case 17

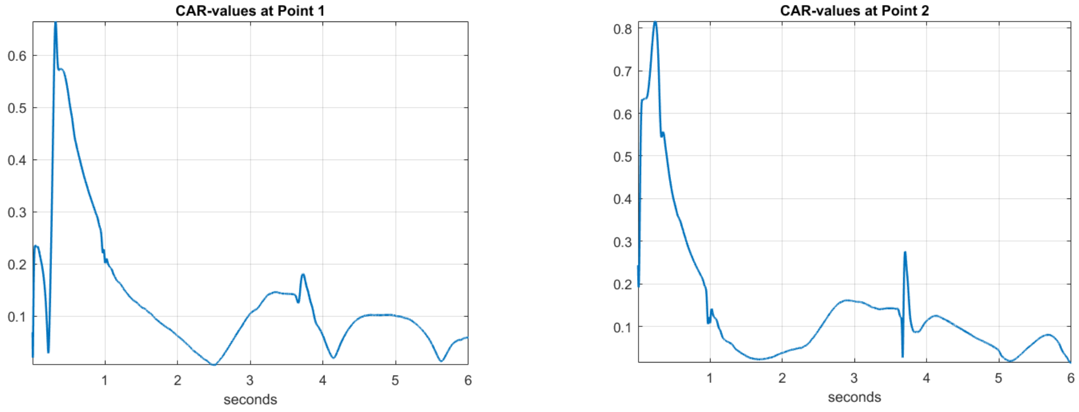
CAR-values at Point 1

CAR-values at Point 2

Figure 8.46: Computed time-histories for CAR- values, case 17

Case 18

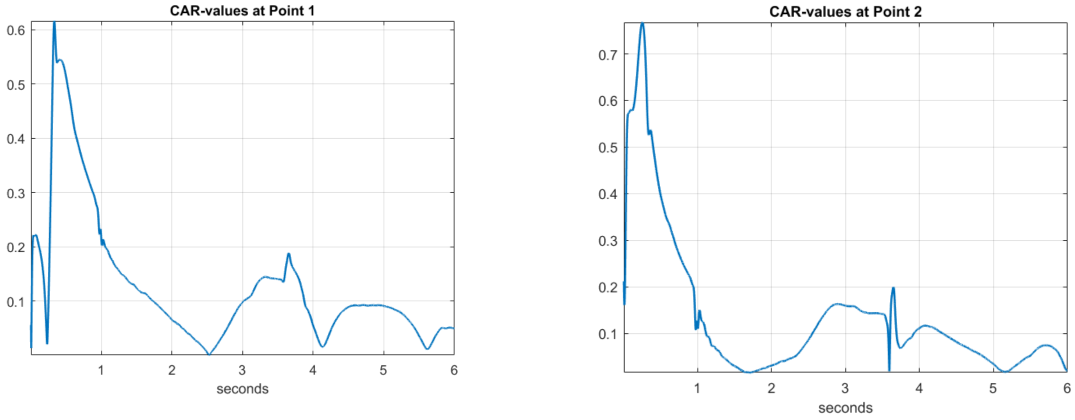
CAR-values at Point 1

CAR-values at Point 2

Figure 8.47: Computed time-histories for CAR- values, case 18

None of the cases experience CAR-values above 0.92. All values less than one are defined as safe according to DNV GL (2016). At these initial conditions, that is the impact velocity, water entry angle, initial rotation, wave phases and headings, the passengers at the specified positions should be able to escape the evacuation scene, without getting harmed. It is important to specify that this is for the origin of the chosen seat positions. When the position is moved out of the x_{body} axis, such that an y- and z-arm is formed, there will be extra contributions from roll and yaw accelerations as well, which can create additional stresses on the passengers.

The time histories of the CAR- values reveals that for most of the cases, the highest values are found in the water entry phase, where the magnitude of the z_{body} acceleration is dominating. The computed time-histories for the angular pitch velocities shows that all the cases have an increasing counter clockwise velocity shortly after impact, hence a counter clockwise pitch acceleration. This rotation creates a contribution in the same direction as the z_{body} acceleration for the fore part, and opposite for the aft part. This is the reason for the largest CAR-values is in fore part in the water entry phase. In Case 5, the rotation is relatively small, and the difference in CAR-value for the two passenger positions are small.

The highest CAR- value is found for Case 2 at 4.0 s. This is when the body re-enters the surface. The stern enters first, creating a large clockwise angular acceleration. This creates an increased acceleration in the fore part that acts in the same direction as the z_{body} acceleration, this creates large second slamming forces on the fore part as it re-enters the surface. The acceleration is in the positive heave direction, the same direction as the counter clockwise pitch acceleration.

When the body dives in the $\frac{3\pi}{2}$ phase, regardless of heading, low CAR-values are observed in the water entry phase. This is due to direction of the fluid velocity, which acts downward, and the relative fluid-body velocity gets smaller. Hence this will be a favourable phase to enter in.

9 Conclusions and discussion

For the convergence check, the order of accuracy showed low values. This implies that the solution is not fully converged, at least not locally. However, the global behaviour of the body is approximately the same for the three different tested mesh discretisation's. This is apparent from the position plot, where for instance the difference in maximum submergence is four centimetres between the coarsest and the finest mesh, and only one centimetre between the finest and the second finest. The second finest mesh is assumed to give satisfactory result, with an acceptable computational time.

The simulations show low average CFL numbers, which is required for maintaining accurate solutions. Some Y^+ values in the $Y^+ < 30$ region has been detected, Star CCM+ then recommends an all Y^+ treatment, which has been chosen. However, how Star CCM+ solves for the values where $1 < Y^+ < 30$ is unknown, and this brings up some uncertainties as it has not been possible to obtain the method from Steve adapco.

The simulations of the simplified lifeboat geometry in calm water conditions, shows an expected behaviour according to theory. There are large accelerations inflicted on the body in the water entry phase. The air cavity formation and collapse are visual in the VOF scenes and as a large acceleration peak in x_{body} at approximately one second. For this case, with the chosen initial conditions, the body gets a small pop- height. This leads to a small second slamming when the body re-enters the water surface. The attempt of compare existing theory for air cavity closure parameters for water entering projectiles showed small order of compliance. The reason for this is due to the many severe differences, like oblique impact, body density and size, between the compared cases. The simplified pop-up height predictions showed better resemblance with theory, and seem to be able to give a coarse indication for this value.

The parameter investigation shows that changing the impact velocity with $\pm 5\ m/s$ gives the largest affect on the behaviour. The water entry angle changing of $\pm 5°$ shows some effect, but in much lesser extent than for the velocity. The behaviour of the body is little effected by changing the COG_z with $\pm 5\ m$, the most pronounced changes for this case are in the pop-up height.

When waves with wave length 85 m and wave height of 7 m are included in the simulations, it shows a great effect on the behaviour of the body. The particle velocity acting in different directions dependent on which wave phase it is located in. For cases where the impact point are located in phases with upward-directed fluid velocity, the body experiences large deaccelerations, this is apparent in the z_{body} acceleration plots and in the CAR- value plots. The opposite is the case for the cases where the impact points are located where the fluid velocity is acting downwards, the relative fluid-body velocity becomes low which leads to smaller accelerations on the body. For cases where the fluid velocities are acting in the same x_{global} direction as the body, that is for impact points in wave crest and wave trough in following and head sea, respectively, large counter clockwise pitch velocities occur before the slamming of the aft part. This causes large z_{body} accelerations in the water entry phase. The CAR-values in the fore part gets large in the water entry phase as the rotation contributes in the same direction as the z_{body} accelerations.

For beam sea, there will be relatively large acceleration in sway, and there will also be roll and yaw motions, they are most pronounced for diving in wave crests and wave troughs, as the particle velocities are lateral to the body motion. This can cause large translation in the y_{global} direction, and the lifeboat will then be dependent on a large area free for obstructions. Hence, multiple lifeboat diving can be problematic as they can crash into each other

By decreasing the wave height, most of the accelerations in the water entry phase is decreased. The particle velocity gets reduced as it is proportional to the wave amplitude. The magnitude of the second slamming on the fore part can however be larger for a wave with lower steepness, as it is highly dependent on pitch acceleration given in and after the water exit.

The air is modelled as incompressible in his thesis. In reality, this is not the case. This is specially of interest for the entrapped air bubble on the stern, which is expected to oscillate due to the compressible air. The behaviour of the body is expected to be affected when the air is modelled as compressible.

An actual lifeboat geometry will have appendages. They will create their own air cavities, and this will influence the behaviour of the body, and the trajectory. The simplified geometry in this thesis will however show many similar features, and what to expect of a typical lifeboat geometry.

There are some uncertainties connected to the simulations and its outcome. The segregated flow solver is not optimal for presenting the slamming. There has also been detected some unrealistic high velocities on the corners on the aft part, after the air cavity has started to form. How these uncertainties will manifest further out in the solution is uncertain. Interpolations errors are introduced for the overset mesh as the cell size is varying. The field values are expressed at the acceptor cells in one mesh using the field values at the donor cells in the other mesh. If the cell size had been held constant in the overset, the interpolation errors would have been in the same order as the discretisation error magnitude. (Steve CD adapco, 2016)

10 Recommendations for further work

- A real lifeboat geometry is optimized for the passengers safety. The aft part is designed to reduce the air cavity and its retardation forces. A real lifeboat will have appendages, these will create air cavities of their own. For further work a real lifeboat geometry could be interpreted in Star CCM+ and analysed.

- Further investigation of diving in wave conditions with different wave parameters, by
  - Investigate the effect of changing the wave length
  - Test different heading angles
  - The waves could be modelled with fifth order VOF waves settings in Star CCM+, these are more realistic waves.
  - Increase and decrease the impact velocity and water entry angle for impact in wave crest and wave trough, respectively. As these impact parameters will be dependent on the wave elevation.

- The air is modelled as incompressible in this thesis. This is a simplification, as it in reality is compressible. Modelling the air as compressible could be combined with diving in wave condition.

- Preformed a structural analysis, and test the structural integrity for the worst wave conditions and with air modelled as compressible, to see how well a structure will hold for these cases.

- Preform model testing and compare the result with CFD analysis, this could be done in both calm water condition and in wave conditions.

References

Berchiche, N., Östman, A., Hermundstad, O. A. & Reinholdtsen, S.-A., 2015. *Experimental validation of CFD simulations of Free-Fall Lifeboats launches in Regular Waves,* s.l.: s.n.

Califano, A. & Brinchmann, K., 2013. *Evaluation of Loads During a Free-Fall Lifeboat Drop,* s.l.: ASME.

Colicchio, G., Greco, M. & Faltinsen, O. M., 2006. *A BEM-level set domain-decomposition strategy for non-linear and fragmented interfacial flows,* s.l.: INTERNATIONAL JOURNAL FOR NUMERICAL METHODS IN ENGINEERING.

Consultance, M., 2017. *Marin Consultance.* [Internett]
Available at: http://www.mcl.co.tt/product/norsafe-free-fall-lifeboat/

DNV-GL, 2010. *Environmental Conditions and Environmental Loads,* s.l.: s.n.

DNV-GL, 2016. *Design of free-fall lifeboats,* s.l.: DNV-GL.

Engineering ToolBox, u.d. *Engineeringtoolbox.* [Internett]
Available at: http://www.engineeringtoolbox.com/fluid-density-temperature-pressure-d_309.html
[Funnet 01. May 2017].

Faltinsen, O. M., 1990. *SEA LOADS ON SHIPS AND OFFSHORE STRUCTURES.* s.l.:Cambridge university press.

Faltinsen, O. M. & Greco, M., 2013. *CFD and Wave and Current Induced Loads on Offshore.* s.l.: NTNU.

Faltinsen, O. M. & Timokha, A. N., 2009. *Sloshing.* s.l.:Cambridge university press.

Fouques, S. & Hermundstad, O. A., 2016. *Structural Integrity Assessment of Free-Fall Lifeboats by combining fast Monte-Carlo simulations with CFD by means of Proxy Load variables,* s.l.: ASME.

Gekle, S. et al., 2008. *Noncontinous Froude Number Scaling for the Closure Depth of a Cylindrical Cavity ,* s.l.: The American Physical Society.

Greco, M., 2012. *TMR4215 - Sea Loads - Lecture Notes,* s.l.: s.n.

Hirt, C. W. & Nichols, B., 1979. *Volume of fluid (VOF) Method for the dynamics for free boandaries ,* Los Alamos: Los Alamos Scientific Laboratory .

J. Andreson, G. D. J. D. E. D. R. G. J. V., 2009. *Computional Fluid Dynamics.* Berlin: Springer.

Jin, J., Ringen, E. & Reinholdtsen, S.-A., 2014. *Forward Distance Performance of a Free Fall Lifeboat in a Seaway,* s.l.: ISOPE.

Kim, G.-H. & Park, S., 2016. *Development of numerical simulation tool for efficient and robust prediction of ship resistance,* s.l.: International Journal of Naval Architecture and Ocean Engineering.

NTNU HPC Group, 2016. [Internett]
Available at: https://www.hpc.ntnu.no/display/hpc/About+Vilje

Sauder, T. & Fouques, S., 2009. *Theoretical Study of the Water Entry of a Body in Waves. Application to Safety of Occupants in Free-Fall Lifeboats,* s.l.: s.n.

Steve CD adapco, 2016. *User guide Star-CCM+ version 11.06,* s.l.: https://stevedocs.cd-adapco.com/starccmplus_latest_en/index.html?param=gYuRe#page/STARCCMP%2FGUID-899D7E79-198D-4E90-B064-F085542B954F%3Den%3D.html%23.

Tregde, V., 2015. *Compressible Air Effects in CFD Simulations of Free Fall Lifeboat Drop,* s.l.: s.n.

Truscott, T. T., Epps, B. P. & Belden, J., 2013. *Water Entry of Projectiles,* s.l.: s.n.

Truscott, T. T., Epps, B. P. & Munns, R. H., 2016. *Water exit of buoyant spheres,* s.l.: American Physical Society .

White, F. M., 2006. *Viscous fluid flow.* Singapore: McGraw-hill companies .

Yan, H., Liu, Y., Kominiarczuk, J. & Yue, D. K. P., 2009. *Cavity dynamics in water entry at low Froude numbers,* s.l.: Cambridge university.

Ytrehus, T., u.d. *The gouverning conservation equations in fluid mechanics,* Trondheim: NTNU.